ABSTRACT

Title of dissertation: AN EXPERIMENTAL AND GRAPH THEORETIC STUDY OF ATOMIC LAYER DEPOSITION PROCESSES FOR SPACE APPLICATIONS

Hossein Salami, Doctor of Philosophy 2019

Dissertation directed by: Professor Raymond A. Adomaitis
Department of Chemical and Biomolecular Engineering

Accurate understanding of the atomic layer deposition (ALD) process kinetics is necessary for developing new ALD chemistries to produce novel nanomaterials, and also optimization of typical ALD processes used in industrial applications. Proposing a potential reaction sequence alongside with accurate kinetic data is among the very first steps in studying the ALD process kinetics and forms the backbone of further engineering analysis. A valid and proper ALD reaction network (RN) must be able to reflect the self-limiting and cycle to cycle reproducibility behavior experimentally observed for practical ALD processes. Otherwise, the mathematical model built based on it fails to precisely capture and reproduce ALD behavior no matter how accurate the available kinetic data are. In this work, a RN analysis method based on species-reaction graphs and the principles of convex analysis is developed to study the mathematical structure and dynamical behavior of thin-film deposition RN models. The key factor in ALD RN analysis is the

presence of consistent surface-originated invariant states for each ALD half-cycle. Therefore, the primary focus of the proposed approach is on identifying and formulating physically-relevant RN invariant states, and to study the chemical significance of these conserved modes for ALD reaction mechanisms. The proposed method provides a well-defined framework, applicable to all ALD systems, to examine the above criteria of a proper ALD RN without requiring any information on the reaction rates. This method fills a gap in the procedure of ALD process modeling before the time-consuming step of calculating individual reaction rates which is usually done through ALD experiments in reactors equipped with in-situ measurement instruments or computationally expensive computational chemistry-based calculations such as density functional theory. The presented approach is also extended to study the variant states of a RN. The generalized method provides information on different variant states dynamically depending on each individual reaction in the network which facilitates the study and ultimately the formulation of different reaction rates in the system.

In the second part of this dissertation, an experimental study of ALD of indium oxide and indium tin oxide films using the trimethylindium, tetrakis (dimethylamino) tin(IV), and ozone precursor system is conducted to first, investigate the potential application of this ALD process for producing high-quality transparent conducting layers; and second, to understand the relationship between the thickness of the deposited films and their electrical and optical properties. The optimized recipe was then used to process commercial Z93 heat radiator pigments used in manufacturing spacecraft thermal radiator panels to enhance their electrical con-

ductivity to avoid the differential charging that may occur due to the interaction with charged particles in Van Allen radiation belts. To this aim a specialized ALD reactor was designed and constructed capable of processing standard flat substrates as well as coating micron-sized particles. The results confirm that the proposed process can be used to coat the heat radiator pigment particles and that the indium oxide film can nucleate and grow on their surface. This provides an example from a variety of potential space-related applications that can benefit from the ALD process.

AN EXPERIMENTAL AND GRAPH THEORETIC STUDY OF ATOMIC LAYER DEPOSITION PROCESSES FOR SPACE APPLICATIONS

by

Hossein Salami

Dissertation submitted to the Faculty of the Graduate School of the
University of Maryland, College Park in partial fulfillment
of the requirements for the degree of
Doctor of Philosophy
2019

Advisory Committee:

Professor Raymond A. Adomaitis, Chair
Professor Garry Rubloff
Professor Kyu Yong Choi
Professor Dongxia Liu
Professor Ganesh Sriram

Dedication

Dedicated to my parents Shahla and Naser. I will never be able to thank you enough for all the sacrifices you have made.

Acknowledgments

On writing a dissertation, a semi-wise man once said the most fun part is writing the acknowledgment because in the middle of writing two hundreds or so pages that is the only place that you get to be a poet instead of a semi-scientist... Where should I begin, not that I cannot think of anyone who I need to thank, but because names and memories flood my brain whenever I start to do so. So let me play a romantic song and begin.

I would not have been able to be where I am today without the help of many dear friends and companions and I must thank all of them. I must thank my adviser Ray, Adomaitis. Ray I learned so much from you. You are always so positive in your feedback on my work and always very patient with my mistakes. I must thank my unofficial co-adviser Vivek Dwivedi. Vivek, I can only hope to become an engineer like you one day. I was really lucky to get the chance to work on these amazing projects and I really appreciate your trust in our work. I must thank Maryland nanocenter staff John, Thomas, Jonathan and Mark. You guys are amazing, your answer to our numerous questions and requests is always a friendly face and lots of help. I mus thank my group-mates old and new ones. I want to thank David, Krishna, Harika, Corinne, Andrew, and specially Aisha, Alan and Aarathi . You guys are great, you were a big help and you always make the lab work more fun. My best wishes for you. I must thank my classmates, friends and colleagues in the Chemical and Biomolecular Engineering Department. Svet, Viviana, Derrick, Dylan, Kevin, Emily, Dennis, Kyle, Nico and Wei. Some of my best memories in the

past five years was with you. It was not possible to handle all this without friends. I must specifically thank my friends Nick and Sean. Maybe you are not aware of it yourself, but you guys helped me so much to adjust to the life here. You are bright, open-minded and fun and I just do not want to stop hanging out with you guys. I must thank our department staff specially Patricia, Kathy, Kay, Jenna and Karin. I am grateful for all your help and just hope that I have not made your life too difficult with all my questions, paperwork and wrong forms.

I must thank my parents but is there anyway to thank your parents with words...? I just want to say that I know there was no way to do all this without you. I still have so much to learn from you. I must thank my lovely wife Mahsa, you always have been supportive and super patient with me freaking out, coming home tired and being all graduate schooly. I must thank my sister and my brother, Hadis and Abbas. Being with you guys even through Skype is so much fun, let us stay kids forever. I also must thank my brother in law Siavash, you know that word in law does not mean much at this point. I am coming from a relatively large and very close family, and I want to thank my grandparents who are not here anymore... my aunts, uncles and my cousins. Specifically, I want to thank my uncle Daeijun who was one of my biggest supporters for doing this. Daeijun, you know my only regret for this is that I could have spent this time hanging out with you. I also must thank U.S tax payers. This project was partially supported by National Science Foundation, and I am thankful for their support. I am also thankful to Dr. Jan Sengers for the Sengers Ph.D. candidacy graduate scholarship; and to the Future Faculty program of the Clark School of Engineering.

Table of Contents

List of Tables

List of Figures

List of Abbreviations

Acet	Acetaldehyde
ALD	Atomic Layer Deposition
ALE	Atomic Layer Epitaxy
CVD	Chemical Vapor Deposition
DFT	Density Functional Theory
EDS	Energy Dispersive X-ray Spectroscopy
FB	Fluidized Bed
FTIR	Fourier-transform Infrared Spectroscopy
GJ	Gauss-Jordan
gpc	Growth Per Cycle
InCp	Cyclopentadienylindium
IO	Indium Oxide
iPrOH	Isopropanol
ITO	Indium Tin Oxide
ML	Molecular Layering
MOT	Molecular Orbital Theory
$Ni(Cp)_2$	bis(cyclopentadienyl)nickel
$Ni(acac)_2$	nickelacetylacetonate
ODE	Ordinary Differential Equation
PEC	Photoelectrochemical Cell
Prop	Propane
QMS	Quadrupole Mass Spectroscopy
QCM	Quartz Crystal Microbalance
RN	Reaction Network
SEM	Scanning Electron Microscopy
SR	Species-Reaction
TEM	Transmission Electron Microscopy
TDMASn	Tetrakis(dimethylamino)tin
TMA	Trimethylaluminum
TMI	Trimethylindium
XPS	X-ray Photoelectron Spectroscopy
XRR	X-ray Reflectivity

Chapter 1: Introduction

Atomic layer deposition (ALD) is a nanomanufacturing method for depositing thin solid films in which through separated introduction of a pair or a group of gaseous precursors to a reactor, high-quality and conformal thin-films can be deposited with nanoscale control of the film thickness on a variety of substrates ranging from standard flat surfaces to those with significant topography. Because of this ability ALD is emerging as a critical manufacturing technology in areas such as optics, energy storage and conversion, nanoelectronics and biomedical engineering [7, 48, 54, 94, 95, 131, 144]. In an ideal thermal ALD process chemical reactions are limited to surface reactions which are terminated upon complete consumption of accessible reaction sites on the growth surface during each precursor exposure. Each precursor exposure step is usually referred to as a half-reaction in a binary ALD process. This makes ALD a self-limiting process and results in a constant amount of material deposition during each ALD cycle [171]. Another advantage of thermal ALD is that it is not a line-of-sight process, so any surface exposed to the gas-phase with active surface sites will be coated [107]. It is because of these characteristics that ALD can be used to coat different substrates whether flat, porous

or even particles with theoretically the same quality and high accuracy; and one can achieve the desired coating or film thickness simply by adjusting the number of ALD cycles [131, 181].

1.1. History of ALD

ALD process was developed independently by two researchers, in 1960 by S. Koltsov in Soviet Union under the name Molecular Layering (ML), and in 1974 by T. Suntola in Finland under the name Atomic Layer Epitaxi (ALE) [131]. Nevertheless, this method did not get widespread attention at the time. One reason for this was that the film growth process was relatively slow compared to other available methods and there were not many applications where the precise control over the film thickness offered by ALD was particularly interesting and required [7, 139]. This situation started to change close to the beginning of the new millennium. One of the main motivations for the increasing interest in ALD by both industry and academia was the race for satisfying the well-known Moore's law [23, 73] in electronics. Continuing down-scaling of dielectrics and metallic electrodes used in electronics in addition to structures with high aspect ratios and complicated geometries require a thin-film manufacturing method which offers high-quality films with excellent control of the thickness and ALD is one of the few methods capable of doing so in a relatively simple process.

While the main application of ALD is in electronics and semiconductor industry, there are other areas that can benefit from this process. Recently, ALD-optimized catalysts have gained much research interest. ALD can be used to make

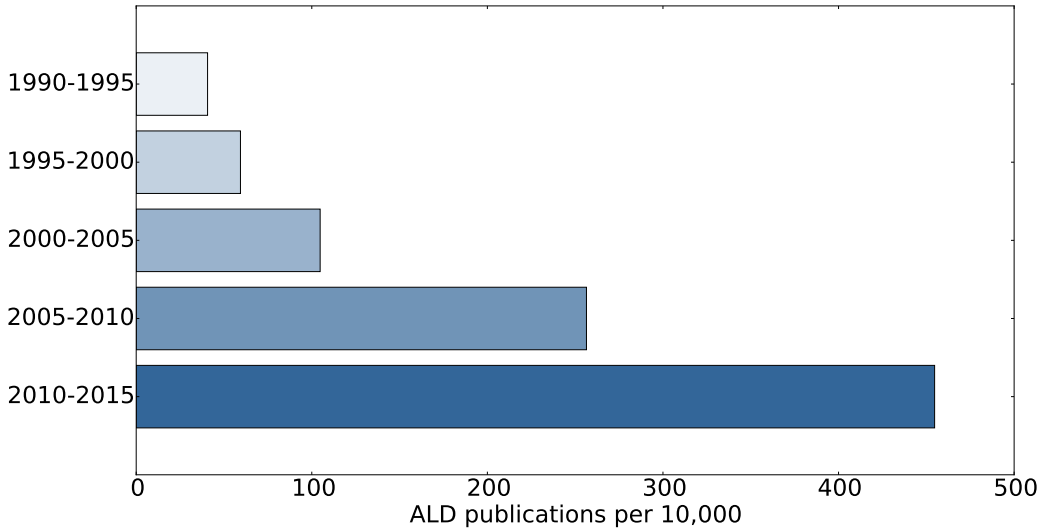

Figure 1.1: Number of *"atomic layer deposition"*-related publications in publications in *"thin film"* area from 1990 to 2015. The data are extracted from GoogleScholar database by searching the related terms [60].

well-dispersed catalysts where the catalytic activity can be enhanced as a result of higher dispersion and also potentially inherent features of the grown nanostructures which might differ from those of bulk. Furthermore, since thermal ALD is not a line-of-sight process it is suitable to deposit catalyst active sites on porous supports [61, 133] . Other example applications for ALD are manufacturing photocatalytic material for Photoelectrochemical (PEC) cells, and depositing active or protective layers for enhanced performance of batteries and supercapacitors [165].

A new potential field of application for ALD is in space. ALD is a natural technological fit for manufacturing spacecraft components where weight, conformality, processing temperature, and material selection are all at a premium. Applications may include optical, thermal control, electric charge dissipation, and protective coatings for the surprisingly reactive environment of low Earth orbit [74, 145].

1.2. Principles of ALD

ALD is a specific form of the more general thin-film deposition method Chemical Vapor Deposition (CVD). The word chemical in the name refers to deposition of the film by a chemical reaction between a vapor-phase molecule and a surface. The main difference between ALD and CVD is that during the thermal CVD process the gaseous precursors are continuously fed to a heated reactor in which after a series of gas-phase and surface reactions, the thin-film material is deposited on a solid substrate. On the other hand, in an ALD process, the precursors enter the reactor sequentially and react with the growth surface during two or more ALD cycle-fraction reactions (together forming one complete ALD cycle). Separating the precursor exposures prevents uncontrolled gas-phase reactions and can be achieved by either temporally or in some cases spatially separated half-cycles [23]. Using an appropriate precursor system, each precursor pulse provides an activated surface for adsorption and reaction of the next precursor and continuing the same procedure for hundreds of times results in film deposition with desired thickness. For a comprehensive introduction to the ALD process the reader is encouraged to look at [139].

1.2.1. ALD process steps

As it is shown in figure 1.2, a typical binary ALD process consists of four main steps.

1. The first step begins with pulsing the first precursor molecules into the reactor chamber. For this step one can use the precursor's own vapor pressure as the

driving force for the transport (direct draw). Alternatively, a noble carrier gas such as argon or nitrogen can be used to facilitate the transport of the precursor molecules to the deposition chamber. Upon contact with the deposition surface covered with active surface sites these molecules will initially adsorb either physically or chemically onto the surface to later participate in subsequent surface reactions provided sufficient thermal energy. This thermal energy is needed for overcoming the energy barrier of the surface reactions and is supplied by an external heating source in thermal ALD processes. Plasma-enhanced ALD and electron-enhanced ALD are examples of ALD processes where a different type of energy source is used to provide the driving force for the surface reactions [54, 163]. While these can be more efficient compared to thermal ALD in terms of proceeding surface reactions, they require more sophisticated reactor designs. They are also line-of-sight processes and therefore, may lack one of the main advantages of ALD. This step ends with the first precursor molecules being chemically bonded to the surface. As mentioned, in an ideal process sufficient precursor and thermal energy is provided inside the chamber to saturate the deposition surface.

2. After the first precursor pulse the gas phase inside the reactor chamber is contaminated with excess precursor molecules and also the byproducts of the reactions between the precursor and the deposition surface. During the first purge period sufficient time is given to the purge gas to carry these to the pump and flush the reactor. This ensures that reactions between the two

precursors are limited to surface reactions.

3. This step mimics the first step only for pulsing the second precursor. Note that in a successful ALD the combination of precursors is chosen so that each precursor reaction with the deposition surface provides an activated surface for the next precursor.

4. Again, purge of a noble gas cleans the chamber from excess precursors and byproducts.

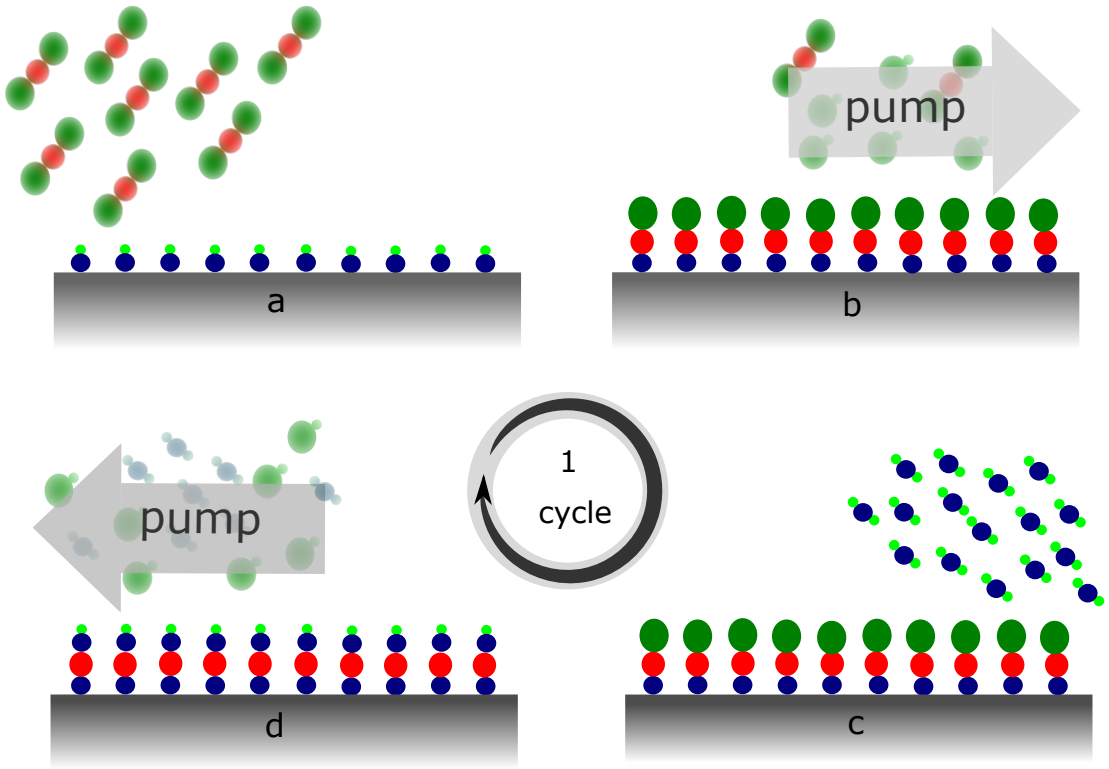

Figure 1.2: Schematic demonstration of the four main steps of a typical thermal ALD process with two precursors, consisting of two precursor pulses (a,c) and two purge periods (b,d). Repeating this sequence for sufficient number of cycles results in deposition of a thin-film with film thickness ideally only dependent on the number of cycles.

1.2.2. Self-limiting behavior

Limiting the reactions between the two precursors to surface reactions provides a very fine control on the amount of material deposited during each ALD half-cycle because surface reactions are self-limiting in an ideal thermal ALD process, meaning that these will terminate upon reaching saturation and remain essentially inactive with further uncontrolled exposure of the precursor materials to the system. In general, this self-limiting behavior and saturation of the deposition surface is induced by two factors [132, 143]

1. Complete consumption of active surface sites by precursor molecules.

2. Steric hindrance from large fragments of already adsorbed precursor molecules, preventing adsorption of additional molecules from vapor phase.

The self-limiting characteristic of the ALD process and its cyclic nature have another important consequence. Unlike CVD, ALD is an inherently dynamic process. The system behaves as a dynamic system during each cycle, reaching the saturation and starting the same trajectory (except the initial nucleation period [129]) over in the next cycle and so no steady-state condition can be defined for an ALD process. For this reason the film growth in ALD is reported as growth-per-cycle (gpc), different than CVD which can operate as a continues process and the film growth is reported as growth per unit of time [139, 143].

1.2.3. Nonideal ALD

There are multiple factors that can lead to nonidealities and deviations from self-saturating ALD. Many of the nonidealities observed in ALD experiments belong to one of the following categories [139].

1. Precursor depletion: In a typical ALD process excess amount of gaseous precursor is introduced to the deposition chamber to ensure complete consumption of active sites and surface saturation. Under-exposure of precursor leads to unreacted surface sites and results in deviations from nominal gpc and nonuniformity in the final product. Under-exposing some parts of the substrate can also occur as a result of deficient precursor delivery and transport system or reactor flow dynamics [48, 52].

2. Extreme temperatures: As mentioned, in an ideal ALD reactions are limited to initial precursor adsorption and subsequent surface reactions. In some cases the temperature used in the reactor is so high that leads to decomposition of precursor molecules. The active fragment products of the decomposition reaction may react with surface and add additional pathways to film deposition. While this often leads to higher gpc and faster film deposition rates, it is undesired in ALD since it results in losing the precise control over the final film thickness. Note that this new pathway might not be self-limiting meaning higher precursor injection or higher availability of precursor molecule fragments in some regions in the chamber directly results in more film deposition. On the other hand, if the process temperature is not sufficiently high,

the energy to overcome the barrier of the surface reactions will not be available. The temperature range between these two extremes is usually referred to as ALD window, where, ideally, the gpc becomes relatively insensitive to temperature.

3. Insufficient reactor purge: The purging period between different precursor pulses is utilized to ensure that active precursors do not meet in the gas phase. If for reasons such as short purge periods precursor molecules from a previous pulse or byproducts of the previous pulse are still present in the chamber when the next precursor is being pulsed uncontrolled gas-phase reactions may occur which can lead to additional deposition pathways and again uncontrolled growth. This can be a major concern in systems where byproducts of a precursor reaction with the deposition surface have high desorption energy barriers hence tend to remain in the reactor for longer periods. Other systems where such nonidealities might occur are those where water is used as the oxygen source in the film. Highly polar water molecule tends to stick to reactor walls and remain in the chamber for extended periods of time. Note that the extreme case of this is when no purge period is being used making the process essentially a CVD [134, 135].

1.3. ALD modeling

Same as many other chemical processes, simulation tools and accurate mathematical models that can describe and predict the behavior of ALD process are important for process design, optimization and control. These are also critical for

production of films with desired properties. Development of such models is complicated due to inherent dynamic of the ALD process, complex system of chemical reactions encompassing homogeneous and heterogeneous reactions with widely varying timescales and challenges of obtaining accurate experimental data [3]. A comprehensive model of an ALD process describes both transport of the precursor material and reaction byproducts, in addition to kinetics of surface and potential gas-phase reactions [52, 121]. While the principal mass transport phenomena governing the transport of different species in the system are well-understood, detailed representation of reaction kinetics is much more challenging. One of the main reasons for this is the difficulty to experimentally observe and measure the evolution of different species on the deposition surface [3].

Considering the fact that the material deposition relies on the adsorption of precursor molecules on the deposition surface, the simplest approach, taken by many early modeling efforts, is to use the concept of sticking coefficient [134, 135] to study the precursor-surface chemistry. This parameter essentially represents the probability that a precursor molecule reacts with the deposition surface and remains chemically bonded to the surface upon colliding with the surface. Clearly, such probability is a function of precursor adsorption energy, process temperature, energy barrier of surface reactions, etc. This parameter then can be fitted to experimentally measured growth data to represent the behavior of the process under specific reactor conditions. Similar to all other empirical approaches, the optimized model is only applicable to systems under the same operating conditions and chemistry and shall not be extrapolated. The other common approach to model the chemistry of an

ALD process is to, again, use the sticking coefficient parameter but increase the accuracy by including the surface reactions explicitly in the kinetic model [134,135]. Rate of different surface reactions can be represented by Arrhenius rate functions and corresponding energy barriers can be approximated by fitting the gpc to experimental data. Obviously, development of such empirical models depends on the availability of accurate and representative data.

An alternative approach to the problem of studying of the precursor-surface chemistry is to use available tools based on computational chemistry such as Density Functional Theory (DFT) and Molecular Orbital Theory (MOT) to calculate the thermodynamic and kinetic parameters associated with different reactions in a system under study. Such approaches are usually referred to as *ab initio*, starting from the beginning, modeling since they are, ideally, only based on physical constants. These can range from quantum-level computations to lower level calculations [96]. Recently, application of such models has significantly increased to study gas-phase and surface reactions during both ALD and CVD processes [5, 42, 182, 183]. The outcome of *ab initio* simulations is usually in the form of thermodynamic information describing reaction Gibbs energy, i.e., the tendency of a reaction to proceed, and kinetic information describing the energy barrier associated with a reaction and essentially its rate. This information can be used to identify feasible reaction mechanisms and formulate rate expressions in an ALD process. Upon availability of rate equations describing the rate of different reactions in the system, one can use species mass balance equations to develop a system of Ordinary Differential Equations (ODEs), (or Partial Differential Equations if combined with transport

phenomena) that describe the evolution of different species in the gas phase and on the deposition surface [3, 136, 170, 171].

1.4. Motivation

Clearly, *ab initio* approaches are more sophisticated than empirical ones, and using the obtained reaction rate data and model predictions is not limited to a specific set of reactor conditions. This is specially beneficial in kinetic modeling of ALD processes were obtaining experimental data for fitting the parameters of empirical models is challenging. However, there still remains another challenge.

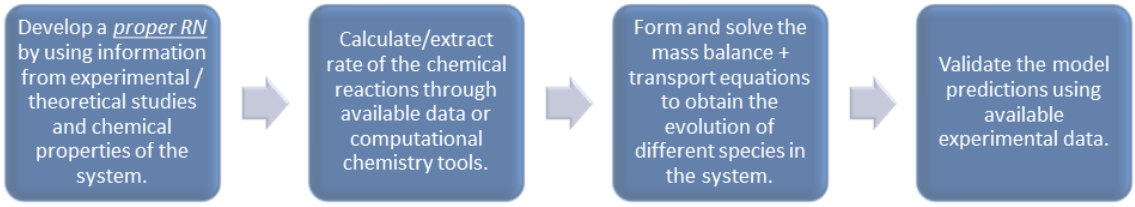

Figure 1.3: Main steps in development of representative surface kinetic models for ALD processes.

At the core of the modeling approach described above and shown in Figure 1.3 lies a set of postulated elementary reactions. One can develop a reaction network (RN) describing different reactions associated with different steps of an ALD process based on the available knowledge on the species in the system and their physical and chemical properties, and then use computational chemistry tools to first, investigate whether each reaction is thermodynamically favored, and second, calculate the energy barrier and subsequently the rate associated with that reaction. However, there are still key questions that the answer to is critical for developing a representative and accurate kinetic model for an ALD process.

1. Is the overall RN balanced, i.e., are all elemental balances satisfied for all time including the system's original state?

2. Can we decouple sets of reactions with different time scales to model the dynamics of the surface species concentrations?

3. Are there combinations of species that define constant molar quantities and, if so, what is the physical significance of these invariants?

4. Will the modes identified as being dynamically redundant have a physical meaning in the context of ALD, and can this meaning be identified as part of the model reduction process?

5. Does the RN's structure guarantee the existence of a self-limiting mechanism in ALD and a consistent growth (surface stability) mode for both ALD and CVD?

6. Is the deposition surface stable, e.g., will the reaction surface area and reactive sites have a positive and bounded value for any number of ALD deposition cycles upon running the model and simulating the system?

7. Is the proposed RN capable of producing a film with correct stoichiometry?

The first four questions are relevant to any RN and any process. Specifically, the answer to the first question seems trivial, indeed for a set of chemical reactions one can validate if the overall RN has the right stoichiometry by balancing every individual reaction. However, doing so is not straight forward in case of atom-free stoichiometries. As will be discussed later, such RN can show up in systems where exact

chemical composition of some species in the system is not well-understood. In those cases the concept of stoichiometrically balanced becomes loose in some sense since there are no specific atoms to be counted on each side of each reaction, however, the consistency of the fragments that are transferred between different molecules still needs to be checked. The second question is concerned with the kinetics of the RN. Different chemical processes give rise to reactions with different time scales. For example, some fast and reversible reactions can be approximated to be in instantaneous equilibrium. These can potentially cause stiffness or singularities when studying the systems dynamics [3, 35, 45]. A systematic model reduction scheme is necessary for studying such RNs. Regarding the third and fourth question, physics dictates that in a closed system, the number of independent reactions is smaller than the number of species present in the system. This results in time-independent modes in an overall dynamic system. These modes may contain potential information about the RN behavior. The last three questions specifically are concerned with the properties of ALD systems. A positive answer to the fifth and sixth questions is crucial for an RN to be able to capture the behavior of true ALD: the ability to operate in a cyclic and self-saturating manner.

The objective of this work is to develop a systematic method to provide answers to above questions for any RN. Specifically for ALD, such method fills a gap in the procedure of ALD process kinetic modeling and optimization before the often time and resource consuming step of calculating individual reaction rates. A validated model describing a consistent set of governing reactions in the growth process can then be coupled with computational chemistry calculations to develop a robust

kinetic model describing the evolution of different gas-phase and surface species in the process. [8, 143, 183].

1.5. Outline of the dissertation

The contents of this dissertation are ordered as follows. Chapter 2 focuses on developing two different but consistent methods based on graphical analysis, and convex analysis to systematically identify and formulate physically-relevant invariants of an RN. It also illustrates how these newly formed states can be used to check whether a proposed RN for an ALD process satisfies the criteria set for a proper ALD RN. Chapter 3 focuses on extending these two methods to study the variant states of an RN, hence enabling one to completely define a mathematical transformation from original species molar amounts to a new state spate where the dynamic dimension of the system is reduced through formulation of physically-relevant RN invariant states, and the effect of each individual reaction rate is decoupled from others by defining new variant states dynamically influenced only by individual reactions. It also illustrates how this information can be used for taking a reaction-based modeling approach in kinetic modeling of different chemical systems such as ALD. Chapter 4 focuses on the experimental study of the specific ALD system of indium oxide for modification of heat radiator coatings used in spacecraft thermal radiators providing an example from a variety of potential space-related applications that can benefit from the ALD process.

Chapter 2: RN Invariants

2.1. Introduction

Reaction invariants are states which remain constant in a dynamic chemical reaction system. These states account for the reduced dimension of the reaction simplex – the subspace in which species participating in chemical reactions evolve – relative to the original chemical species space [141,152]. Invariant states that can be found in different chemical processes include elemental and molecular moiety conservation, reaction site conservation in heterogeneous systems, and charge invariants in electrochemical systems [8].

Representative of early studies of reaction invariants is the series of papers by Asbjørnsen and colleagues in which the potential application of stoichiometric constraints in modeling and control of continuous stirred-tank reactors was demonstrated [10,11]. Reaction invariants can be used together with reaction equilibrium relationships to approximate chemically reacting systems featuring at least one fast timescale [109,152]. Additionally, Gustafsson et al. [66] investigated the use of reaction invariants for pH control in acid-base reaction systems by correlating pH to the reaction invariant states. Most recently, Lu et al. [101] used a combination of reaction invariants and equilibrium relationships to compute the instantaneous buffer

solution composition and pH in an integrated biomanufacturing plant.

Gadewar et al. [50, 51] used reaction invariants for process design rather than process control purposes. They developed a method to systematically determine the invariants of an RN originating from the conservation of elements and showed their method can be used to validate a proposed set of reactions and to formulate molar balances over process units for degree-of-freedom analysis. Reaction invariants in the form of explicitly defined elemental balances also have been used to reduce the dynamic dimension of reaction networks to allow for the graphical analysis of the attainable regions in the synthesis of chemical reactor networks [114, 155].

Invariants also are useful for analyzing biochemical and biological systems [44]. Complexity and nonlinearity present in biochemical RNs coupled with uncertainties in reaction rate parameter values can hinder direct mathematical analysis of these systems. Reaction invariants limit the space where dynamic analysis should be performed to a subspace defined by conservation laws, and can be used in the analysis of experimental data obtained for biochemical systems [46, 77, 150–152]. Reaction invariants also can be used to decrease the number of potential reaction pathways in metabolic networks by excluding those that do not satisfy conservation laws [152].

Another important application of reaction invariants is found in the study and modeling of the ALD processes [8, 170]. As it will be shown, reaction invariants can be used to investigate potential defects in the structure of a proposed RN for ALD kinetic modeling where presence of surface-site related invariants are vital to accurately capturing the behavior of the film growth process [143]. Later in this chapter, application of RN invariants in answering the questions regarding the validity of an

ALD RN posed in the beginning of this dissertation will be demonstrated.

Because of their utility for model reduction and for probing the structural characteristics of RN, there have been many efforts directed to the computation of invariant states. For example, Bonvin and colleagues [9, 141, 164] presented linear and nonlinear transformations to separately identify reaction variants, flow variants, and reaction and flow invariants. Details of their approach and a comprehensive review of studies related to applications of variants/invariants in chemical reaction systems can be found in [141]. More recently, a reaction factorization approach was developed by Remmers et al. [136] to investigate the kinetics of ALD processes in which surface species dynamic balance equations are decoupled by performing a series of Gauss-Jordan (GJ) elimination steps on the stoichiometric matrix using integer arithmetic to identify the conserved (reaction invariants) and the dynamic (reaction variants) quantities. The proposed procedure decouples the reaction time scales and eliminates redundant dynamic modes. Researchers have also reported other model reduction methods such as those in [15, 142, 176] for studying metabolic systems and for process control.

Schuster et al. [152, 154] noted that for a conservation relation, or an invariant state, to represent the conservation of real molecular moieties it must be constructed from non-negative coefficients (making it a semi-positive vector). This is important because if the goal in model reduction procedure is to extract invariant states that are physically-relevant and use those to probe some characteristics of the RN, states which are constructed from all non-negative coefficients are desired. However, in many of the works cited above, more emphasis was placed on using reaction invari-

ants solely for dynamic dimension reduction rather than interpreting their physical significance. This highlights the need for a straightforward approach to identify all reaction invariants and to aid in their physical interpretation.

2.2. Model development

Consider a simplified picture of an one step thin-film deposition process presented by the RN of Table 2.1, in which a gas-phase monomer $M_{(g)}$ participates in a reversible reaction to form dimer $D_{(g)}$ governed by equilibrium relationship defined by the function $e_0(n_{M_{(g)}}, n_{D_{(g)}})$, where n_i corresponds to species molar amount. The monomer $M_{(g)}$ can adsorb with the finite rate f_0 onto a surface to form physisorbed species A, which later can associatively desorb, or react with surface species B to produce a secondary surface species C. Note that while purge period prevents gas-phase reactions between the precursors in an ALD process, such potential dimerization (and trimerization) reactions cannot be avoided. This is for example, the case for widely used aluminum precursor trimethylaluminum (TMA) or nickel precursor nickel(II)acetylacetonate [3, 147]. Furthermore, here it is assumed that the first reaction is a pseudo-equilibrium reaction to emphasize that there is no preset condition on the time scales and rates of the reactions involved in the RN. For an equilibrium process one can use an artificial time constant ϵ to define a reaction rate for the formulation of mass balance equations. Let us, for now, ignore this different rate process and its exact rate representation. This will be discussed in detail in chapter 3 focusing on variant states.

Using the law of molar conservation we write a set of equations in (2.1) for

Table 2.1: The reactions and net-forward rates for the dimer-monomer-adsorbed species reaction network. As it will be shown later, the $(1/\epsilon)$ factor is used to represent a rate for a pseudo-equilibrium process as $\epsilon \to 0$.

Reaction			Net rate	
$D_{(g)}$	$\rightleftharpoons$	$2\ M_{(g)}$	$(1/\epsilon)e_0$	mol s^{-1} m^{-3}
$M_{(g)}$	$\rightleftharpoons$	A	f_0	mol s^{-1} m^{-2}
$2\ A$	$\rightleftharpoons$	$D_{(g)}$	f_1	mol s^{-1} m^{-2}
$A + B$	$\rightleftharpoons$	C	f_2	mol s^{-1} m^{-2}

a closed system with n_s species and n_r reactions using the $n_r \times n_s$ matrix $\mathbf{N}$ (the transpose $\mathbf{N}^T$ is typically referred to as stoichiometric matrix):

$$\frac{d\mathbf{n}}{dt} = \mathbf{N}^T \mathbf{\Phi} \mathbf{r} \quad \mathbf{n}(t=0) = \mathbf{n_0} \tag{2.1}$$

where $\mathbf{n}$ is a $n_s \times 1$ vector containing the number of moles subject to the initial condition $\mathbf{n_0}$. $\mathbf{\Phi}$ is a $n_r \times n_r$ diagonal matrix to adjust the rate units for gas-phase and surface reactions with diagonal elements $[\phi_0, \phi_1, \phi_1, \phi_1]$, where ϕ_0 corresponds to gas phase volume and ϕ_1 to reaction surface area. Finally, $\mathbf{r}$ is a $n_r \times 1$ vector of reaction net-forward rates. Note that at this point the focus is on analyzing the reaction network and extracting the invariants and not accurate representation of reaction rates; therefore, we simply assume that some representation of the reaction rate for both types of reactions (equilibrium or slow kinetic) is available. For RN of

Table 2.1 this gives:

$$\frac{d}{dt}\begin{bmatrix} n_{\mathrm{D}_{(g)}} \\ n_{\mathrm{M}_{(g)}} \\ n_{\mathrm{A}} \\ n_{\mathrm{B}} \\ n_{\mathrm{C}} \end{bmatrix} = \begin{bmatrix} -1 & 0 & 1 & 0 \\ 2 & -1 & 0 & 0 \\ 0 & 1 & -2 & -1 \\ 0 & 0 & 0 & -1 \\ 0 & 0 & 0 & 1 \end{bmatrix} \mathbf{\Phi} \begin{bmatrix} (1/\epsilon)e_0 \\ f_0 \\ f_1 \\ f_2 \end{bmatrix} \tag{2.2}$$

subject to the initial condition $\mathbf{n_0}$. Obviously, values for $\mathbf{r}$ and $\mathbf{\Phi}$ depend on each specific system and the reaction conditions; however, these values pose no restriction on the following analysis. Also note that n_i corresponds to each species molar amount.

Because $n_s > \mathrm{rank}(\mathbf{N})$ there is a null space $\mathbf{P}$ for matrix $\mathbf{N}$ which satisfies:

$$\mathbf{N}^{n_r \times n_s}\mathbf{P}^{n_s \times n_q} = \emptyset^{n_r \times n_q} \tag{2.3}$$

in which $n_q = n_s - \mathrm{rank}(\mathbf{N})$ is the nullity of $\mathbf{N}$ and $\emptyset$ is the null matrix. To put it more physically, since the number of independent reactions is less than the number of species involved ($n'_r < n_s$), this system is expected to have invariant states [3, 141]. This is true for every physically valid RN in a closed system [45]. Identification of these invariant states leads to reducing the dynamical order of the system and essentially transforms the original system of ODEs in (2.2) obtained from molar balance equations to a system of differential-algebraic equations (DAE). Algebraic equations are obtained by multiplying the transpose of matrix $\mathbf{P}$ by the species molar amounts in vector $\mathbf{n}$ and $\mathbf{N}^T$ on both sides of (2.1) which generates new

states as linear combination of original molar quantities that have zero derivative essentially remaining constant in time.

Clearly, a subspace of this null space **P** can be defined by rows of atomic matrix associated with this RN (a matrix constructed by using the number of atoms in each species). However, the atomic matrix is not always available. Examples of atom-free stoichiometries will be presented later in this chapter. Furthermore, atom conservation relationships are not the only factor giving rise to invariant states in an RN. Such cases are not difficult to imagine, for example, consider a complex RN of several hydrocarbon molecules. While there are only two atom types in the system (C, H) several independent reactions can be constructed and so several invariant states can exist. Also it is worth to mention that the left null space of **N** can be used in studying the steady-state behavior of the associated RN and is widely used for biochemical and biological RN flux analysis [44, 150, 151], unlike here where our focus is on a transient and dynamic system. Note that in metabolic flux analysis the aim is to find the feasible region in the reaction rate space that the system can operate in but here we are studying the invariant subspace within the chemical species concentration space. Nevertheless, these two views are closely related since they both study different aspects of the stoichiometric matrix [152, 153].

There are a number of different approaches to compute the null space **P** [22, 141]. For example, there are the QR factorization or GJ elimination-based approaches suggested in [63] and [136] or the method proposed by Schuster and Hofer [152] based on convex analysis. However, for all but the last of these approaches, the invariant states produced provide little insight to RN structure and

the system's behavior. The same issue is also encountered in other cases when a purely mathematical approach is used to study a complex process model [25]. Here we make a proposition that *for every chemically balanced RN there must be a set containing n_q semi-positive vectors forming* $\mathbf{P}$ *in* (2.3) *spanning the invariant subspace*. Also, as it will be shown later, being semi-positive, these invariants facilitate their physical interpretation and can signal potential defects in the RN structure.

2.3. Convex analysis

The semi-positive criterion implies that the invariant subspace is a convex polyhedral cone and transforms the problem of finding the invariant subspace and the solution to equation (2.3) to a convex optimization problem and convex analysis based approaches can be used to tackle it [152]. Note that the invariant subspace Γ is a convex cone since it possesses two properties [26, 69]:

i) $\forall \nu \in \Gamma$ and $\lambda > 0 \quad \Rightarrow \quad \lambda\nu \in \Gamma$

ii) $\forall \nu_1, \nu_2 \in \Gamma \quad \Rightarrow \quad \nu_1 + \nu_2 \in \Gamma$

Following the work of Schuster and Hofer [152], an algorithm to find a set of semi-positive vectors as columns of $\mathbf{P}$ in (2.3) is as follows:

1. Form an initial tableau $\mathbf{T}^{j=0}$ (with elements denoted as $t_{i,j}$) by augmenting matrix $\mathbf{N}^T$ with an $n_s \times n_s$ identity matrix, $\mathbf{T}^{j=0} = [\mathbf{N}^T, \mathbf{I}]$.

2. Using the column $j+1$ in the current tableau, for every pair of elements $t_{i,j+1}$ and $t_{k,j+1}$ compute and save a new vector $\nu = \frac{|t^j_{i,j+1}|}{\text{GCF}}\mathbf{T}^j_{(k,:)} + \frac{|t^j_{k,j+1}|}{\text{GCF}}\mathbf{T}^j_{(i,:)}$ (GCF, the greatest common factor of $|t_{i,j+1}|$ and $|t_{k,j+1}|$) if

- $t_{i,j+1}$ and $t_{k,j+1}$ are both nonzero and have opposite signs.
- for every row $l \neq i, k$ in the current tableau $S(i) \cap S(k) \nsubseteq S(l)$, where $S(i) = \{h - n_r : h > n_r \text{ for which } t^j_{i,h} = 0\}$ contains column indices of zero elements of each row in the right-hand side of the current tableau.

3. Construct the updated tableau ($\mathbf{T}^{j=1}$) as the union of all vectors ν saved in the previous step and every row in the current tableau ($\mathbf{T}^{j=0}$) for which $t^j_{i,j+1} = 0$.

4. Using the updated tableau, repeat steps 2 and 3. Continue until all the elements in the left-hand side are zero (obtaining $\mathbf{T}^{j=n_r}$).

5. When the algorithm terminates, use the transpose of the right-hand side of the final tableau to define $\mathbf{P}$.

The Schuster-Hofer (SH) algorithm above, essentially picks every potential pair of elements with opposite signs in each column and adds them together with integer weights to remove the effect of the corresponding reaction in the new state's dynamics, proceeding from left to right through the tableau. Because the algorithm is limited to addition operations, the final formulation will be semi-positive combinations of original states. This algorithm guarantees finding $p \geq n_q$ semi-positive vectors, where p is the number of systematically independent generating vectors of the invariant subspace (a set of vectors defining a cone in which none can be written as a non-negative linear combination of other vectors of this cone, this property is sometimes referred to as systematic independence) or the invariant cone [26, 152].

Following the definition of a systematically independent set, the second condition in step 2 assures that no row in the final tableau can be written as a non-negative linear combination of other rows [152, 154], otherwise, redundant states will be generated. This condition will be discussed in more detail in the next chapter. Finally, one can pick n_q linearly independent vectors from the final tableau to construct matrix $\mathbf{P}$ in (2.3). As it will be shown later in the case of an archetype ALD RN, in some cases choosing such set so that every vector in this basis directly corresponds to a physical quantity in the system is not trivial. However, since vectors obtained from this method are made of non-negative integer coefficients, they are most amenable to physical interpretation.

Starting with the first tableau and applying this algorithm to the RN of Table 2.1 gives: For $\mathbf{T}^{j=0}$:

$$\mathbf{T}^{j=0} = \left[\begin{array}{cccc|ccccc} e_0 & f_0 & f_1 & f_2 & D & M & A & B & C \\ -1 & 0 & 1 & 0 & 1 & 0 & 0 & 0 & 0 \\ 2 & -1 & 0 & 0 & 0 & 1 & 0 & 0 & 0 \\ 0 & 1 & -2 & -1 & 0 & 0 & 1 & 0 & 0 \\ 0 & 0 & 0 & -1 & 0 & 0 & 0 & 1 & 0 \\ 0 & 0 & 0 & 1 & 0 & 0 & 0 & 0 & 1 \end{array}\right] \tag{2.4}$$

For $\mathbf{T}^{j=1}$:

$$\mathbf{T}^{j=1} = \left[\begin{array}{cccc|ccccc} e_0 & f_0 & f_1 & f_2 & D & M & A & B & C \\ 0 & -1 & 2 & 0 & 2 & 1 & 0 & 0 & 0 \\ 0 & 1 & -2 & -1 & 0 & 0 & 1 & 0 & 0 \\ 0 & 0 & 0 & -1 & 0 & 0 & 0 & 1 & 0 \\ 0 & 0 & 0 & 1 & 0 & 0 & 0 & 0 & 1 \end{array}\right] \tag{2.5}$$

For $\mathbf{T}^{j=2}$:

$$\mathbf{T}^{j=2} = \left[\begin{array}{cccc|ccccc} e_0 & f_0 & f_1 & f_2 & D & M & A & B & C \\ 0 & 0 & 0 & -1 & 2 & 1 & 1 & 0 & 0 \\ 0 & 0 & 0 & -1 & 0 & 0 & 0 & 1 & 0 \\ 0 & 0 & 0 & 1 & 0 & 0 & 0 & 0 & 1 \end{array}\right] \tag{2.6}$$

For $\mathbf{T}^{j=3}$:

$$\mathbf{T}^{j=3} = \left[\begin{array}{cccc|ccccc} e_0 & f_0 & f_1 & f_2 & D & M & A & B & C \\ 0 & 0 & 0 & -1 & 2 & 1 & 1 & 0 & 0 \\ 0 & 0 & 0 & -1 & 0 & 0 & 0 & 1 & 0 \\ 0 & 0 & 0 & 1 & 0 & 0 & 0 & 0 & 1 \end{array}\right] \tag{2.7}$$

For $\mathbf{T}^{j=4}$:

$$\mathbf{T}^{j=4} = \left[\begin{array}{cccc|ccccc} e_0 & f_0 & f_1 & f_2 & D & M & A & B & C \\ 0 & 0 & 0 & 0 & 2 & 1 & 1 & 0 & 1 \\ 0 & 0 & 0 & 0 & 0 & 0 & 0 & 1 & 1 \end{array}\right] \tag{2.8}$$

Applying this algorithm to RN of Table 2.1, we find two independent vectors as columns of matrix $\mathbf{P}$ in (2.3): $\nu_1 = (2, 1, 1, 0, 1)$ and $\nu_2 = (0, 0, 0, 1, 1)$. These

invariant states make physical sense: we know that two molecules of monomer species $M_{(g)}$ make up species $D_{(g)}$. We also know that A is the adsorbed form of M, and that A is completely incorporated in C, so ν_0 represents the initial and constant number of the monomer unit in the RN. ν_1 can be interpreted in the same manner by considering species B to be incorporated into C, hence the amount $n_B + n_C$ must be fixed in the system independent of the kinetic rates and process time.

2.4. Species-reaction graph

Early work on studying graphs associated with an RN stems from Othmer who examined the relationship between invariants and the RN structure for a model chemically-reacting system [125]. Craciun and Feinberg later developed a new form of SR graph to determine whether an RN has the potential of multiple equilibria in a stirred tank reactor [34]. Here, we extend this RN analysis approach to develop an alternative method to extract physically meaningful invariants for application in thin-film deposition systems RN.

To illustrate, consider a simple RN subset of the one presented in Table 2.1 consisting of the reactions involving only gas-phase species dimer $D_{(g)}$, monomer $M_{(g)}$ and surface species A. We note that the D-M-A system described is representative of a wide range of common reaction systems including the biochemical Michaelis-Menton mechanism [46].

To develop our method, we construct an SR graph in which chemical species and reactions define the nodes. Circular and square nodes denote species and reactions, respectively. Throughout this dissertation, we distinguish equilibrium (e_i)

from finite-rate (or kinetically limited) (f_i) processes using different node colors in the graphs (blue and yellow, respectively); however, as it will be shown, the distinction has no bearing on our analysis. The numbers on the edges connecting the species and reactions represent the corresponding stoichiometric coefficients of each compound participating in that reaction. Negative and positive signs determine whether the chemical species is being consumed or produced. The SR graph associated with the D-M-A reaction network is shown in Figure 2.1. In what follows the relationship between RN invariants and SR graph structure will be described. This can be used to extract the reaction invariants of any RN no matter how complex, using its SR graph.

To generalize, we consider the D-M-A reaction system with arbitrary stoichiometric coefficients, and write the molar balance equations for each species and proceed with the GJ based factorization procedure [136] to obtain:

$$\frac{d}{dt}\begin{bmatrix} n_{\mathrm{D}_{(\mathrm{g})}} \\ n_{\mathrm{M}_{(\mathrm{g})}} \\ n_{\mathrm{A}} \end{bmatrix} = \begin{bmatrix} \nu_{r,0} & 0 \\ \nu_{p,0} & \nu_{r,1} \\ 0 & \nu_{p,1} \end{bmatrix} \begin{bmatrix} (1/\epsilon)e_0 \\ f_0 \end{bmatrix} \tag{2.9}$$

$$\frac{d}{dt}\begin{bmatrix} n_{\mathrm{D}_{(\mathrm{g})}} \\ n_{\mathrm{M}_{(\mathrm{g})}} - (\nu_{p,0}/\nu_{r,0})n_{\mathrm{D}_{(\mathrm{g})}} \\ n_{\mathrm{A}} - (\nu_{p,1}/\nu_{r,1})\left[n_{\mathrm{M}_{(\mathrm{g})}} - (\nu_{p,0}/\nu_{r,0})n_{\mathrm{D}_{(\mathrm{g})}}\right] \end{bmatrix} = \begin{bmatrix} \nu_{r,0} & 0 \\ 0 & \nu_{r,1} \\ 0 & 0 \end{bmatrix} \begin{bmatrix} (1/\epsilon)e_0 \\ f_0 \end{bmatrix} \tag{2.10}$$

The two first rows are related to variant states and the dynamics of the process and

can be ignored for now. The last row corresponds to a newly defined state which is under influence by none of the reactions in the system hence is an invariant state. For the specific case of this example, inserting the original coefficients gives:

$$\frac{d}{dt}[2n_{\mathrm{D}_{(\mathrm{g})}} + n_{\mathrm{M}_{(\mathrm{g})}} + n_{\mathrm{A}}] = 0 \tag{2.11}$$

therefore,

$$2n_{\mathrm{D}_{(\mathrm{g})}} + n_{\mathrm{M}_{(\mathrm{g})}} + n_{\mathrm{A}} = w_0 \tag{2.12}$$

where the value of constant w_0 can be computed from the system's initial conditions and can be interpreted as an atomic balance on the element that is being deposited, e.g., if $\mathrm{M}_{(\mathrm{g})}$ and $\mathrm{D}_{(\mathrm{g})}$ are the gas-phase monomer and dimer of the well-known ALD precursor TMA, respectively, w_0 would correspond to the total amount of aluminum atoms in the closed system, the ALD reactor.

The same treatment can be generalized to any linear SR graph corresponding to species S_0 - S_N and terminated by those chemical species at each end. The reaction invariant then can be formulated as

$$S_N - \frac{\nu_{p,n}}{\nu_{r,n}}\left[S_{N-1} - \frac{\nu_{p,n-1}}{\nu_{r,n-1}}\left[S_{N-2} - \ldots S_0\right]\right] = \text{cons.} \tag{2.13}$$

when the first edge encountered from species S_N corresponds to $\nu_{p,n}$. We note that we can trace the path in the opposite direction (0 to N) while (2.13) still remains valid; no matter what direction we choose, passing over each reaction node the value of the first edge we encounter appears in nominator and the second in denominator of (2.13). Note that in an RN with a linear SR graph $n_s - n_r = 1$ and all reactions

are independent hence there exists exactly one invariant state. The invariant state must be and indeed is a semi-positive vector since all $\frac{\nu_{p,n}}{\nu_{r,n}}$ terms are calculated by dividing two numbers associated with a production and a consumption process that have opposite signs.

The central concept of the above analysis is that reaction invariants correspond to certain paths in the SR graph, in this case a linear terminal-to-terminal path. However, typical reaction networks describing ALD and CVD processes are far more complex than that of the Figure 2.1(top). For example, if we include the complete form of the RN of Table 2.1, we find that the SR graph shown in Figure 2.1(bottom) now includes three types of deviations from a simple terminal-to-terminal path and we need to extend the application of (2.13) to such cases as well before applying it to more complicated structures.

1. **Reaction branches** occur when there is at least one reaction in an RN producing and/or consuming more than one species. Encountering a branched reaction node, one is free to choose any of the $(p \times q) + (p \times (p-1)/2) + (q \times (q-1)/2)$ paths resulting from q reactants and p products and then consider that node an unbranched path for the purpose of invariant formulation. However, as mentioned earlier, because we are interested in those invariants in form of $w = \sum_{i=1}^{s} a_i n_i$ where $a_i \geq 0$, we must choose one of $p \times q$ paths connecting one reactant to one product resulting in $\nu_i/\nu_{i-1} < 0$ in (2.13). It will be shown later that the existence of reaction branches in a SR graph results in the presence of multiple invariant states.

2. **Species branches** occur when there is at least one species which is produced and/or consumed in more than one reaction. When encountering a species branch, one *must* take into account all branches connected to that node when using (2.13). This can be simplified by first decomposing the species with the branch to a set of fictitious subspecies to account for all the reactions affecting that species dynamic as shown in Figure 2.1. It is important to stress that because these subspecies are fictitious quantities, one cannot use (2.13) to formulate invariant states involving only one of them.

3. **Cycles** refer to paths which begin and end at the same node. Cycles correspond to an invariant state which can be formulated using (2.13) if they are *stoichiometric*, meaning $|\prod_{i=1}^{r} \nu_{reac,i}/\nu_{prod,i}| = 1$ for all reactions involved in the cycle [34].

Note that all of these cases are essentially extensions to the unbranched linear graph. To make the logic behind our treatment of species and reaction branches more clear it is helpful to take a look back at the reaction factorization approach performed in (2.10). As it was shown, the method developed for extracting the invariants from SR graph is directly based on GJ elimination procedure. For example, confronting a branch over a species node in SR graph, we *must* account for both branches in a manner analogues to an *and* operator. This is a result of branching on a species node in the SR graph implying that there is a row with more than two non-zero elements in the stoichiometric matrix which means that in order to make the off-diagonal elements zero in GJ elimination procedure, one has to do more than one

row operation. This is different than branching over a reaction node which acts as an *or* operator allowing us to choose any of the routes to trace the network. In fact, invariant formulations generated from the SR graph are nothing but the result of a specific set of matrix row operations in the reaction factorization procedure. However, finding this set of operations which results in physically meaningful invariants is tedious without using the SR graph. The convex algorithm presented above handles this situation differently by constructing and saving multiple ν vectors using all the potential elements with different signs hence considering all of the sign-changing routes on each reaction branch at each step.

Now we can compute the invariant states of the complete RN of Table 2.1. As it is shown in Figure 2.1, to simplify using (2.13) we can decompose species A and $\mathrm{M_{(g)}}$ to subspecies $\mathrm{A}=\mathrm{A}^{(0)}+\mathrm{A}^{(1)}$ and $\mathrm{M_{(g)}}=\mathrm{M}^{(0)}_{(g)}+\mathrm{M}^{(1)}_{(g)}$ which produces two invariant states, first

$$\underbrace{n_{\mathrm{M}^{(0)}_{(g)}} - \frac{-1}{1}\left[n_{\mathrm{A}^{(0)}} - \frac{-2}{1}\left[n_{\mathrm{D_{(g)}}} - \frac{-1}{2}n_{\mathrm{M}^{(1)}_{(g)}}\right]\right]}_{\text{M-D-A Cycle}} + \underbrace{n_{\mathrm{A}^{(1)}} - \frac{-1}{1}n_{\mathrm{C}}}_{\text{A Species branch}} = w_0$$

which simplifies to

$$2n_{\mathrm{D_{(g)}}} + n_{\mathrm{M_{(g)}}} + n_{\mathrm{A}} + n_{\mathrm{C}} = w_0$$

The second invariant is found by choosing the (B,C) pair on f_2 reaction branch:

$$n_{\mathrm{B}} - \frac{-1}{1}n_{\mathrm{C}} = w_1$$

$$n_{\mathrm{B}} + n_{\mathrm{C}} = w_1$$

clearly, both invariant states are the same as those defined by vectors ν_1 and ν_2

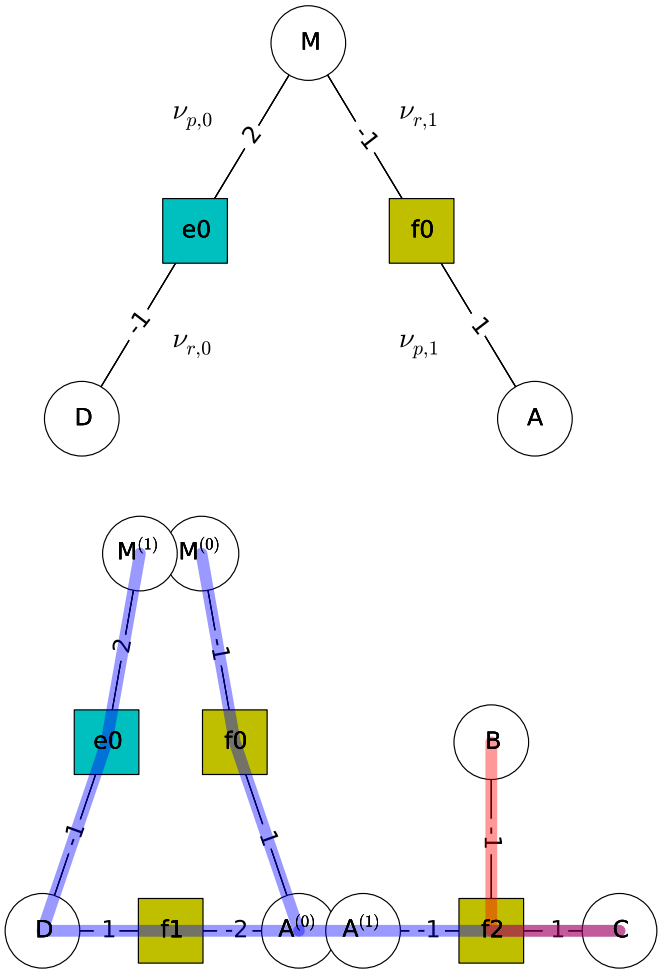

Figure 2.1: A linear terminal-to-terminal SR graph (top), and the SR graph associated with RN of Table 2.1 (bottom). $M_{(g)}$ and A species are shown as decomposed nodes to clarify the use of (2.13). The two invariant paths corresponding to invariants w_0 and w_1 are highlighted with different colors for clarity.

obtained from the convex algorithm.

2.5. Applications

The presented methods can be used to study and validate a postulated RN for a chemical process under study by answering the critical questions posed in the beginning of this dissertation, and help to identify potential inaccuracies in its structure including - but not limited to being elementally unbalanced. In what

follows the application of this approach will be illustrated in the context of three different chemical systems where invariant states with different origins are involved. The last example ends this chapter by applying our method to extract the invariant states of an archetype ALD RN, and illustrates how the presence of surface-related invariant states can be used to investigate whether the proposed RN has the potential to capture the true behavior of ALD. It is important to put emphasis on the word potential since a valid RN postulated for an ALD process might still be thermodynamically or kinetically hindered [182, 183].

2.5.1. Acid-base reaction systems

Reaction invariants have been used for pH control in acid-base reaction systems [66, 101]. Acid and base dissociation reactions typically have a very short time scale meaning that aqueous phase concentrations can be computed from the combination of reaction invariants and equilibrium relationships, with reactor dynamics governed by feed and product flow rates. In this example, we focus on extracting and physically interpreting reaction invariants in such systems.

Consider a system where acetic acid is used to neutralize sodium hydroxide in a reactor with pH as the control variable. Both acetic acid and sodium hydroxide solutions are fed to the system with time-dependent flow rates, which can be represented as finite-rate processes with net-forward reaction rates f_0 and f_1, respectively. Previously, McAvoy [109] considered this type of system to derive dynamic equations for pH control. As it can be seen in Table 2.2, the first two reactions represent transfer of acid and base to the reactor; because the system is defined as the combi-

Table 2.2: Sodium hydroxide neutralization with acetic acid (RN1) and net-forward reaction rate expressions. HAC and AC^- represent acetic acid and acetate, respectively. The artificial time constant ϵ is used to define a rate for an equilibrium process.

Reaction			Net rate, mol s^{-1} m^{-3}
HAC_f	$\rightarrow$	HAC	f_0
$NaOH_f$	$\rightarrow$	$Na^+ + OH^-$	f_1
HAC	$\rightleftharpoons$	$H^+ + AC^-$	$(1/\epsilon)e_0$
H_2O	$\rightleftharpoons$	$OH^- + H^+$	$(1/\epsilon)e_1$

nation of the reactor and feed tanks, it is considered closed. It is important to note that we differentiate the molar amount of acetic acid in the feed reservoir (HAC_f) from its amount in the semi-batch reactor (HAC) since it is a weak acid. On the other hand, there is no representation of NaOH in the reactor, as it immediately and completely dissociates in water. The third and fourth reactions represent acetic acid and water dissociation equilibrium reactions.

We can apply the same factorization procedure as in (2.10) to reduce this model and eventually decouple process time scales [136]. However, for now we keep our focus only on invariant states and proceed together with the SH algorithm to find the null space of the stoichiometric matrix. Doing so we obtain the set of reaction invariants listed in (2.14).

$$\begin{aligned}
\frac{d}{dt}\left[n_{\mathrm{HAC}} + n_{\mathrm{HAC_f}} + n_{\mathrm{AC^-}}\right] &= \frac{d}{dt}\left[w_0\right] = 0 \\
\frac{d}{dt}\left[n_{\mathrm{H^+}} + n_{\mathrm{HAC}} + n_{\mathrm{HAC_f}} + n_{\mathrm{H_2O}}\right] &= \frac{d}{dt}\left[w_1\right] = 0 \\
\frac{d}{dt}\left[n_{\mathrm{OH^-}} + n_{\mathrm{H_2O}} + n_{\mathrm{NaOH_f}}\right] &= \frac{d}{dt}\left[w_2\right] = 0 \\
\frac{d}{dt}\left[n_{\mathrm{Na^+}} + n_{\mathrm{NaOH_f}}\right] &= \frac{d}{dt}\left[w_3\right] = 0
\end{aligned} \tag{2.14}$$

It can be observed that the conserved quantities w_0, w_1, w_2, and w_3 represent

the conservation of acetate group, hydrogen ion, hydroxide group, and elemental sodium, respectively - we note that under these conservation relationships, water splits into H^+ and OH^-. We can also obtain the charge conservation invariant, which is of a great importance for pH control applications, as a linear combination of these invariants

$$\frac{d}{dt}\left[n_{AC^-} + n_{OH^-} - n_{H^+} - n_{Na^+}\right] = \frac{d}{dt}\left[w_0 - w_1 + w_2 - w_3\right] = \frac{d}{dt}\left[w_4\right] = 0 \quad (2.15)$$

which is a non semi-positive invariant generated from the original semi-positive set. This result is interesting since at first glance it illustrates a physically-relevant invariant state which is not a direct outcome of the convex algorithm, but has to be represented as a linear combination of other vectors obtained. However, charge invariant can be obtained directly as a semi-positive vector in electrochemical systems by considering the conservation of valence electrons in the system [152].

The semi-positive invariants also can be obtained from the corresponding SR graph shown in Figure 2.2. We can obtain the acetate conservation invariant, w_0, by applying (2.13) on the path starting with HAC_f to AC^-, as shown in Figure 2.2 (top). For the hydrogen ion conservation invariant, we encounter a species branch, in which H^+ is produced in both the e_0 and e_1 reactions. In this case, all branches must be considered, and (2.13) will be applied to each branch individually. This is illustrated in Figure 2.2 (bottom), where the two highlighted paths are added to obtain the hydrogen ion conservation invariant w_1. We can also formulate an invariant from the path starting with $NaOH_f$ to H_2O with a species branch on hydroxide node resulting in w_2. This can be added to w_1 to obtain a true elemental hydrogen

conservation invariant. For the sodium conservation, a terminal-to-terminal path is taken, starting from $NaOH_f$, and ending with Na^+.

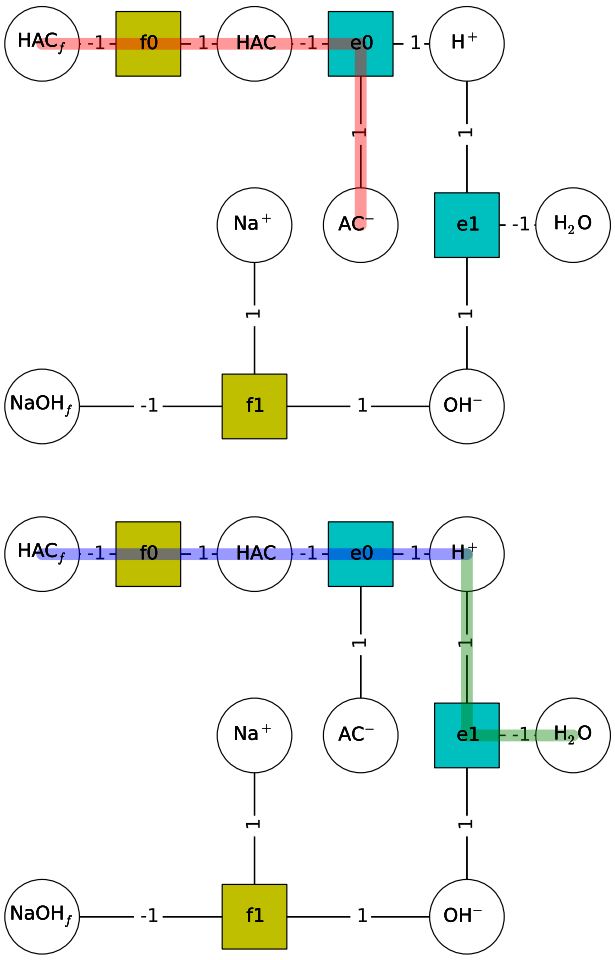

Figure 2.2: SR graph for sodium hydroxide neutralization with acetic acid showing paths corresponding to acetate group conservation (top), and hydrogen ion conservation (bottom).

McAvoy [109] considered this system for pH control; however, water was not included as a species in the initial problem formulation. Instead, water equilibrium equation with water concentration embedded in the equilibrium constant K_w was used to overcome the challenge of writing a material balance equation for hydrogen. Applying the SH algorithm to that simplified system generates the set of invariants

in (2.16).

$$\begin{aligned} n_{\mathrm{HAC}} + n_{\mathrm{HAC_f}} + n_{\mathrm{AC^-}} &= w_5 \\ n_{\mathrm{Na^+}} + n_{\mathrm{NaOH_f}} &= w_6 \end{aligned} \tag{2.16}$$

The number of semi-positive invariants obtained for this case is less than the dimension of the null space $\mathbf{P}$ ($n_s - \mathrm{rank}(\mathbf{N}) = 3$). This means that one of the basis vectors of the invariant subspace is not semi-positive, which signals a defect in the postulated RN. A defect can be anything that prevents a proposed RN from being physically feasible, such as inaccurate stoichiometric coefficients or inconsistent molecular fragments. Indeed, it can be seen that hydrogen and hydroxide groups are not conserved when H_2O in not considered in this system's representation as done in the approximation made by [109]. This result can also be obtained from the SR graph where removing the H_2O node results in losing the two invariants corresponding to the paths ending at that node. This analysis demonstrates that by focusing on semi-positive reaction invariants, one can capture defects or incompleteness in a proposed RN.

2.5.2. The Brusselator

The Brusselator model was first proposed by Prigogine and coworkers at the Free University of Brussels as an example of an oscillating reaction system [62,160]. Oscillating systems are characterized by autocatalytic reactions, in which some of the reaction products are reactants as well, as is the case for species X in RN2 of Table 2.3.

Even though the Brusselator is presented as an atom-free system (the elemental

Table 2.3: Brusselator model reactions (RN2) and net-forward reaction rate expressions.

Reaction	Net rate
$\mathrm{A} \rightleftharpoons \mathrm{X}$	f_0
$2\mathrm{X} + \mathrm{Y} \rightleftharpoons 3\mathrm{X}$	f_1
$\mathrm{B} + \mathrm{X} \rightleftharpoons \mathrm{Y} + \mathrm{D}$	f_2
$\mathrm{X} \rightleftharpoons \mathrm{E}$	f_3

compositions of species A, X, Y, B, D, and E are not specified), applying the SH algorithm reveals interesting information about the conservation relations implicitly defined by this RN. For this RN the algorithm generates two vectors that give:

$$\begin{aligned} n_{\mathrm{A}} + n_{\mathrm{X}} + n_{\mathrm{Y}} + n_{\mathrm{E}} &= w_0 \\ n_{\mathrm{B}} + n_{\mathrm{D}} &= w_1 \end{aligned} \tag{2.17}$$

It can be deduced from the first, second, and last reactions in RN2 that the species A, X, Y, and E are isomers; hence the conserved quantity w_0 corresponds to the elemental balance for these isomers. Similarly, from the third reaction, B and D are also isomers, which is captured in the invariant w_1.

This set of reaction invariants can also be extracted from the SR graph shown in Figure 2.3. Following the terminal-to-terminal path starting with D and ending with B produces w_1. For w_0, we trace the highlighted path starting with A and ending with E. Note that in this case we encounter a species branch at node X, which requires defining the subspecies $\mathrm{X}^{(0)}$ and $\mathrm{X}^{(1)}$ to account for all branches. It is important to note that the invariants are not connected to the self-oscillating behavior of this system as oscillations occur for a specific range of reaction rates, and the reaction invariants are rate-independent.

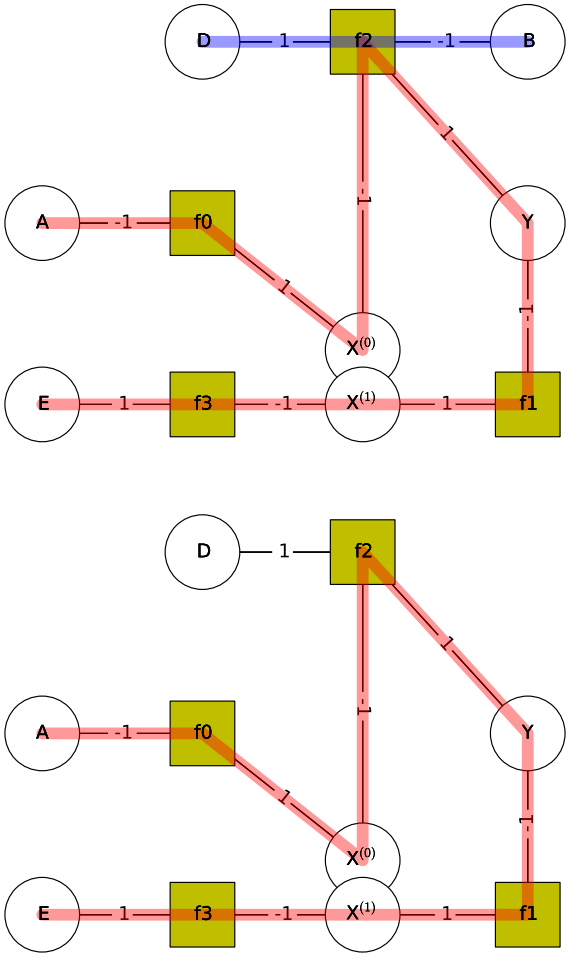

Figure 2.3: SR graph for the Brusselator model of RN2 with X species decomposed to $X^{(0)}$ and $X^{(1)}$ (top), and an altered, intentionally atomically unbalanced variation (bottom).

The atomic balance of an RN must hold even in atom-free formulation. Herein, we show that by examining the SR graph, one can identify possible defects in the network. To illustrate, let us consider a modified version of RN2, shown in Figure 2.3 (bottom), in which we remove the species B from the third reaction. With five species present in the new system and four independent reactions, one expects one invariant state. Indeed, by applying the SH algorithm or tracing the path highlighted in Figure 2.3 (bottom), we obtain w_0 invariant in (2.17). This might

suggest that this network is physically valid; however, as can be seen in Figure 2.3 species D is not included in the highlighted path of that invariant. This points to a defect in the modified RN because every atom participating in the RN must be conserved so every species must belong to at least one invariant in a closed system. One might suggest following the path starting from species D to A, however, this will produce an invariant state with only one of the subspecies of decomposed X. This result makes physical sense since the modified RN2 suggests that X and Y are isomers in the second reaction, and at the same time prevents them from being isomers through the third reaction (without the presence of species B). This type of observation may be hidden in a complex RN where it would be challenging to extract and verify conservation relations. This is particularly true for an atom-free RN, where the construction of the atomic matrix is not possible.

2.5.3. Archetype atomic layer deposition

In this example we apply our reaction invariant identification methods to an archetype metal-oxide ALD process RN consisting of the following overall reaction between a metal-containing precursor $L_2M_{(g)}$ and water to produce a metal-oxide film MO and gas-phase by-product $HL_{(g)}$:

$$L_2M_{(g)} + H_2O_{(g)} \quad \rightarrow \quad M_{(b)} + O_{(b)} + 2HL_{(g)}$$

This reaction network is consistent with the schematic of Figure 1.2 and can represent, for example, the ALD of ZnO from diethyl zinc (DEZn) and water precursors [5, 53, 183]. Using available information on the electronic structure of typical metal-oxide precursor molecules and quantum-level calculations, one can postulate

the elementary reaction network RN4 given in Table 2.4. A more complicated RN of titania ALD process can be found in [143]. The first three reactions of Table 2.4

Table 2.4: Archetype metal-oxide ALD process reactions and net-forward rate expressions (RN4). ‡ sign denotes a critical complex. Gas-phase and bulk-film species are explicitly denoted by (g) and (b) subscripts, respectively, while all others are surface species.

Reaction			Net rate mol s^{-1} m^{-2}
$L_2M_{(g)} + 2S + HO$	$\rightleftharpoons$	L_2MHO	f_0
L_2MHO	$\rightleftharpoons$	$L_2MHO^{\ddagger}$	$(1/\epsilon)e_0$
$L_2MHO^{\ddagger}$	$\rightarrow$	$LM + O_{(b)} + HL_{(g)} + S$	f_1
$H_2O_{(g)} + LM$	$\rightleftharpoons$	H_2OLM	f_2
H_2OLM	$\rightleftharpoons$	$H_2OLM^{\ddagger}$	$(1/\epsilon)e_1$
$H_2OLM^{\ddagger}$	$\rightarrow$	$HO + M_{(b)} + HL_{(g)} + S$	f_3

represent the metal-containing precursor half-reaction of the ALD process. This sequence of reactions begins with the reversible adsorption of $L_2M_{(g)}$ onto the O of a surface hydroxyl group to produce the surface adduct L_2MHO. Additionally, two surface sites S are consumed by this reaction; this fictitious species accounts for the area on reaction surface that is sterically hindered by the metal precursor ligand L. It is important to include such species in an ALD RN since steric hindrance may be the reason for the self-saturating behavior of the process. The adsorbed adduct L_2MHO can undergo a (1-2) H-transfer reaction [37] by forming the critical complex $L_2MHO^{\ddagger}$. We note that while conventional transition-state theory (CTST) dictates this to be an instantaneous equilibrium process [92], we write the net-forward reaction rate as the finite-rate process $(1/\epsilon)e_0$ using relaxation time constant ϵ for the purpose of correctly formulating the species balances that follow. This will be discussed in more detail in the next chapter. The transition state $L_2MHO^{\ddagger}$ then can

eliminate by-product $HL_{(g)}$ and liberate an adsorption site S through reaction f_1, which leaves the permanently-bonded surface species LM and incorporates $O_{(b)}$ into the bulk film. We can consider this reaction irreversible assuming sufficient reactor exhaust rate to effectively remove all $HL_{(g)}$.

The reactions corresponding to the water exposure (second half-reaction) mirror those of the metal precursor: water adsorbs onto the reactive metal surface species ML to form adduct H_2OLM, eventually resulting in the incorporation of metal $M_{(b)}$ into the bulk film. We note that reaction rates of Table 2.4 can be generated from experimental measurements or computational chemistry based calculations [183] coupled to CTST [92] for real ALD processes (e.g., ZnO ALD).

The mechanistically simple but mathematically nontrivial model produced from species material balances corresponding to RN4 provides a representative example that can be used to illustrate the procedure of RN validation for ALD processes and check whether it satisfies the criteria of a "proper" ALD RN. Because our system can be considered closed during each cycle and because $n_r < n_s$, we expect our set of species molar balance equations to contain redundant dynamic modes because elements – and potentially other reaction quantities – must be conserved. To find the reaction invariants of this RN, we define the matrix $\mathbf{N}^T$ and proceed with the convex algorithm to find eleven rows on the right-hand side of the last tableau ($\mathbf{T}^{j=6}$). Unlike previous examples, in this case only six of the eleven vectors are linearly independent ($n_s - \text{rank}(\mathbf{N}) = 6$). Note that we were aware that such cases might occur since the convex algorithm provides the systematically independent generating set of the invariant cone, a set of vectors in which no state can

be described as a positive linear combination of others, and this is clearly a loose condition compared to complete linear independency. The right-hand side of the last tableau reads:

$$\mathbf{T}^{j=6} = \begin{bmatrix} 2 & 0 & 0 & 2 & 2 & 1 & 0 & 1 & 0 & 1 & 1 & 0 \\ 1 & 0 & 0 & 1 & 1 & 1 & 0 & 0 & 0 & 1 & 1 & 1 \\ 1 & 0 & 0 & 1 & 1 & 0 & 0 & 1 & 1 & 1 & 1 & 0 \\ 0 & 1 & 0 & 2 & 2 & 0 & 1 & 0 & 1 & 1 & 1 & 0 \\ 0 & 1 & 0 & 2 & 2 & 0 & 0 & 1 & 2 & 2 & 2 & 0 \\ 0 & 0 & 1 & 1 & 1 & 0 & 1 & 0 & 1 & 1 & 1 & 0 \\ 0 & 0 & 1 & 1 & 1 & 0 & 0 & 1 & 2 & 2 & 2 & 0 \\ 0 & 0 & 0 & 0 & 0 & 0 & 0 & 0 & 1 & 1 & 1 & 1 \\ 0 & 1 & 0 & 2 & 2 & 1 & 0 & 0 & 0 & 1 & 1 & 0 \\ 0 & 0 & 1 & 1 & 1 & 1 & 0 & 0 & 0 & 1 & 1 & 0 \\ 1 & 0 & 0 & 1 & 1 & 0 & 1 & 0 & 0 & 0 & 0 & 0 \end{bmatrix} \tag{2.18}$$

where the columns correspond to the species in the RN of Table 2.4 listed in the order of {$L_2M_{(g)}$, S, HO, L_2MHO, $L_2MHO^{\ddagger}$, LM, $O_{(b)}$, $HL_{(g)}$, $H_2O_{(g)}$, H_2OLM, $H_2OLM^{\ddagger}$,

$M_{(b)}\}$. A subset of six independent vectors can be obtained from this set as:

$$\mathbf{P}^T = \left[\begin{array}{c|cccccccccccc} \nu_1 & 2 & 0 & 0 & 2 & 2 & 1 & 0 & 1 & 0 & 1 & 1 & 0 \\ \nu_2 & 1 & 0 & 0 & 1 & 1 & 1 & 0 & 0 & 0 & 1 & 1 & 1 \\ \nu_3 & 0 & 0 & 1 & 1 & 1 & 0 & 1 & 0 & 1 & 1 & 1 & 0 \\ \nu_4 & 0 & 0 & 1 & 1 & 1 & 0 & 0 & 1 & 2 & 2 & 2 & 0 \\ \nu_5 & 0 & 1 & 0 & 2 & 2 & 1 & 0 & 0 & 0 & 1 & 1 & 0 \\ \nu_6 & 0 & 0 & 1 & 1 & 1 & 1 & 0 & 0 & 0 & 1 & 1 & 0 \end{array}\right] \tag{2.19}$$

These six semi-positive vectors are columns of matrix $\mathbf{P}$ in (2.3) and span the invariant subspace of RN4. ν_1 and ν_2 clearly, correspond to the invariant states related to the conservation of the ligand L and metal atom M. Note that we can designate ligand L as an "atom" because it is not further decomposed in this RN. ν_3 and ν_4 correspond to O and H elemental conservation, and ν_5 and ν_6 correspond to the reaction surface species. As mentioned earlier, an ideal ALD is a dynamic process where the surface repeatedly evolves in a cyclic trajectory which points to the importance of invariants for ALD RN analysis. It will be shown that the last two invariants are crucial to investigate if the RN4 can display the "proper" ALD behavior described earlier.

To graphically examine the physical meaning of the six reaction invariants, particularly the last two involving only surface species, we start with the SR graph associated with RN4 displayed in Figure 2.4. We note that equation (2.13) was derived for extracting the RN invariants resulting from the reaction factorization procedure applied to a closed system. However, it still can be applied to this case as

we can consider the ALD process during one complete ALD cycle as a closed system where gaseous precursors are not reactive towards each other in the gas phase.

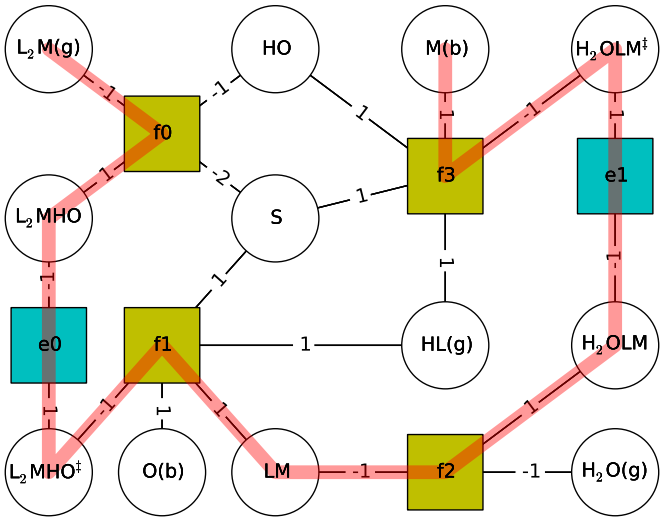

Figure 2.4: Archetype ALD SR graph illustrating the path corresponding to metal atom conservation.

As it is shown in Figure 2.4, there is a path originating from the metal gas-phase precursor $L_2M_{(g)}$ that travels through the graph following our previously stated rules, terminating at the bulk metal $M_{(b)}$. This path corresponds to the vector ν_2 and conservation of the M atoms. The invariant state associated with O atom conservation can be found as well by using (2.13), tracing a terminal-to-terminal path from the O-containing $H_2O_{(g)}$ to bulk film $O_{(b)}$ shown in Figure 2.5 giving vector ν_3. The invariants corresponding to L and H conservation can be extracted from SR graph by tracing two distinct paths starting from $L_2M_{(g)}$ and the $H_2O_{(g)}$ nodes, both ending at $HL_{(g)}$. This graphical process confirms that all elemental balances are satisfied in this RN.

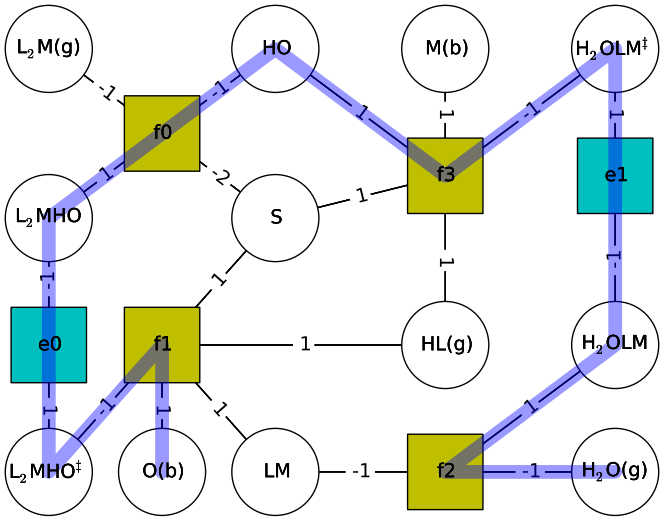

Figure 2.5: Archetype ALD SR graph illustrating the path corresponding to oxygen atom conservation.

2.5.3.1 Surface-based invariants and ALD behavior

To aid in identifying the remaining two invariants and to clarify the physical interpretation of these modes, we remove the gas- and bulk-phase species from the graph, leaving only the surface species and reactions. Furthermore, because of the reaction branches corresponding to f_0, f_1, and f_2, we can generate sub-graphs based on including/excluding the surface species S and OH - both of the sub-graphs are shown in Figures 2.6 and 2.7. The motivation for separating OH and S species comes from the fact that the self-limiting and cyclic behavior of the ALD process stems from two surface-related phenomena: consumption and later reproduction of surface active sites (OH-related), or occupying and later releasing the available space on the deposition surface (S-related) [132]. This will be discussed in more detail shortly.

Inspection of the SR sub-graph that includes S and excludes OH (Figure 2.6) reveals two interconnected cycles that define the invariant state associated with

steric hindrance effects. These cycles can be thought of as paths starting at node S and traveling counterclockwise back to S, passing through f_1 or f_3 as the last reaction before returning to S. Note that the two cycles overlap from f_0 to f_1. Both cycles can be interpreted as closed loops of reaction processes, each consuming and then producing one unit of surface area corresponding to the size of ligand L. Having three edges connected to node S and following the description of a species branch, we decompose the original S to subspecies $S^{(0)}$, $S^{(1)}$ and $S^{(2)}$ as shown in Figure 2.6. Using (2.13) for each path and adding the results (a consequence of the reaction branch at f_1), we obtain the invariant given by vector ν_5. During an exposure to the metal-containing precursor, reaction rate $f_2 = 0$, a condition corresponding to zero water adsorption rate. This effectively breaks the second cycle, resulting in the saturation of the growth surface with LM species, terminating the reaction and confirming the self-saturating nature of a true ALD RN.

The second cycle of the SR sub-graph limited to surface species and reactions does not involve node S but the surface hydroxyl HO and is shown in Figure 2.7. By following the path in this cycle, it is clear that it represents the final invariant: the conservation of surface reactive sites. The importance of this invariant state is that it guarantees the reaction surface remains bounded - that it does not grow indefinitely or vanish, a condition meaning that steady ALD cycles were not possible. As with the reaction invariant signaling self-saturating ALD behavior, this cycle also is broken when $f_0 = 0$ and/or $f_2 = 0$ corresponding to the individual precursor exposures and half-reactions. Again, upon using equation (2.13) for this path we can formulate the invariant state given by vector ν_6. Note that both invariant states

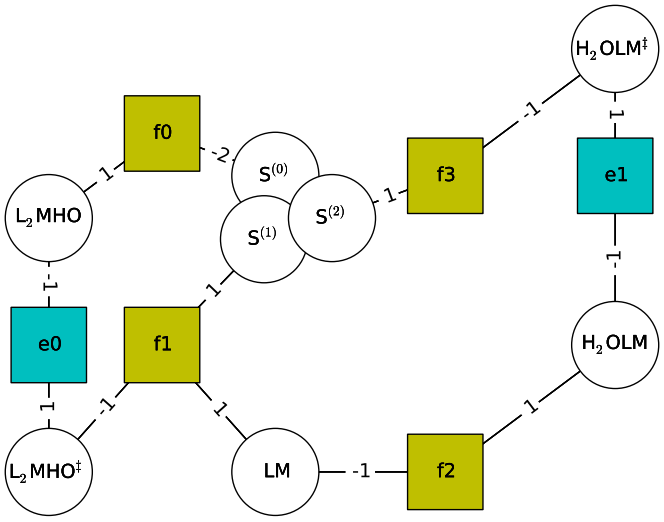

Figure 2.6: Archetype ALD SR sub-graph illustrating cyclic reaction path corresponding to surface area (steric hindrance) conservation cycles defining reaction invariant ν_5.

related to the reaction surface form a cyclic path on the SR graph.

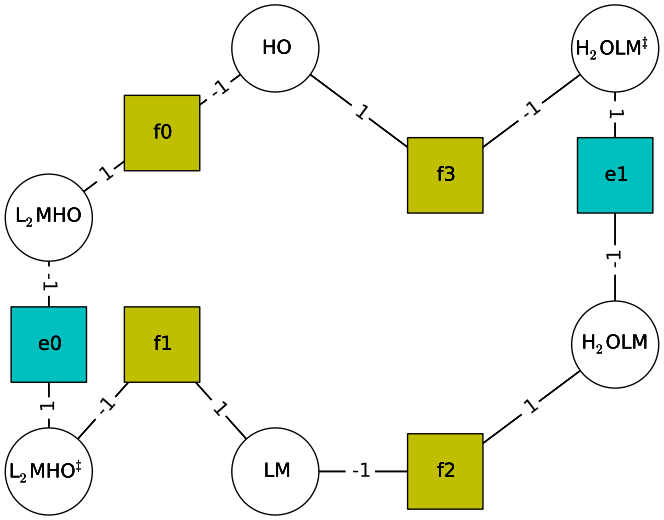

Figure 2.7: Archetype ALD SR sub-graph illustrating cyclic reaction path corresponding to surface reactive site conservation cycle producing reaction invariant ν_6.

Note that in a real process ALD half-reactions occur separately and not at the

same time. In other words, during each precursor exposure and each half-reaction only a subset of the overall RN and stoichiometric matrix is active. So considering the overall system as one RN, as we mostly did above, might be somewhat misleading. This does not change anything about the first four invariant states related to atomic balances. However, thinking in terms of separated half-cycles not only is more accurate but provides a more clear view point on the importance of surface-related states. Looking at each of the half-reactions individually, we can formulate an invariant state associated with only surface species. Of course, for the metal half-reaction this state would not involve surface species H_2OLM and $H_2OLM^{\ddagger}$ because these are not a part of that sub-RN. Same thing goes for L_2MHO and $L_2MHO^{\ddagger}$ and the water half-reaction. The fact is even for an RN which is not capable of simulating the behavior of a true ALD process such states may be formulated, however, only for a proper ALD RN these two sub-invariants are consistent and can be combined to generate an invariant state for the overall RN. In such cases the cyclic paths such as the ones shown in Figure 2.6 and 2.7 will be formed. Of course, kinetic limitations might result in for example, presence of L_2MHO on the surface during the water half-cycle but this does not mean that the proposed RN is structurally improper for describing an ALD process.

The ALD RN system illustrates the ability of SR graph to provide a framework that simplifies interpretation of the vectors obtained from SH algorithm. As an example, consider the last vector vector $\nu_{11} = (1, 0, 0, 1, 1, 0, 1, 0, 0, 0, 0)$ obtained from the final tableau for this RN provided in (2.18). This corresponds to a path on SR graph from terminal node $L_2M_{(g)}$ to $O_{(b)}$. This is a terminal-to-terminal path

with a reactant/product pair selected on f_1 reaction node that is different from the one used to generate vector ν_2. This new path meets the criteria of semi-positive integer coefficients, but the formulated invariant does not correspond to a conserved mode with significant physical consequence.

2.5.3.2 Film composition

The first four invariant states ν_1 to ν_4 confirmed that the proposed RN is indeed elementally balanced. The last two invariant states ν_5 and ν_6 confirmed that RN4 has the potential of capturing the self-limiting and cyclic behavior of the ALD process. Another question that remains to be answered is whether this RN results in a film with correct stoichiometry. Same as some of the criteria of a proper ALD RN, this can be answered by other means, however, it is constructive to study the application of the associated SR graph for this purpose.

To do so, we trace a path starting from O(b) terminal node to M(b) by passing through f_1, e_0, f_0 and f_3. Using (2.13) we obtain:

$$n_{\mathrm{O}_{(b)}} + n_{\mathrm{L_2MHO}^{\ddagger}} + n_{\mathrm{L_2MHO}} ... - n_{\mathrm{M}_{(b)}} = \text{cons.} \tag{2.20}$$

Taking the derivative of (2.20) with respect to time gives:

$$\frac{d}{dt}[n_{\mathrm{O}_{(b)}} + n_{\mathrm{L_2MHO}^{\ddagger}} + n_{\mathrm{L_2MHO}} ... - n_{\mathrm{M}_{(b)}}] = 0 \tag{2.21}$$

Integrating over a complete ALD cycle we obtain:

$$\oint dn_{\mathrm{O}_{(b)}} + \oint dn_{\mathrm{L_2MHO}^{\ddagger}} + ... - \oint dn_{\mathrm{M}_{(b)}} = 0 \tag{2.22}$$

All terms in (2.22) except those related to bulk film components $\mathrm{M}_{(b)}$ and $\mathrm{O}_{(b)}$,

correspond to surface species molar amounts which have the same value at the beginning and at the end of an ideal ALD cycle, therefore:

$$\Delta n_{\mathrm{O}_{(b)}}^{ALDcycle} - \Delta n_{\mathrm{M}_{(b)}}^{ALDcycle} = 0 \tag{2.23}$$

Equation (2.23) implies that the number of O atoms which are deposited to the film bulk phase is equal to that of M atoms regardless of number of ALD steps taken which corresponds to a film with metal atom in oxidation state +2 such as in ZnO.

Above conclusion is not trivial and in fact, not every proposed RN necessarily results in a film with correct stoichiometry; for example, at the initial stages of an ALD process the integral over the surface species molar quantities may deviate from zero due to nucleation and other nonidealities during the incubation period. To give an example of a defective RN, consider adding the following reaction to the RN of Table 2.4: LM + OH $\rightarrow$ M + $\mathrm{LH}_{(g)}$ + $\mathrm{O}_{(b)}$ This reaction may take place through the same mechanism described for the first hydrogen-transfer reaction (this reaction is indeed suggested to occur in ZnO ALD [183]). However, this reaction adds an additional fracture to the SR graph which causes a new path ending at $\mathrm{O}_{(b)}$ node with no change for $\mathrm{M}_{(b)}$ node. Decomposing species LM and $\mathrm{O}_{(b)}$ for more clear derivation we can formulate:

$$\frac{d}{dt}[n_{\mathrm{O}_{(b)}^{(1)}} + n_{\mathrm{LM}^{(1)}}] = 0 \tag{2.24}$$

$$\frac{d}{dt}[n_{\mathrm{O}_{(b)}^{(2)}} - n_{\mathrm{LM}^{(2)}}] = 0 \tag{2.25}$$

$$\frac{d}{dt}[n_{\mathrm{LM}^{(3)}} + n_{\mathrm{H_2OLM}\ldots} + n_{\mathrm{M}_{(b)}}] = 0 \tag{2.26}$$

From (2.26) and taking the same approach as above it is straightforward to show

that taking the integral over ALD cycle results in having: $\Delta n_{\mathrm{M}_{(b)}}^{ALDcycle} = \Delta n_{\mathrm{O}_{(\mathrm{b})}^{(1)}}^{ALDcycle} - \Delta n_{\mathrm{O}_{(\mathrm{b})}^{(2)}}^{ALDcycle}$ which means $\Delta n_{\mathrm{M}_{(b)}}^{ALDcycle} < \Delta n_{\mathrm{O}_{(\mathrm{b})}}^{ALDcycle}$. This does not necessarily mean the added reaction is chemically inaccurate, but does imply that the RN is defective with just this reaction alone added to it. Note that one may suggest to modify the added reaction to LM + OH $\rightarrow$ $\mathrm{M}_{(\mathrm{b})}$ + $\mathrm{LH}_{(\mathrm{g})}$ + $\mathrm{O}_{(\mathrm{b})}$ to avoid this. In that case the film stoichiometry will be satisfied; however, the invariant and the cyclic path associated with surface reactive sites will still vanish.

It also is worth highlighting the difference in the nature of surface species and bulk material molar quantity terms in this formulation where the latter acts as an accumulative variable. Therefore, analyzing the ALD RN, one must be aware of the fact that terms related to bulk material in the proposed invariants correspond to the relative change in their value with respect to the beginning of each individual ALD cycle. We also can use the same approach to check the film composition for steady state processes such as in CVD and high vacuum CVD (HV-CVD) reactors where both precursors enter the reactor continuously and simultaneously to provide steady film growth [31, 134, 135]. In this case, we may consider the continuous precursor input to the reactor to be provided by an arbitrarily large reactor vessel therefore, equation (2.13) derived for extracting the invariants of a closed system remains valid. Taking the same approach as the one used to derive (2.20), the integral over the species of the path from $\mathrm{M}_{(\mathrm{b})}$ to $\mathrm{O}_{(\mathrm{b})}$ on the graph again would be equal to zero due to the fact that in a steady state process the surface species molar amounts are constant over time, unlike the bulk quantities which continuously increase.

2.6. Final remarks

In this chapter, two methods for formulating a set of physically-relevant invariant states for a RN were presented. Specific to ALD RN analysis, it was shown that presence of consistent surface-related invariant states for both ALD half-cycles and overall RN can be used to test whether the proposed RN for an ALD process satisfies the criteria of a proper RN and can guarantee a self-limiting and stable ALD growth mode.

Concluding this chapter, there are few points that should be highlighted. Both the SH algorithm and SR graph methods can be used to identify the set of semi-positive reaction invariants describing the reaction invariant subspace. The SH algorithm automates the generation of this set, while in the SR graph method, the user analyzes the graph to extract the invariants; however, the SR graph approach facilitates the physical interpretation of the invariants by providing a better visual representation of the RN and the connection of different species. For example, in case of metabolic networks, cycles and terminal-to-terminal paths can be used to distinguish between invariants with different types related to moieties or cofactors internal to the network [44]. Another example of this was presented in section 2.5.3.1.

It is important to note that all examples considered in this chapter are treated as closed systems without any inlet/outlet streams. In open systems, the amount of each species in the system is affected not just by chemical reaction fluxes, but also by fluxes through system boundaries. The presence of inlet or outlet streams alter

the invariant subspace so that its dimension is not necessarily equal to nullity of the original stoichiometric matrix. Both the SH algorithm and the SR graph approaches can be extended to open systems as well. In the case of SR graphs, each inlet (outlet) stream can be represented by a reaction node with no reactant (product) producing (consuming) the corresponding species, where rate of that reaction represents the net feed of that species. Thus, invariants can be formulated following the same approach on the updated graph. For example, in the D-M-A RN, an inlet stream of species B will form a new reaction node connected to that species. This terminates the original terminal-to-terminal path from B to C and results in the loss of the corresponding invariant w_1. The SH algorithm also can be applied in such cases by introducing additional columns to the stoichiometric matrix for each stream as it is shown in [151]. For the purpose of RN analysis one can also assign a virtual feed tank to each stream and consider the composite system containing reactor and feed tanks closed [62, 152]. An example of taking the last approach was presented in the context of acid-base reaction system.

Chapter 3: RN Variants

3.1. Introduction

Chemical reactions are at the core of many chemical, biochemical and geochemical processes. For example, chemical industries use chemical reactions to transform raw materials into a variety of useful products, biochemical reactions are responsible for energy production and other activities in the human body, and geochemical reactions are involved in contamination and remediation processes for ground water systems and subsurface environments [20, 44, 45]. In many cases these processes consist of complex chemical reaction networks with large number of species and reactions. To understand, control and optimize these processes, and to design and develop new ones, chemical and mathematical models that accurately represent the kinetics of the RN of interest under different process conditions are desired. Development of such kinetic models can be challenging due to lack of an exact knowledge about reactions occurring in a specific system, unavailability of experimental kinetic data for many reactions, and complexities which arise as a result of usually highly interconnected nature of these RNs where the effect of different reactions are coupled through different species in the system. These issues become worse when the dynamics of the system is influenced by species transport processes such as diffusion

and convection and one has to take those into account as well [20, 22, 141].

Among the mentioned, accurate identification of reaction rates poses one of the main challenges to developing robust kinetic models. First-principles models can provide theoretical approximations for reaction rates [182], however, they usually require large amounts of computational resources, and the resulting rate expressions may have significant errors due to modeling approximations and other nonidealities.

There are in general two approaches to obtain the rate parameters and develop rate expressions for reactions in a system of interest using experimental measurements. The first, which sometimes is referred to as ad hoc modeling in the literature [45], considers the overall system and performs parameter fitting for a set of empirical or semi-empirical rate expression functions to find the appropriate set of parameters that best describe available experimental data. In this approach the effect of each individual reaction is not explicitly considered [45]. In fact, even without a complete and accurate knowledge of all reactions occurring in the system, this approach is still applicable and can be used to develop a kinetic model representative of the system's dynamics and the available experimental data. The main drawback of this approach is that the identified model probably would not be readily applicable to other systems based on that chemistry or the same system under different process conditions. The alternative is to take a reaction-based modeling approach [45]. As mentioned, in many practical cases, there is a complex RN governing the behavior of the chemical system under study and kinetic modeling and system analysis is simpler if the effect of different reactions and transport processes can be decoupled [141, 164]. In the reaction-based modeling approach the

goal is to decouple the effect of different reactions and study the rate of each process individually [22,141]. The main advantage of this approach is that the effect of each reaction is explicitly considered, therefore, there is a lower uncertainty associated with the derived kinetic parameters. The rate expressions developed by this approach may be used to study other systems which use the same chemistry or any of the individual reactions [45]. Note that an accurate description of the reactions occurring in the system is crucial for reaction-based modeling. In other words, the stoichiometric matrix associated with a system should be built a priori to kinetic modeling. Unfortunately, this information again is not always available for different chemical systems; however, there are methods to define a stoichiometry for an unknown system using limited available experimental data [25]. Also, first-principles models and computational chemistry calculations still can be used to identify potential reactions by calculating the thermodynamic and kinetic parameters of each reaction.

Decoupling the reaction rates also is necessary when studying the dynamic behavior of a chemical system. The time evolution of a system can be mathematically described by formulating a system of ODEs by using the production and consumption rates of different species in the system by each reaction. Often times, different reactions in an RN have significantly different time scales, meaning some reactions occur much faster than others which can lead to problem stiffness and a heavier computational burden. As an example of an extreme case, treating a reversible reaction with a very short time scale, the pseudo equilibrium approximation can be used to consider that reaction to be in equilibrium with respect to the more slowly

evolving state. Mathematically, the rate of such reaction can be represented using an artificial relaxation time constant $\epsilon \ll 1$. For example, for reaction A $\leftrightharpoons$ B, we will have

$$\frac{d[B]}{dt} = k_f[A] - k_r[B] = k_r(K_{equ}[A] - [B]) \tag{3.1}$$

with k_f and k_r for forward and reverse rate constants, and K_{equ} for equilibrium constant. Assuming the pseudo equilibrium approximation (very large forward and reverse rate constants), we can define the time constant ϵ and write

$$\frac{d[B]}{dt} = \lim_{\epsilon \to 0}(\frac{1}{\epsilon})(K_{equ}[A] - [B]) \tag{3.2}$$

This representation then gives rise to an algebraic equation upon taking the limit of $\epsilon \to 0$ which can be formulated using the information about the equilibrium constant. This transforms the original system of ODEs to a system of DAEs. However, due to the usual complexity of chemical systems introducing the time constant ϵ may result in a singular perturbation problem in non-standard form meaning that setting ϵ=0 in (3.2) results in the loss of information from the original ODEs [35,176]. This issue can be avoided by decoupling the fast (equilibrium) reactions from those which are kinetically limited and have a finite rate.

Furthermore, as mentioned in the previous chapter, since for an RN in a closed system the number of species present is larger than the number independent reactions, there will be redundant dynamic modes, or invariant states that remain constant throughout the process and only depend on system's initial condition. It is desirable to identify these modes which result in algebraic equations as well, be-

fore attempting to solve the systems dynamics, to reduce the number of differential equations in the model. Also, as it was shown, invariant states can be used to identify structural defects and potential inconsistencies in a proposed RN for a system under study. A complete model reduction scheme separates the effect of different reactions while formulating the physically relevant invariant states.

To achieve the aforementioned goals and facilitate the reaction-based modeling, we seek to find a transformation of the original ODE variables (original molar quantities in the system) to a new state space, where ideally the effect of all reactions are decoupled (meaning the dynamics of each of the new states is influenced/governed solely by one of the reactions), and the dynamic order of the system is reduced through the identification of RN invariants. In the previous chapter a graphical-algebraic method based on SR graphs and convex analysis was proposed to formulate the RN invariants and facilitate their physical interpretation [8, 143]. In this chapter we extend our approach to study of variant states and decoupling the reactions, therefore, finding the complete representation of the systems dynamics in the reduced form in the new state space. Furthermore, as it will be shown, the method proposed here is capable of providing all alternative representations of different variant states influenced by each individual reaction or a specific group of reactions. Such information can be useful for reaction rate parameter identification and checking the partial consistency for systems where experimental measurements are available only for a subset of species present [186].

3.2. Model development

Following the same mass conservation principle as the previous chapter, for a system with n_s species and n_r reactions the number of moles of each species changes in time due to production or consumption in different reactions, or by exchange fluxes through system boundaries. For a closed and well-mixed system then we can write

$$\frac{d\mathbf{n}}{dt} = \mathbf{N}^T \mathbf{\Phi} \mathbf{r} \quad \mathbf{n}(t=0) = \mathbf{n_0} \tag{3.3}$$

where the elements of matrix $\mathbf{N}^T$ correspond to the stoichiometric coefficients of each species in each reaction. $\mathbf{n}$ is a $n_s \times 1$ vector of the number of moles subject to the initial condition $\mathbf{n_0}$, and $\mathbf{r}$ a $n_r \times 1$ vector of reaction net-forward rates. Note that we can formulate a rate equation even for equilibrium reactions using the artificial time constant ϵ as introduced in equation (3.2). $\mathbf{\Phi}$ is a $n_r \times n_r$ diagonal matrix corresponding to reaction volume (gas phase volume for gas-phase reactions and reaction surface area for surface reactions) to make the units consistent for heterogeneous reaction systems. Following the reaction-based modeling approach, instead of directly solving the equation (3.3) transformation $\mathcal{T}$ can be applied to the original system of ODEs to give

$$\mathcal{T}\frac{d\mathbf{n}}{dt} = \mathcal{T}\mathbf{N}^T\mathbf{\Phi}\mathbf{r} = \begin{bmatrix} \mathbf{R}^{n_{r'} \times n_s} \\ \left[\mathbf{P}^T\right]^{n_q \times n_s} \end{bmatrix} \mathbf{N}^T\mathbf{\Phi}\mathbf{r} = \begin{bmatrix} \widetilde{\mathbf{I}}^{n_{r'} \times n_r} \\ \emptyset^{n_q \times n_r} \end{bmatrix} \mathbf{\Phi}\mathbf{r} \tag{3.4}$$

where $n_{r'}$ is the rank of the stoichiometric matrix or the number of independent reactions and $\emptyset$ is the null matrix. Finding such transformation $\mathcal{T}$ is desirable since it reduces the dynamic order of the model by identifying the invariant states

through matrix $\mathbf{P}^T$. Furthermore, by applying such transformation, in an ideal case, effects of different reactions are decoupled in the new states dynamics through matrix $\mathbf{R}$. As previously mentioned, this facilitates the analysis of the RN, guides in designing experiments for rate expression formulation in reaction-based modeling, and separates equilibrium from finite-rate reactions enabling the formulation of a standard singular perturbation problem.

Study of the invariant subspace and calculation of matrix $\mathbf{P}^T$ was addressed in chapter 2. It was demonstrated that for every stoichiometrically valid RN there exist a set of semi-positive vectors (in which all elements are $\geqslant 0$) to form $\mathbf{P}$, making the solution to (2.3) a convex cone [26, 152]. We also highlighted the importance of finding such $\mathbf{P}$ in detecting the RN structural defects, and in the physical interpretation of different invariant states.

The final element of the transformation matrix $\mathcal{T}$ is $\mathbf{R}$. Again, one can perform GJ elimination to determine $\mathbf{R}$ as in the reaction factorization approach suggested in [3, 45, 136]. Note that the complete decoupling of reactions can be achieved if all of the reactions in the system are independent and $n_r = n_{r'}$. In that case, $\mathbf{R} = (\mathbf{N}\mathbf{N}^T)^{-1}\mathbf{N}$ is the Moore-Penrose left pseudoinverse of $\mathbf{N}^T$ [141] and applying the transformation $\mathcal{T}$ results exactly in the identity matrix $\mathbf{I}^{n_r \times n_r}$ in the right-side of (3.4).

Finding both $\mathbf{R}$ and $\mathbf{P}^T$ completes the transformation and applying the singular perturbation formulation, the resulting system of DAEs can be solved to simulate the dynamics of the system. However, note that all available methods such as those based on GJ elimination provide only a specific set of vectors to define matrices $\mathbf{R}$

and $\mathbf{P}^T$ while there are indeed infinite choices to define those as any linear combination of their rows can be used to form a new basis for both variant and invariant subspaces. For example, following the procedure of (2.10) and performing GJ elimination for reaction factorization [3, 136], the final form of the transformation $\mathcal{T}$ directly depends on the initial setup of the stoichiometric matrix, or essentially the order in which reactions and species are indexed. This might not be an issue if the sole purpose of the model reduction is for dynamic simulation, however, alternate basis vectors for defining the variant and invariant states can be helpful in the physical interpretation of these states (as it is previously shown for the case of invariant states). Furthermore, there is value in having information about different variant states dynamically associated with only a specific reaction (or potentially set of specific reactions) for the purpose of reaction-based modeling and designing new experiments to measure the rate of that reaction and ultimately formulate a rate expression. Such information is embedded in alternate bases and essentially different representations of matrix $\mathbf{R}$.

3.3. Convex analysis

Here we extend the convex analysis based algorithm proposed by Schuster and Hofer [152], originally developed for formulating a semi-positive basis set for invariant subspace, to extract the variant states of an RN as well. More importantly, as it will be shown, the method proposed here systematically provides semi-positive vectors associated with all alternative states which are dynamically affected by a specific reaction rate in the system. This provides all the information necessary

for taking the reaction-based modeling approach. The modified algorithm proceeds through the same steps as the one described in chapter 2 with minor modifications to detect a set of variant states:

1. Build the set M containing the reaction or the group of reactions under study $\{r_{x_1}, r_{x_2}, ...\}$. This is an empty set when studying reaction invariants.

2. Form an initial tableau $\mathbf{T}^{j=0}$ (with elements denoted as $t_{i,j}$) by augmenting matrix $\mathbf{N}^T$ with an $n_s \times n_s$ identity matrix, $\mathbf{T}^{j=0} = [\mathbf{N}^T, \mathbf{I}]$.

3. **if** $r_{j+1} \in M$: No operation necessary for column $j+1$, neglect this column and proceed to the next tableau by forming $\mathbf{T}^{j+1} = \mathbf{T}^j$

   else $(r_{j+1} \notin M)$:

   (a) Using the column $j+1$ in the current tableau, for every pair of elements $t_{i,j+1}$ and $t_{k,j+1}$ compute and save a new vector $\nu = \frac{|t^j_{i,j+1}|}{\text{GCF}}\mathbf{T}^j_{(k,:)} + \frac{|t^j_{k,j+1}|}{\text{GCF}}\mathbf{T}^j_{(i,:)}$, if $t_{i,j+1}$ and $t_{k,j+1}$ are both nonzero and have opposite signs (GCF, the greatest common factor of $|t_{i,j+1}|$ and $|t_{k,j+1}|$).

   (b) Construct the updated tableau ($\mathbf{T}^{j+1}$) as the union of all vectors ν saved in the previous step and every row in the current tableau ($\mathbf{T}^j$) for which $t^j_{i,j+1} = 0$.

   (c) for every row l in the updated tableau ($\mathbf{T}^{j+1}$) remove that row if there exist another row z that $S(l) \subseteq S(z)$, where $S(i) = \{h - n_r : h > n_r$ for which $t_{i,h} = 0\}$ contains column indices of zero elements of each row in the right-hand side.

4. Using the updated tableau $\mathbf{T}^{j+1}$, repeat step 3. Continue until the last column on the left-side and constructing tableau $\mathbf{T}^{n_r}$.

5. For variant states formulation, those vectors which have a nonzero entry in the left-hand side in the columns associated with reactions in set M are the vectors of interest, and dynamically only affected by those reactions.

The outcome of performing these steps when M is empty is a set of semi-positive vectors obtained in the right-hand side of the last tableau as a basis set for the invariant subspace or matrix $\mathbf{P}$. New states described by these vectors show no dynamics and have a constant value during the overall dynamic process. Note that, as it is previously shown, the above algorithm generates $n_p \geq n_s - rank(\mathbf{N})$ vectors [152]. In other words, the number of generating vectors of the invariant cone is equal to or larger than its dimension. An example of such cases was the archetype ALD RN of Table 2.4.

Furthermore, the presence of step 3.c is to ensure that none of the final vectors can be represented as a positive linear combination of others, satisfying the requirement for a systematically independent set [26] and removing the redundant vectors. Comparing this step to the SH algorithm described in chapter 2, this is a different approach to remove the redundant vectors. In the previous version, the redundancy is checked before adding the two rows with elements of opposite signs and constructing the new vector ν, by not using the (i, k) pair for which $S(i) \cap S(k) \subseteq S(l)$. However, in the modified algorithm here this is implemented in the last step of tableau construction by removing the row l for which there exist a row z that $S(l) \subseteq S(z)$.

Clearly, the second approach is simpler in terms of programming and includes fewer operations. Nevertheless, it can be shown that both approaches are mathematically equivalent. The mathematical proof for the equivalency of the two approach and the guarantee for producing a systematically independent set is provided in appendices A and B.

In the case of a nonempty M, the described procedure essentially analyzes the invariant cone of a *reduced stoichiometric matrix* in which the column associated with each reaction under study is being neglected. Ultimately, for each specific reaction r_x the result of this operation is a set of semi-positive vectors defining new variant states dynamics of which is only affected by reaction r_x. Any of these vectors then can be used to define one of the rows in the variant-related part of the transformation $\mathcal{T}$, matrix $\mathbf{R}$. Having all possible options to define the variants associated with each reaction is helpful when the goal is to experimentally measure the rate of that reaction through measuring the amount of species in the system and ultimately define a rate expression. Choosing the state which contains the largest number of measurable species decreases the uncertainty in the proposed reaction rate expression and parameters. Again, the operation in step 3.c ensures that none of these new states can be written as a positive linear combination of others hence removing trivial cases which contain no new information.

If a reaction in a proposed RN is not linearly independent (i.e., the associated column in the stoichiometric matrix is not linearly independent from others), the rate of that reaction cannot be independently measured and the result of performing the algorithm will be an empty set. Note that this is more of a mathematical issue

and a dependent reaction in an RN, nevertheless, might be a chemically valid and feasible reaction. This is indeed the case for many of the biological and biochemical RNs where multiple pathways are available for production of one species [77] and $n_r > n_s$. In such cases $n_r > n_{r'}$ and no matrix $\mathbf{R}$ can be found to exactly produce an identity matrix on the right-hand side of (3.4); and for some reactions the algorithm does not provide any vector. However, to extended the algorithm to study such cases one can consider a list of pairs of reactions (e.g., r_{x_1} and r_{x_2}) in the first step and then neglect the two corresponding columns when proceeding with constructing the new tableaus. The result will be a set of semi-positive vectors defining new variant states dynamics of which is only affected by reactions r_{x_1} and r_{x_2}. This information can be used to design experiments in conditions under which one of the reactions is deactivated to measure the rate of the other. The same strategy can be used to study larger groups of reactions for highly interconnected networks if necessary. Later in this chapter, we will discuss in more detail some complications that can arise in the case of having dependent reactions in the RN, and how the algorithm can be optimized to handle such cases.

It is also worth comparing the operation during the formulation of variant and invariant states. The extended SH algorithm for variant analysis essentially terminates complete invariant state formulation procedure (by neglecting the associated column) only to find variant states related to the specific reaction of choice. As it will be shown later, this viewpoint is helpful when extracting the variant states from the SR graph associated with an RN.

3.4. Species-reaction graph

In the previous chapter, we illustrated a method for extracting the invariant states of an RN from its SR graph [8,143]. An obvious approach to extend the application of SR graphs to study of variant states is to remove the reaction (or reactions) of interest (r_x) from the RN and re-construct the graph associated with the reduced RN. Using equation (2.13) and the described procedure to handle deviations from a simple linear SR graph (branches and cycles), invariant paths associated with the reduced RN can be found. These new invariant states (paths) fall into one of two categories regarding to the removed reaction: 1) either they are dynamically insensitive to r_x which means these states are invariants of the original RN as well, or 2) they are variant states of the original RN affected only by r_x. The main issue with this approach is that one needs to repeatedly find and formulate the invariant paths of the reduced graph when studying each individual reaction.

A second and more efficient approach is to use the fact that all variant states are indeed embedded in the invariant states of the original graph. This is because variant states can be considered as invariant states for the reduced RN, and an invariant of the original RN is for sure an invariant state for the reduced RN as well.

The paths associated with different invariant states of the original SR graph can be used to study variants related to each reaction r_x instead of re-examining the complete reduced graph repeatedly. Those invariant paths that do not cover the part of the graph where reaction r_x node lies can be simply ignored. For the rest, r_x node should be removed from the invariant path to produce a *reduced path* which later

will be examined using the same invariant extraction rules previously developed. Resulted invariant states of this reduced path are variant states associated with reaction r_x.

Note that in both approaches we use the rules already developed for invariant state extraction on a reduced system to extract the variant states. This makes sense because variant states are invariant states for the reduced system. However, the second approach is more efficient since only small parts of the original SR graph must be re-analyzed (reduced invariant paths), while in the first approach the reduced graph itself must be examined to study each reaction's variant states.

To better illustrate the logic behind this approach, it is helpful to look back at the extended SH algorithm. The algorithm enforces zero entries in all elements in the left-hand side of the last tableau except those in the column associated with the reaction of interest r_x. Finding zero entries in that column as well (without enforcing it through step 3) implies that, r_x is not independent, and all vectors constructed in the right-hand side are invariant states and dynamically insensitive to all reactions, even r_x. However, if nonzero entries are present in the associated column there must be at least one entry with positive and one with negative sign in that column. In other words, in a valid RN if reaction r_x is independent, there should be at least one semi-positive variant state consumed by that reaction and one produced (This can be easily proven by looking at the GJ elimination procedure of (2.10) and performing that procedure while having the reaction of interest in the first column). Rows with changing signs can then be added together following the SH algorithm to make an invariant state. The presence of rows with different sign

entries at reaction r_x column in the left-side implies that there are variant paths embedded in each invariant path which is the core idea behind the second approach. Again, the advantage of taking this approach is that all variant states associated with different reactions can be extracted by analyzing the available invariant paths of the complete SR graph. The same idea can be used to study variant states associated with a pair of reactions (e.g., r_{x_1} and r_{x_2}) or larger groups.

3.5. Application

To illustrate the application of the proposed methods consider the RN presented in Table 3.1 describing the liquid oxidation of propane (Prop) with oxygen to produce water, acetone, isopropanol (iPrOH) and acetaldehyde (Acet). This is a simplified case of a more general RN suggested by Björnbom [24, 25].

Table 3.1: Reactions and net-forward rates for the simplified RN of liquid oxidation of propane with oxygen.

Reaction			Net rate, $s^{-1}\ m^{-3}$
$C_3H_8 + O_2$	$\rightleftharpoons$	$(CH_3)_2CO + H_2O$	f_0
$4\ C_3H_8 + 5\ O_2$	$\rightleftharpoons$	$6\ CH_3CHO + 4\ H_2O$	f_1
$2\ C_3H_8 + O_2$	$\rightleftharpoons$	$2\ C_3H_7OH$	f_2

This RN contains 6 chemical species and 3 linearly independent reactions ($rank(\mathbf{N}) = 3$). Therefore, there are 3 invariant states expected. Furthermore, since all reactions are linearly independent there should exist a transformation in (3.4) which decouples the effect of each individual reaction. The associated stoichiometric

matrix for this RN is presented in (3.5)

$$\mathbf{N}^T = \left[\begin{array}{r|ccc} \text{Prop} & -1 & -4 & -2 \\ \text{O}_2 & -1 & -5 & -1 \\ \text{Acetone} & 1 & 0 & 0 \\ \text{H}_2\text{O} & 1 & 4 & 0 \\ \text{Acet} & 0 & 6 & 0 \\ \text{iPrOH} & 0 & 0 & 2 \end{array}\right] \tag{3.5}$$

Applying the convex algorithm to this system to find the invariant states results in four vectors on the right-hand side of the last tableau as generating vectors of the invariant cone: $p_1 = (3, 0, 3, 0, 2, 3)$, $p_2 = (0, 6, 6, 0, 5, 3)$, $p_3 = (0, 6, 0, 6, 1, 3)$ and $p_4 = (1, 0, 0, 1, 0, 1)$. Any linearly independent subset of three from these can be used to define the null space of $\mathbf{N}$, or the invariant subspace. Note that vectors, p_1, $2(p_1 + p_4)$ and $(p_2 + p_3)/6$ correspond to the conservation relations of C, H and O atoms in the system which was expected since the RN is stoichiometrically balanced.

Figures 3.1 to 3.4 show the SR graph associated with the RN of Table 3.1. Highlighted paths correspond to the invariant states which can be formulated by tracing each path and using equation (2.13). For example, using the highlighted path in Figure 3.1 and decomposing the propane species node we obtain

$$\begin{aligned} n_{\text{iPrOH}} - (\frac{2}{-2}) n_{\text{Prop}^{(0)}} &= \text{cons.} \\ n_{\text{Prop}^{(1)}} - (\frac{-4}{6}) n_{\text{Acet}} &= \text{cons.} \\ n_{\text{Prop}^{(2)}} - (\frac{-1}{1}) n_{\text{Acetone}} &= \text{cons.} \end{aligned} \tag{3.6}$$

where $\text{Prop}^{(i)}$ is a fictitious sub-species accounting for the consumption of propane

in multiple reactions. Adding the three expressions in (3.6) to get $n_{\text{Prop}} = n_{\text{Prop}^{(0)}} + n_{\text{Prop}^{(1)}} + n_{\text{Prop}^{(2)}}$, and multiplying the results by three gives an invariant state similar to vector p_1 obtained from the convex algorithm.

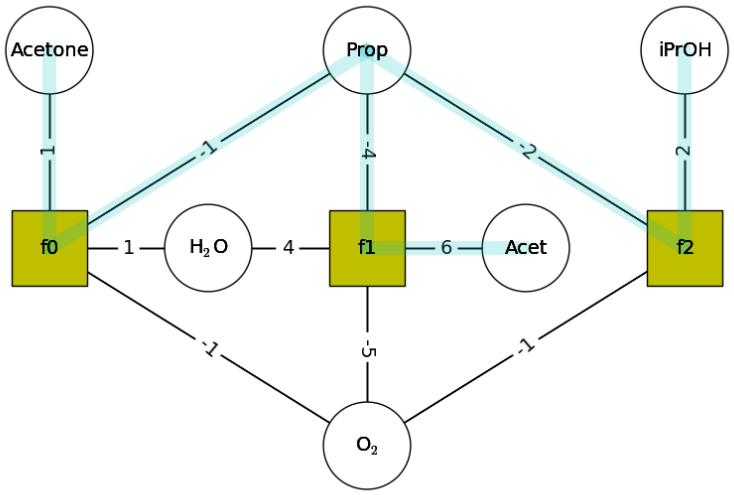

Figure 3.1: SR graph associated with the RN of Table 3.1 describing the liquid oxidation of propane (Prop) with oxygen to produce water, acetone, isopropanol (iPrOH) and acetaldehyde (Acet). The highlighted path can be used to formulate the semi-positive invariant state corresponding to vector p_1 using equation (2.13).

The other three states described by vectors p_2, p_3 and p_4 can be obtained from the SR graph with taking a similar approach and tracing the highlighted paths in Figures 3.2 to 3.4.

For variant states corresponding to each of the reactions, the algorithm provides four states associated with f_0 and f_1 and five with f_2; all are provided in appendix C. For example, four linearly independent states with dynamics regulated only by reaction f_0 are listed in (3.7). Note that for the purpose of model reduction one can choose any of these vectors to describe a row in the transformation matrix $\mathcal{T}$. On the other hand, designing experiments for rate measurements one chooses

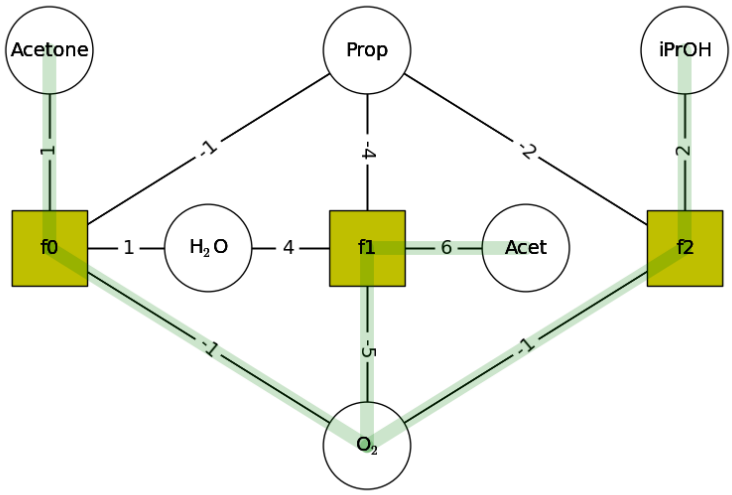

Figure 3.2: SR graph associated with the RN of Table 3.1. The highlighted path can be used to formulate the semi-positive invariant state corresponding to vector p_2 using equation (2.13).

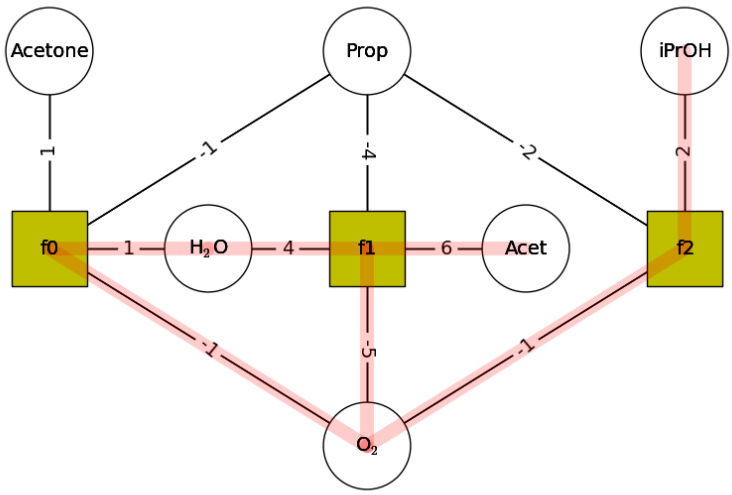

Figure 3.3: SR graph associated with the RN of Table 3.1. The highlighted path can be used to formulate the semi-positive invariant state corresponding to vector p_3 using equation (2.13).

the state that corresponds to readily measurable species in the system.

There are two approaches for identifying the variant states from the SR graphs:

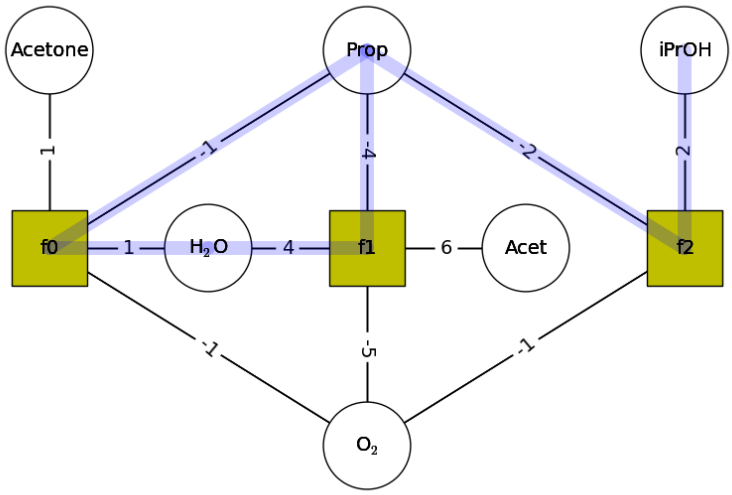

Figure 3.4: SR graph associated with the RN of Table 3.1. The highlighted path can be used to formulate the semi-positive invariant state corresponding to vector p_4 using equation (2.13).

either to remove the reaction under study from the graph and find the new paths that correspond to invariants for the reduced graph (terminal to terminals, cycles or the combination of the two), or to re-analyze the invariant paths of the original graph. The latter is more efficient since repeatedly analyzing the complete graph focusing on each individual reaction is more complicated and time-consuming compared to analyzing a set of simple invariant paths already found and shown in Figures 3.1 to 3.4. To compare the outcome of the graphical approach and the results from the convex algorithm let us focus on reaction f_0 variant states listed in (3.7). Removing the reaction f_0 and forming the reduced graph, Figures 3.5 to 3.8 highlight the parts of the reduced SR graph associated with invariants p_1 to p_4 previously shown

in Figures 3.1 to 3.4.

$$\begin{aligned}\nu_1 &= (3,0,0,0,2,3)\\ \nu_2 &= (0,6,0,0,5,3)\\ \nu_3 &= (0,4,0,5,0,2)\\ \nu_4 &= (0,0,1,0,0,0)\end{aligned} \tag{3.7}$$

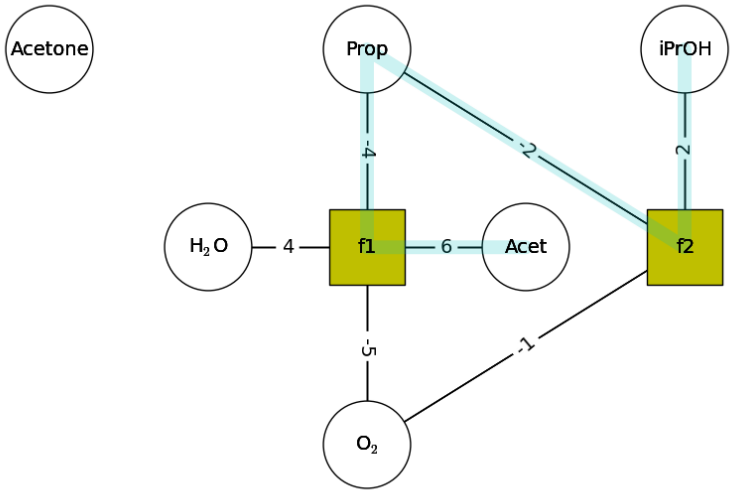

Figure 3.5: SR graph associated with the reduced RN of Table 3.1 with reaction f_0 removed. Highlighted path shows the remaining part from the invariant path of the original graph shown in Figure 3.1.

Using the remaining part of each invariant path in the reduced graph highlighted in Figures 3.5 to 3.8, and equation (2.13) we can formulate variant states associated with reaction f_0. For example, tracing the path in Figure 3.5

$$\frac{d\left(n_{\mathrm{iPrOH}} - \left(\frac{2}{-2}\right)\left[n_{\mathrm{Prop}} - \left(\frac{-4}{6}\right)n_{\mathrm{Acet}}\right]\right)}{dt} = \text{cons.} \times f_0 \tag{3.8}$$

which if multiplied by three to obtain integer coefficients gives a vector equivalent

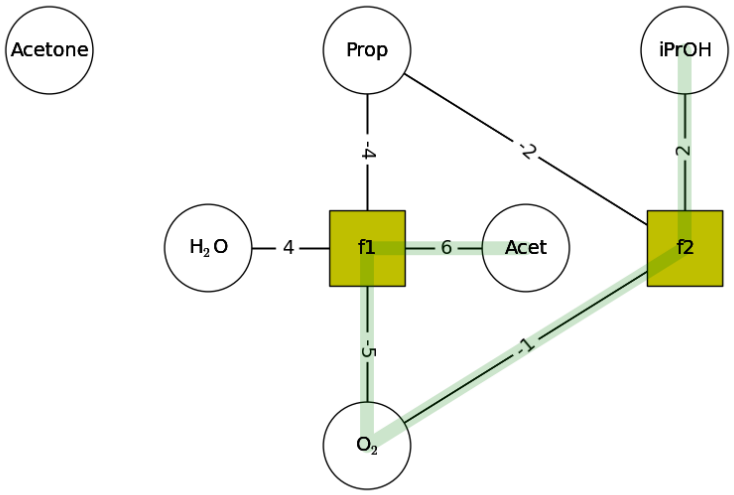

Figure 3.6: SR graph associated with the reduced RN of Table 3.1 with reaction f_0 removed. Highlighted path shows the remaining part from the invariant path of the original graph shown in Figure 3.2.

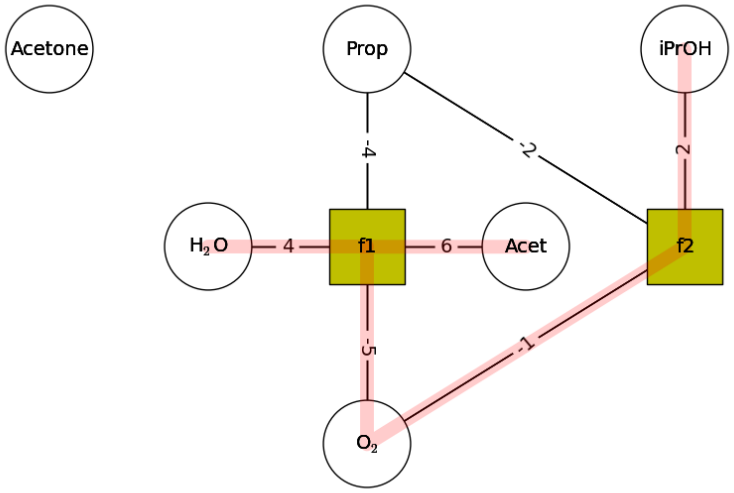

Figure 3.7: SR graph associated with the reduced RN of Table 3.1 with reaction f_0 removed. Highlighted path shows the remaining part from the invariant path of the original graph shown in Figure 3.3.

to ν_1 in (3.7) produced by the convex algorithm. Tracing the path shown in Figures

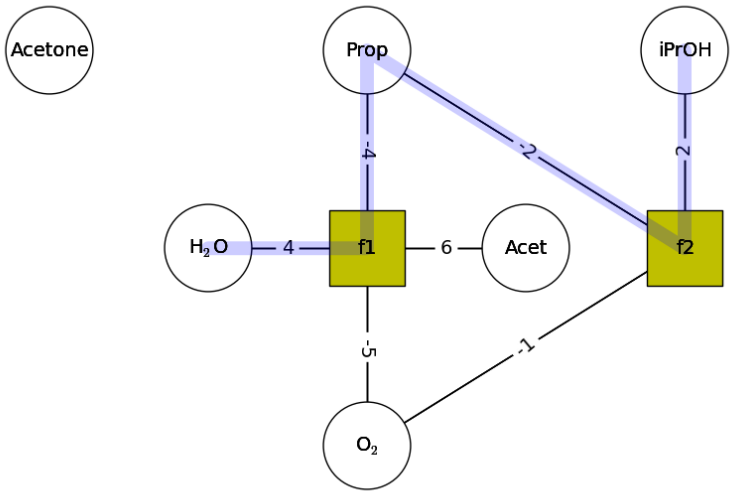

Figure 3.8: SR graph associated with the reduced RN of Table 3.1 with reaction f_0 removed. Highlighted path shows the remaining part from the invariant path of the original graph shown in Figure 3.4.

3.6 and 3.7 we find

$$\begin{aligned} \frac{d\left(n_{\mathrm{iPrOH}} - \left(\frac{2}{-1}\right)\left[n_{\mathrm{O_2}} - \left(\frac{-5}{6}\right)n_{\mathrm{Acet}}\right]\right)}{dt} &= \text{cons.} \times f_0 \\ \frac{d\left(n_{\mathrm{iPrOH}} - \left(\frac{2}{-1}\right)\left[n_{\mathrm{O_2}} - \left(\frac{-5}{4}\right)n_{\mathrm{H_2O}}\right]\right)}{dt} &= \text{cons.} \times f_0 \end{aligned} \tag{3.9}$$

which correspond to vectors ν_2 to ν_3, if multiplied by appropriate coefficients to give all integer values. The node associated with acetone species is also a part of invariant paths shown in Figures 3.1 and 3.2 and results in another variant state upon removing the f_0 node which is clearly equivalent to vector ν_4. This completes identifying the variant states depending only on reaction f_0 using the SR graph. Note that the invariant path shown in Figure 3.4 does not result in a new variant state upon reducing the path by removing the f_0 node (shown in Figure 3.8) and the resulting path generates an invariant vector (essentially a variant state with constant value of zero). This is a result of having a stoichiometric cycle formed between f_0

and f_1 nodes. The value of the constants in (3.8) and (3.9) for variants associated with ν_1 to ν_4 are -3, -6, 1 and 1 respectively, calculated using the stoichiometric matrix.

Numerical representation

To illustrate that the dynamics of the newly defined variant states described by vectors ν_1 to ν_4 solely depends on reaction f_0 we can compare the time derivative of these new states with f_0 reaction rate. Figure 3.10 shows the time derivative of the proposed variant states obtained by numerically solving the original ODEs of species mass balances for a set of arbitrary initial conditions and known reaction rates provided in appendix D. In each plot the circle markers represent the data points obtained from the numerical solution to the ODE (shown in Figure 3.9), and the highlighted area corresponds to the rate of reactions directly calculated from their rate expression equation multiplied by the right constant similar to equation (3.8). As it can be seen in Figure 3.10, the dynamics of different variant states generated by the algorithm and SR graph for each reaction f_0, f_1 or f_2 are indeed governed only by the corresponding reaction as expected, confirming that they can be used to formulate and optimize a rate expression equation for each individual reaction. In each case the other two reaction rates are plotted for comparison.

3.6. Application to ALD

Unlike invariants, the proposed approach for variant states analysis does not have any implication specific to ALD process. Furthermore, as it was mentioned, obtaining accurate experimental data from this heterogeneous and dynamic system

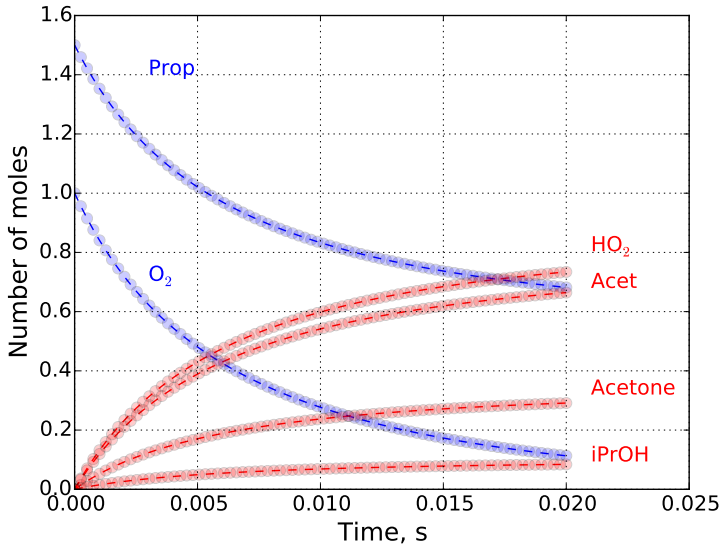

Figure 3.9: Raw data points obtained from numerical solution to the mass balance system of ODEs using the arbitrary initial condition and reaction rate parameters listed in appendix D.

is a major challenge in ALD process modeling which makes accurate reaction-based modeling using experimental data difficult. However, it still is worthwhile to use this approach to analyze the archetype ALD RN of Table 2.4. For clarity let us focus only on variant states associated with reaction f_0. Applying the convex algorithm to this reaction results in seven states. It is particularly interesting to analyze the SR graph path associated with two of the states. Figure 3.11 shows two paths corresponding to variant states of f_0. The variant path highlighted in blue contains species $L_2MHO^{\ddagger}$, L_2MHO and $O_{(b)}$. One can approximate the concentration of the transition state $L_2MHO^{\ddagger}$ to be zero meaning that by measuring species L_2MHO and $O_{(b)}$ one can measure the rate of reaction f_0. This result makes physical sense since all the atoms which are incorporated into the film or are chemically bonded to the surface must first adsorb on the surface and pass from reaction f_0. There are

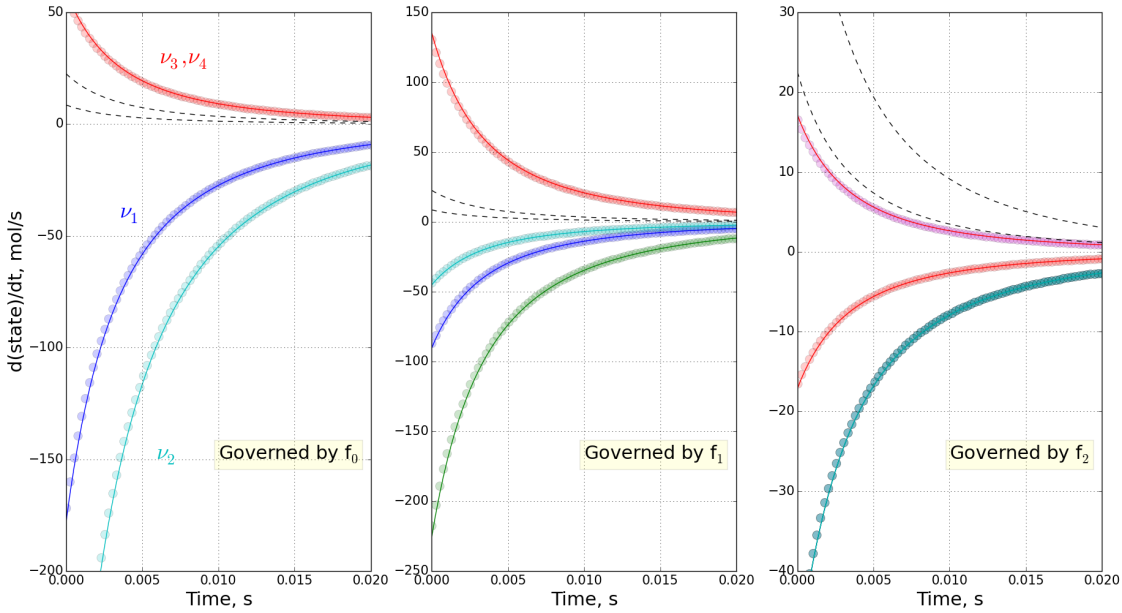

Figure 3.10: Time derivative of different variant states associated with each individual reaction shown with circle markers obtained from directly solving the mass balance system of ODEs (solution shown in Figure 3.9); and rate of the associated reaction multiplied by the appropriate constant shown with solid lines. The upper plot for reaction f_0, and the lower plot for f_2 encompass two and three overlapping variant states respectively. In each case the dotted lines show the rate of the two irrelevant reactions for comparison.

surface analysis methods such as Fourier-transform Infrared spectroscopy (FTIR) and Quartz Crystal Microbalance (QCM) that can aid in measuring these species; however, as mentioned, differentiating between different surface species and accurate surface concentration measurement is challenging. The second path highlighted in red illustrates a variant state which is not trivial and in fact might be surprising at first glance. All of the species in this state are products of water half-reaction; however, their combination produces a variant state associated with metal precursor adsorption. It is of course the consumption of a HO surface group that provides the link to reaction f_0. This result is interesting because gas phase analysis techniques such as Quadrupole Mass Spectroscopy (QMS) might generate more accurate data

for some gaseous molecules than others. For example, it is well-known that water molecules tend to stick to reactor walls and remain inside the vacuum deposition chamber for an extended period of time; therefore, for those systems that use water as a precursor one may not be able to accurately measure the evolution of water concentration in the gas phase. However, alternative variants can be used to relate the rate of a reaction under study to a different and more measurable gas-phase species. The same idea can be used in the experimental study of other chemical systems where accurate measurements area available only for some species in the system.

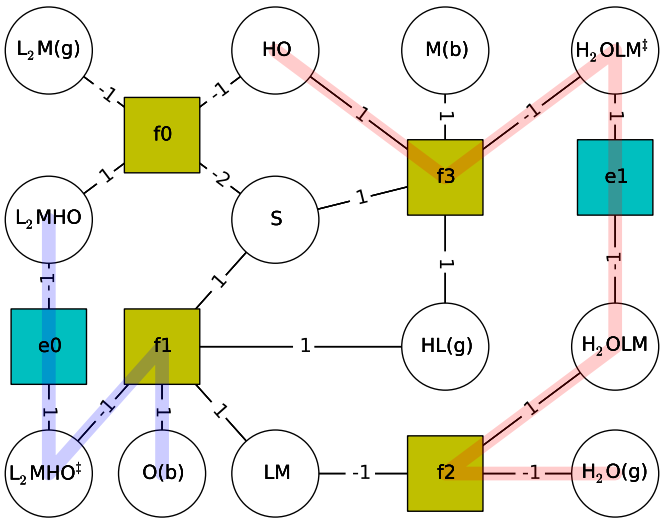

Figure 3.11: SR graph associated with archetype ALD RN. Two highlighted paths show two of the variant states associated with reaction f_0.

3.7. Final remarks

As it was shown, both the convex algorithm and SR graph methods can be used to identify invariant states of a proposed RN. It was also shown that with

small variation they also can be used to obtain sets of different variant states which are associated with individual (or potentially a group of) reaction(s) of interest in the system. Invariant states can be used to reduce the dynamic dimension of the kinetic model, and provide useful information about the physical origin of conserved quantities. Variant states which were the focus of this chapter can be used to complete the construction of the transformation matrix $\mathcal{T}$ in (3.4) and to decouple fast and finite-rate reactions. Furthermore, information about alternative variant states, which are all equally valuable for the formation of $\mathbf{R}$ in $\mathcal{T}$, is useful for reaction-based modeling in systems where only a subset of species concentrations can be experimentally and accurately measured. In these cases if the aim is to experimentally measure the rate of a reaction in the system and ultimately fit a rate expression to the data, one can use the results from this work and choose a corresponding variant state which contains the highest number of measurable species or the one that contains species that can be most accurately measured and relate them to the rate of the reaction under study. In the same manner, the complete set of invariant vectors generated by these methods can be used to check for partial consistency in such systems by checking whether the value of those invariant states for which experimental data are available remains constant during the process, an observation that can partially confirm the accuracy of the proposed RN for the system under study [45].

To conclude this chapter, there are few additional points regarding the results of the proposed methods that should be highlighted. In our approach variants are restricted to semi-positive vectors; one might ask do these necessarily cover all the

alternative variant states for each reaction under study? The answer to this lies in the fact that variant states associated with a reaction are invariant states of the reduced RN when that reaction is eliminated. As discussed in chapter 2, the semi-positive vectors generated by the convex algorithm are capable of completely describing the null space or invariant subspace ($n_p \geq n_s - rank(\mathbf{N})$). Therefore, variant states associated with each reaction are completely described by the vectors generated by the proposed algorithm as well. One can also argue that if there are variant state vectors that are not semi-positive, adding the appropriate semi-positive invariant can transform that state to a semi-positive variant.

The example RN provided in Table 3.1 did not contain any fast, equilibrium reactions and all three reactions were assumed to be finite-rate and kinetically limited processes. The presence of fast reversible reactions such as in (3.1) does not impose any restriction on our method. However, there are two points that need to be considered in such cases. First, if these reactions are approximated to be pseudo equilibrium, there is less value in finding different variant states associated with them since there will be no measurable rate, and the rate expression is replaced with an algebraic chemical equilibrium equation upon invoking the singular perturbation formulation as shown in (3.2). Note that these are essentially a pair of dependent forward and reverse reactions with very large rate constants and hence cannot be measured independently. The second point is concerned with model reduction procedure using singular perturbation formulation [3]. In the presence of equilibrium reactions in the RN, the transformation $\mathcal{T}$ to the new state space cannot result in more than one state depending completely or partially on each of the fast

reactions. Failure to satisfy this results in loosing information upon taking the limit of $\epsilon \to 0$ (nonstandard singular perturbation problem), or algebraic equations that contain two equilibrium expressions (addition of two infinite terms). In other words, all fast reactions in an RN have to be independent from one another otherwise the system is overdetermined and the postulated RN must be modified [3, 45].

Chapter 4: ALD of Indium Oxide for Electrical Modification of Spacecraft Heat Radiator Pigments

4.1. Introduction

Charged particles trapped by the Earth's magnetic field in the Van Allen radiation belts are the primary cause for the differential charging of spacecraft components. Van Allen belts can vary in shape and radiation level due to solar variations and magnetic disturbances; they generally extend from approximately 1000 km to 6 Earth radii. If not dissipated, differential charging can lead to electrostatic discharge (ESD) between high potential and low potential components in spacecraft. ESD may cause electromagnetic interference and arcing resulting in damaged integrated circuits, blown fuses, electronics failures, operational anomalies and degradation of thermal control surfaces [55, 78].

Differential charging can be a major concern in the case of nonconductive thermal control coatings used for spacecraft radiator panels. The main cause of differential charging on these components is the flux of low-energy electrons in the Van Allen belts since high-energy electrons easily penetrate the thin thermal coating

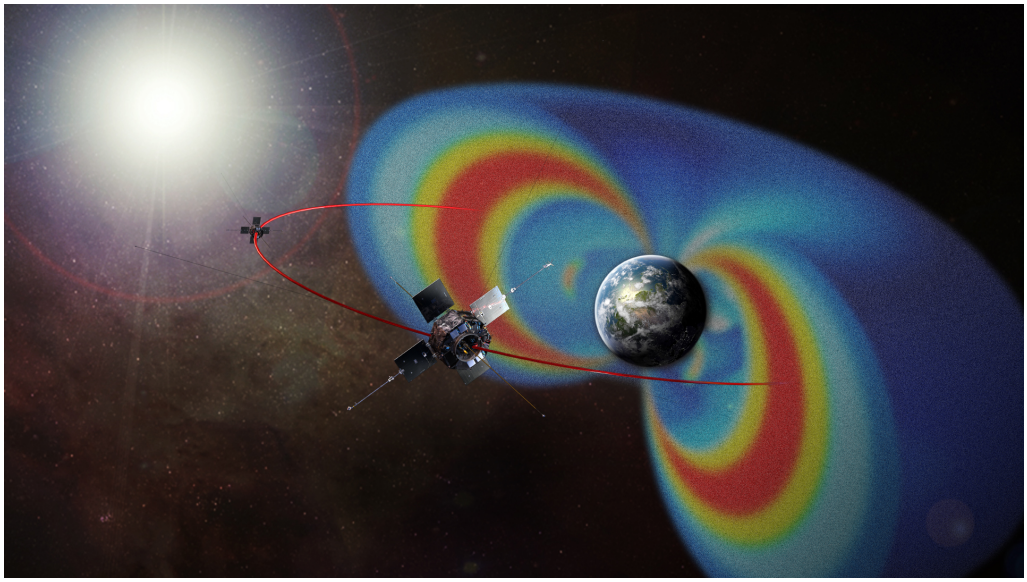

Figure 4.1: Schematic of inner and outer Van Allen radiation belts, retrieved from [189].

and so do not cause charge buildup on the surface. The buildup charge is not completely compensated by low-energy protons due to their lower flux. The level of charging depends on factors such as flux intensity, specific coating material, surface contamination, and temperature [78]. One method to reduce differential charging is to apply a thin (∼200Å) transparent conductive layer such as indium tin oxide (ITO) on nonconductive surfaces. Considering the relatively low electrical currents generated in orbit, typically 1×10^{-8} A/cm^2, coatings with the sheet resistivity less than 10^5 $\Omega/\square$ are sufficient to dissipate charge [78].

Transparent conducting oxides (TCOs) are oxide materials that conduct electricity and demonstrate high optical transparency in the visible range of spectrum. TCOs are widely used in optoelectronics applications such as flat panel displays and photovoltaics (PV) [79, 127, 188]. Indium oxide, In_2O_3 (IO), is one

of the most widely used TCOs and has been studied extensively over the past several decades [104, 107, 123, 127, 148, 159, 166, 184]. IO has relatively good electrical conductivity and high transparency, as well as mechanical and chemical stability, making it a strong candidate for its many applications in liquid crystal and touch screen displays, solar cells, organic light emitting diodes (OLED) and chemical sensors. [21, 29, 90, 99, 107, 112]. In most of these applications, however, to achieve high electrical conductivity IO is typically doped with 10 wt.% SnO_2 to produce indium tin oxide (ITO). Both IO and ITO thin-films can be grown by different methods, such as metal organic chemical vapor deposition (MOCVD) [180], electron beam deposition [82, 127, 156], sputtering [17, 29, 49, 68, 71, 87, 115, 117–119, 122, 128, 148, 188], spray pyrolysis [47, 168], pulsed laser deposition [4, 81] and atomic layer deposition (ALD) [12, 39, 40, 84, 93, 98, 107, 138].

An alternative solution to applying a conductive layer to heat radiator panels' surface is to modify the electrical properties of the thermal coating pigments before binding and spray application. The motivation for pre-processing the pigments is that this approach is not limited by the geometry of the spacecraft part to be coated, such as requiring a large deposition chamber to accommodate parts of different sizes making up the complete thermal radiator panels [74]. To achieve this goal, a deposition method is needed to conformally coat the micron-size radiator pigments. Furthermore, since the primary function of these pigments is to efficiently dissipate heat it is desired to coat them with the minimal amount of a conductive layer to avoid degradation of pigment optical properties. ALD is the natural choice for this application. Because ALD is not a line-of-sight process it is appropriate for

particle processing, furthermore, ALD offers a precise control over the thickness of the deposited film which is useful for applying the minimal level of coating to the pigment particles.

The aim of this project is to study the application of ALD to produce thin-films of IO and ITO, and investigate the thickness-dependent optical and electrical properties of the deposited film. The motivation for this is to ultimately use the optimized process to enhance the electrical conductivity of spacecraft thermal radiator pigments by applying a thin layer of a TCO coating to their surface [74]. As mentioned, to avoid disturbing the optical properties of these pigments, most importantly the emissivity, we seek to obtain the required conductivity using minimal coating. Therefore, we have limited our study to films of less than 20 nm thickness.

4.2. Materials and methods

For an ALD process to work, the precursors must meet the criteria of having sufficient vapor pressure, high thermal stability, and high reactivity towards the deposition surface [54]. Several ALD precursor systems have been used for depositing IO and ITO thin-films. In general, IO can be deposited by using a typical binary ALD process where the sources of In and O atoms are introduced to the reactor during each ALD half-cycle. For the case of ITO, a "supercycle" [103] containing a Sn source can be used to introduce Sn doping to the film. Table 4.1 lists the main IO and ITO ALD studies and the precursor system that has been used in each. Those ALD processes that use halogenated precursors typically produce corrosive byproducts such as HCl which can damage the equipment over time and potentially etch

Table 4.1: List of ALD studies of IO and ITO films. InCp refers to cyclopentadienyl indium, TMI to trimethylindium, TEI to triethylindium, DADI to [3-(dimethylamino)propyl] dimethyl indium, INCA to diethyl[1,1,1-trimethyl-N-(trimethylsilyl)silanaminato]indium, $Me_2In(EDPA)$ to dimethyl (N-ethoxy-2,2-dimethylcarboxylicpropanamide) indium, and TDMASn to tetrakis(dimethylamino)tin(IV).

Ref.	Film	Metal source	Oxygen source
Asikainen et al. [13]	IO	$InCl_3$	H_2O
Elam et al. [40]	IO	InCp	O_3
Libera et al. [98]	IO	InCp	O_2+H_2O
Lee et al. [93]	IO	TMI	H_2O
Maeng et al. [104–106]	IO	DADI,TEI,INCA,$Et_2InN(SiMe_3)_2$	H_2O,O_3
Yeom et al. [187]	IO	$Et_2InN(SiMe_3)_2$	plasma O_2
Mane et al. [107]	IO	TMI	O_3
Agbenyeke et al. [6]	IO	$Me_2In(EDPA)$	H_2O
Kim et al. [84]	IO	tris(N,N-diisopropylformamidinato)indium	H_2O
Ritala et al. [138]	IO,ITO	$InCl_3$+$SnCl_4$	H_2O_2+H_2O
Matero et al. [108]	IO,ITO	$InCl_3$+$SnCl_4$	H_2O
Asikainen et al. [12]	ITO	$InCl_3$+$SnCl_4$	H_2O
Elam et al. [39]	ITO	InCp+TDMASn	H_2O_2,O_3

the deposition surface causing non-uniformity in the film. These also often require high process temperatures [12, 138] which hinders their application to temperature sensitive substrates [107]. As a non-halogenated source, cyclopentadienyl indium (InCp) has been shown to provide an acceptable gpc at relatively low temperatures when used in combination with ozone or a water/oxygen system [40, 98]. However, InCp suffers from some drawbacks such as high cost and low vapor pressure [107].

For this study, we have chosen trimethylindium (TMI) and ozone as the In and O sources to deposit IO. This precursor system has been shown to provide acceptable gpc and saturating ALD behavior in the temperature range of 100-200 °C [107]. TMI has a relatively high vapor pressure, and does not require additional precursor source heating or a complicated delivery system. Figure 4.2 shows the TMI vapor pressure data from three sources reported in [158]. As it can be seen, TMI has a vapor pressure of about 1.8 Torr in room temperature which is sufficient for direct

draw in our reactor system. It has been reported that water also can be used as the O source with TMI, however, unless very large exposures are used, it cannot completely remove surface ligands that remain after the TMI pulse [93, 107]. Considering this and the higher reactivity of ozone as an oxidizer, ozone was chosen as the O source for this study. We also used tetrakis(dimethylamino)tin(IV) (TDMASn), which has been successfully used in SnO_2 ALD studies [32, 39], as the source for Sn atoms.

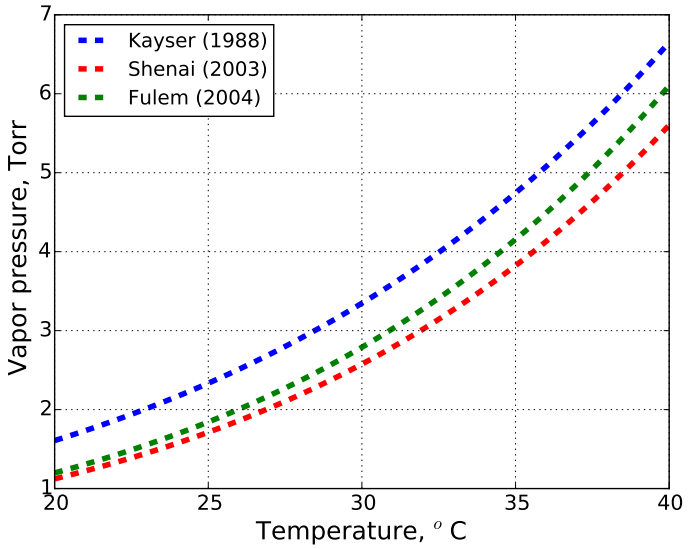

Figure 4.2: TMI vapor pressure data taken from [158].

4.2.1. Experimental procedure

Two sets of experiments were conducted in this study. First, IO and ITO films with different thicknesses were deposited on standard silicon and quartz flat substrates to investigate their thickness-dependent properties. In the next step the optimized process was used to coat commercial Z93 heat radiator pigments used in spacecraft heat radiators.

There are many groups who have successfully used ALD to coat particles with a range of size distributions for varying applications. Most of these studies have used fluidized bed (FB) reactor designs. For example, Wank et al. [181] demonstrated the application of FB reactors for ALD experiments by coating Ni particles with alumina. They used the same alumina ALD process for coating boron nitride particles to increase their adhesion to epoxy resins. Hakim et al. [67] used a FB reactor to perform ALD of alumina on nano-sized silica particles. King et al. [86] also used the same design to coat silica and titania nano-particles with zinc oxide films for applications in UV-blocking cosmetic particles. More recently Kaariainen et al. [76] used FB-ALD for coating acetaminophen particles for pharmaceutical applications. McNeary et al. [111] and Guo et al. [64] also used FB-ALD to deposit titania and alumina nanostructures for catalyst synthesis. While currently being the most promising method for large-scale ALD processing of particles, FB-ALD can require sophisticated reactor designs to assure proper fluidization of the particles and effective transport of ALD precursors. Likewise, when FB-ALD is used to coat lightweight nano-sized particles, a significant portion of each batch may be entrained in the carrier gas leading to a small recovery [83]. To avoid this issue Kikuchi et al. [83] proposed an alternative ALD reactor design where particles were fixed on a substrate by applying an electrostatic potential and were mixed by a scraper attached to a rotator. This approach was proven successful in coating gold nanoparticles with titania. Recently, van Ommen has suggested a new design for particle ALD as a continuous process by passing the particles through a tubular reactor using a carrier gas and injecting the precursors in multiple downstream injection

points [174].

For this study ALD experiments were performed in a custom designed bench-scale hot-wall reactor. A schematic diagram of the reactor and the precursor delivery system is presented in Figure 4.3. The reactor is a standard 4.5 in ConFlat stainless steel cross with an inside diameter of 2.5 in, which is wrapped by a heating jacket controlled by a PID controller, capable of providing internal temperatures up to 190 °C. A mechanical pump was used to maintain a pressure of ∼0.1 Torr inside the chamber during experiments measured by a capacitance manometer (MKS Baratron) attached to one of the axis flanges. Precursors flow individually into the reactor chamber through a multi-input flange. Each precursor line is controlled by a separate solenoid activated control valve (Swagelok) to ensure consistent and precise doses. The forth axis flange on the right can be configured for either a quick release door when depositing on flat substrates or configured for pigment particle coating via a rotary feed-through. The particles to be coated are placed inside a cylinder with the capacity to process batches of maximum 14 g, with walls consisting of a coarse mesh cage to provide rigidity and lined with a 55 micron Dutch weave mesh to prevent particles from escaping. The cylinder is capped with a KF40 aluminum flange attached to a rotating shaft. The internal shaft is attached to a Kurt J. Lesker magnetically coupled rotary motion feed-through with a co-axially mounted stepper motor. The stepper motor rotary speed is controlled by the applied voltage. The sample cylinder rotation prevents particle agglomeration and enables the precursor gases to react with the entire particle surface area. The gate valve placed on the line leading to the pump is used to isolate the reactor chamber from the pump and

to provide sufficient exposure time for reaction between the precursor molecules and the particles if needed. Our reactor design for processing the particles closely follows the one used by McCormick et al. [110].

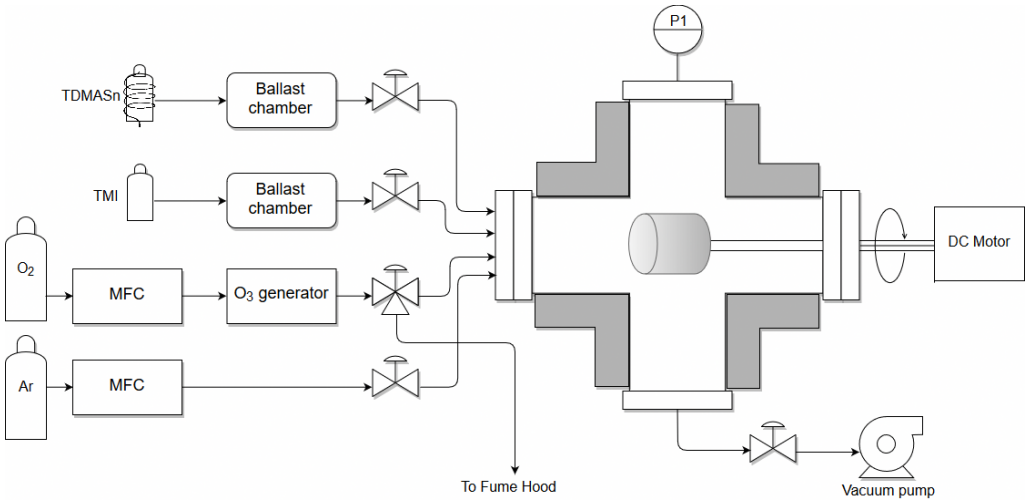

Figure 4.3: Schematic of the ALD reactor used for preparing the samples. The forth axis flange on the right can be configured for either a quick release door when depositing on flat substrates or configured for pigment particle coating via a rotary feed-through.

TMI was supplied by SAFC Hitech and TDMASn by Strem Chemicals. Ozone was produced using a bench-scale ozone generator (Absolute Ozone NANO) using a feed of industrial grade oxygen at a flow rate of 100 sccm producing ~8-10% ozone in oxygen measured using an inline microprocessor-based gas sensor (Teledyne API model 452). When not used, using a 3-way valve, oxygen flow is directed to the lab. fume hood after passing an activated carbon filter. High purity Argon (Airgas) flowing at 10 sccm was used to purge the reactor during and after precursor pulses. For flat substrate runs each precursor pulse was set to 0.1 s. TMI pulses were followed by a 20 s purge of Ar gas. A 25 s purge was used after the O_3 and TDMASn pulses. Separated heating jackets were used to heat the TDMASn precursor source

to 70 °C to provide sufficient vapor pressure for direct draw into the chamber; and to warm up its delivery line to avoid precursor condensation. 2 in Si(100) wafers with a ∼1.5 nm native oxide layer (Virginia Semiconductor) and 1×1 in^2 quartz slides (TED PELLA) were used as substrates. The substrates were cleaned with ethanol in an ultrasonic bath for 5 min and then rinsed with deionized water. Also, before starting each ALD run substrates were allowed to outgas in the reactor at deposition temperature with Ar flowing for 10 min followed by 10 pulses of ozone to remove surface contamination. Samples deposited on Si wafers were used for thickness measurements and X-ray photoelectron spectroscopy (XPS); those on quartz slides were used for optical and conductivity measurements.

Thickness measurements were performed with a J.A. Woolam M-2000D variable angle spectroscopic ellipsometer (VASE) at the University of Maryland NanoCenter. A Cauchy model was used to fit the data obtained from IO films. For ITO samples, an optical model consisting of a Tauc-Lorentz and a Drude oscillator was used, however, considering that the samples were relatively thin the results were close to when a simple Cauchy model was being used. Elemental analysis was done using a Kratos AXIS 165 X-ray photoelectron spectrometer at the University of Maryland Surface Analysis Center. The calibration was done using carbon (284.80 eV), and take-off angles of 20° and 90° (normal to surface) were used. Relative sensitivity factors specific to the Kratos Axis 165 were obtained from the Kratos Vision Software and inputted into CASAXPS, instrumental transmission function was imported with the raw data and read by the CASAXPS software. Reflectance and transmittance were measured using Ultraviolet-Visible (UV-Vis) spectroscopy.

Sheet resistance was measured using a Lucas Signatone S-302 four-point probe and a Keithley 2400-c source meter; film resistivity was calculated using

$$\rho(\Omega \cdot \text{cm}) = 4.53 \times R_{\text{sheet}} \times d \tag{4.1}$$

with d being film thickness [80, 161]. Hall probe measurements (Ecopia HMS-5000) were used to determine mobility and carrier concentrations. Annealing of ITO samples was performed in air in a Barnstead Thermolyne 21100 tube furnace capable of reaching 1200 °C. Scanning electron microscopy (SEM) was performed in the University of Maryland Advanced Imaging and Microscopy (AIM) Laboratory.

Z93 particles were processed in two sets of experiments. To investigate whether the IO film can nucleate and grow on the surface of the pigment particles, 600 ALD cycles were applied to a small batch of particles fixed in position by adhesion to a carbon tape. This experiment was performed using the optimized flow-type ALD recipe, found from the experiments with the flat substrates, consisting of 0.2 s and 0.1 s pulses of TMI and ozone and 30 s Ar gas purge after each precursor pulse. To study the effect of IO coating on the conductivity of the Z93 particles, the sample cylinder and rotatory feed-through were used to coat a 12 g batch of the particles. For this experiment, the sample cylinder was rotated at a rate of about 120 revolution per minute through the application of 1.7 V to the motor. For each precursor pulse, the ALD process recipe cycled through four steps:

1. Close the gate valve and shut off the Ar flow into the chamber.

2. Pulse TMI for 0.2 s (or ozone for 0.1 s).

3. Keep the gate valve closed and the Ar flow shut off for TMI (or ozone) exposure for 5 s.

4. Open the gate valve and restart Ar flow to purge the chamber of excess precursors and by-products.

Upon processing, the pigments were compressed lightly by hand and held in place by a 3D-printed electrically insulating hollow Nylon/Teflon annulus spacer held on an aluminum plate. A stainless steel rod with 1 in diameter and 3 in height was placed on top of the spacer and compressed by approximately 5 lbf. This setup, shown in Figure 4.4, is then biased with voltages varying from 1 to 100 V using a Keithley 6517B electrometer with a built-in source and resistance measurement. Following resistivity measurements in air, the set-up was transferred to a vacuum chamber to investigate the electrical conductivity under different vacuum levels.

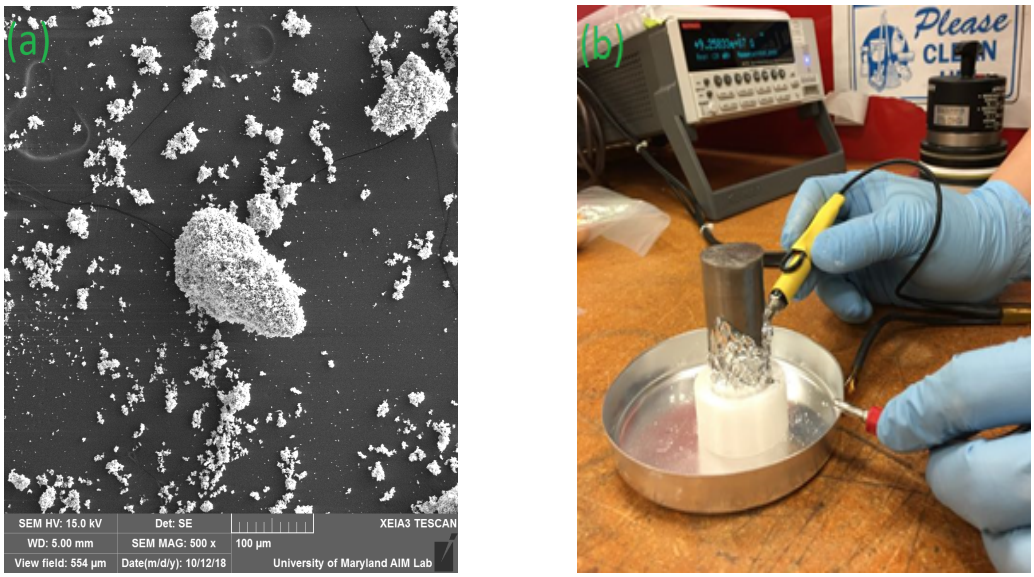

Figure 4.4: The scanning electron microscope image of commercial Z93 heat radiator pigments (a), bulk resistivity measurements of a compressed batch of coated pigments (b).

4.2.2. Reaction mechanism

While there is little information available regarding the reaction mechanisms and kinetics of the TMI/O_3 ALD process, insight can be gained by comparing this system to the ALD of other oxides in the same group as In. Both Al_2O_3 and Ga_2O_3 ALD processes have been studied previously using similar precursor systems (trimethylaluminum and trimethylgallium, respectively with O_3) [33,42,58]. For the first (metal) half-reaction, the most likely mechanism is the chemisorption of the TMI precursor molecule onto surface O atoms of the growing film as is postulated in many other metal-oxide ALD processes [8, 37, 43, 120, 126, 183]. Indium atoms have empty orbitals in their valence shell which can accept a lone electron pair from a surface O forming a Lewis acid/base adduct. The methyl ligands of the adsorbed molecule can later react with protons from surface hydroxyl groups and desorb in the form of methane gas (ligand removal reaction). Methane production during the metal precursor pulse has been observed for both Al_2O_3 and Ga_2O_3 ALD processes when O_3 is used as the O source [33, 58]. Therefore, for the first half-reaction we propose

$$In(CH_3)_{3(g)} + x\text{ -OH} \rightarrow x\text{ -}O_{(b)} + \text{-}In(CH_3)_{3-x} + x\ CH_{4(g)}$$

(g) and (b) subscripts refer to gas phase and the growing film bulk phase, respectively; while all others are surface species. Note that the surface -$In(CH_3)_2$ species may undergo a second ligand removal reaction depending on the availability of hydroxyl sites in its vicinity, resulting in the elimination of a second ligand [183]. The activation energy for release of the third ligand is most likely too large for it to

occur significantly within the temperature range used for this ALD process (<250 °C) [183]. The quartz crystal microbalance study by Mane et al. [107] showed that on average about x = 1.3 of precursor methyl ligands are released during the first half-reaction, which points to an approximate average between the first and the second ligand removal reactions. There are also other possibilities such as dissociative adsorption of the TMI on the surface oxygen bridge sites [43].

During the ozone pulse, it has been suggested that O_3 can decompose to O_2 and O from which the later acts as the oxidizer [42]. The O atom can attack surface methyl groups remaining from the metal precursor dose to generate surface hydroxyls. In Al_2O_3 and Ga_2O_3 ALD processes, this reaction can produce $CH_2O_{(g)}$ [33, 100] or $C_2H_{4(g)}$ [42, 58] by-products. Considering that the ethylene enthalpy of formation is significantly greater than formaldehyde [30], the formation of $CH_2O_{(g)}$ is thermodynamically preferred. The presence of gaseous formaldehyde has been detected by quadrupole mass spectroscopy in Ga_2O_3 ALD process [33]. Locy et al. also have reported formaldehyde production in ozone reaction with TMI [100]. This supports the following potential reaction during the second half-reaction [33]

$$\text{-In}(CH_3)_{3-x} + 2(3\text{-x})\ O_{3(g)} \rightarrow \text{-In}(OH)_{3-x} + (3\text{-x})\ CH_2O_{(g)} + 2(3\text{-x})\ O_{2(g)}$$

A potential overall reaction for this ALD process is then:

$$2\ In(CH_3)_{3(g)} + 6\ O_{3(g)} \rightarrow In_2O_{3(b)} + 3\ CH_2O_{(g)} + 6\ O_{2(g)} + 3\ CH_{4(g)}$$

Note that above overall reaction assumes x = 1.5 (x the number of ligands released during the first half-reaction) which is different than x = 1.3 previously reported for this system [107]. The reported value in the cited source might be partially

due to incomplete surface re-hydroxylation during the ozone pulse, or incomplete saturation of surface reactions during the TMI pulse [171, 183].

4.3. Results and discussion: Flat substrate

To confirm the viability of TMI/O_3 ALD process, and to investigate its application for modification of radiator pigments' electrical properties, IO films were deposited on quartz and Si(100) substrates. Deposition temperatures in the range of 90-190 °C were tested, obtaining gpc of ∼0.46 Å/cycle which proved to be relatively insensitive to temperature using our standard ALD process recipe. gpc as large as ∼0.55 Å/cycle was observed when using two consecutive pulses of TMI before ozone pulse to ensure complete surface saturation. These results agree with values reported by Mane et al. for this ALD process [107]. Figure 4.5 shows the film thickness versus the number of ALD cycles at 140 °C. As it can be seen, film thickness grows in a linear manner with respect to the number of cycles resulting in a gpc of 0.46 Å/cycle. Films deposited with 100 cycles seem to have slightly larger gpc, this might be due to lower density of these thinner films which can result in larger thickness measurements. Other reasons for this might be slightly larger TMI exposure in the beginning cycles (due to longer equilibration in the source), and errors in ellipsometry measurements. Nevertheless, gpc reaches its fixed and reproducible value after about 150 cycles. Based on conductivity measurements presented below, depositing samples with less than 100 ALD cycles seem to result in highly nonuniform films. Also indium oxide film refractive index was found to be ∼2.1 at 632 nm measured by ellipsometry. Figure 4.6 shows the SEM image of the sample

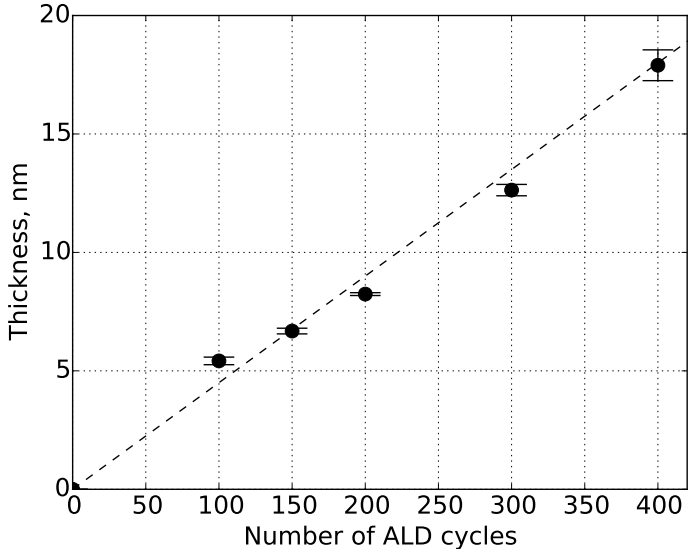

Figure 4.5: Indium oxide film thickness versus the number of ALD cycles for films deposited at 140 °C on a Si substrate. Horizontal bars show standard deviation of thickness measurements from multiple points on the surface.

deposited with 600 ALD cycles on Si substrate at 140 °C. As it can be seen, the film appears to be polycrystalline with the grain size of ∼20 nm. This is consistent with the onset of crystallization of IO films previously reported in the literature at 135-140 °C [41].

4.3.1. Electrical measurements

To investigate the electrical and optical properties of IO films with respect to film thickness and to find the optimum number of ALD cycles for pigment coating, a set of experiments was performed in which IO films of different thicknesses were deposited on quartz and Si substrates. In an ALD process, film thickness can be controlled simply by adjusting the number of ALD cycles. The temperature of these ALD runs was set to 140 °C. As previously mentioned, this value lies in

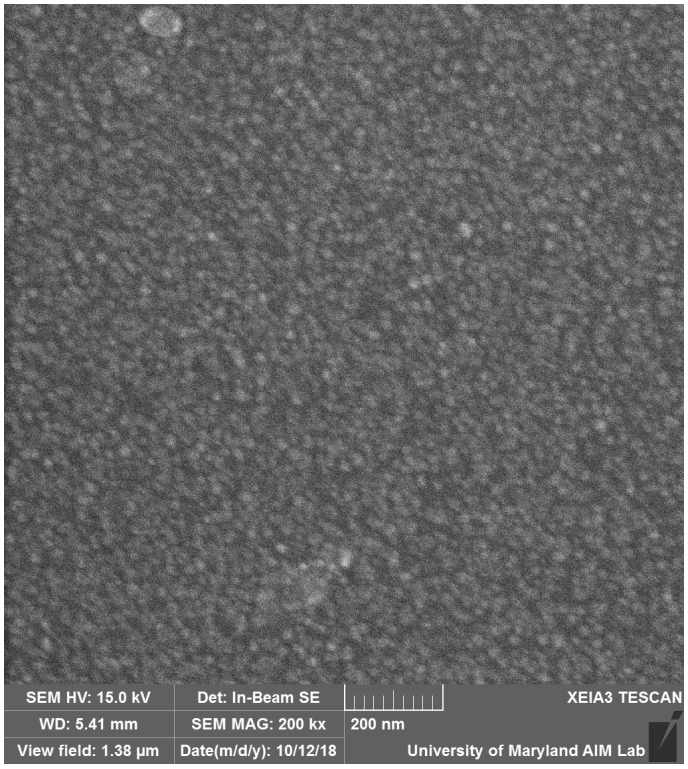

Figure 4.6: SEM image of IO film deposited with 600 ALD cycles on Si substrate at 140 °C.

the ALD temperature window of this process, and the IO films prepared at this temperature have some degree of crystallinity, [59, 107] potentially leading to higher charge carrier mobility, and therefore enhanced conductivity. Figure 4.7 illustrates the resistivity of IO films as a function of thickness as measured by four-point probe. Resistivity is an intrinsic property of a material in bulk form; however, in the case of ultra-thin films, its value may depend on the film thickness. As it can be seen in Figure 4.7, the resistivity plateaus after performing about 200 ALD cycles but for films thinner than ∼8 nm the resistivity depends strongly on film thickness. Overall, three distinct regions can be identified in Figure 4.7. In the first region the film is most likely consist of isolated islands and the conduction

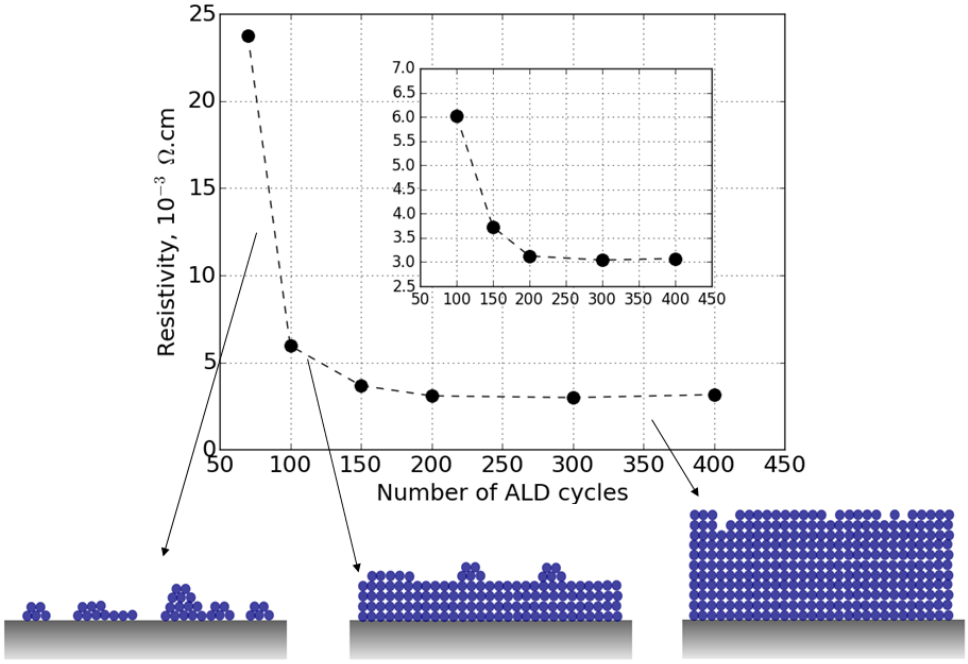

Figure 4.7: Resistivity of IO thin-films versus the number of ALD cycles for films deposited at 140 °C on a quartz substrate as measured by four-point probe. Inset shows a zoom of the low resistivity region.

process is limited mainly by quantum tunneling. Upon performing larger number of ALD cycles a continuous film is being formed, however, significant surface scattering limits the conductivity. Finally, the resistivity plateaus after performing about 200 ALD cycles. This behavior has been previously reported for both IO and ITO films deposited by sputtering and evaporation [89, 112, 123, 149, 166, 167]. Several groups have reported similar values for the critical thickness of IO films (∼7-9 nm) below which film resistivity becomes highly sensitive to its thickness [89, 123, 149, 167]. Using Transmission Electron Microscopy (TEM) studies combined with in-situ electrical measurements, Muranaka and Hayashi concluded that in the initial stages of growth on SiO, IO islands with amorphous structure are formed until reaching

a critical thickness, where they coalesce into a continues layer which then starts to crystallize [123]. Sato et al. and Korobov et al. also reported similar behavior and suggested a Volmer-Weber type growth for IO film deposited on glass [89, 149]. Following Young's equation for interfacial tension, the reported surface energy values of $\sim$1 J/m^2 for IO and 0.3 J/m^2 for glass support this growth mechanism as well [137, 177].

Hall probe measurements were performed to determine the type, concentration, and mobility of the charge carriers in these films. Figure 4.8 shows the results obtained at room temperature. Hall experiments also confirmed the n-type conductivity of as-deposited IO films which has been widely reported in the literature [19, 36, 72, 107]. In the exact stoichiometric ratio, IO films would act as a wide band gap semiconductor, however, the presence of O vacancies and interstitial In sites (the concentration of such defects depends on deposition condition) lead to generation of free charge carriers [36, 71, 169]. In early studies, O vacancies were considered to be the primary reason behind the n-type behavior of IO films. Under this hypothesis, each O vacancy generates two free electrons which can participate in the conduction process [17]. Bellingham et al. performed chemical analysis combined with electrical measurements on amorphous IO films grown by sputtering to establish a relationship between the O/In ratio and charge carrier density. They concluded that based on this view, the O vacancy doping efficiency is only 10% [17]. Investigating the exact origin of the n-type conductivity in IO, Tomita et al. performed first-principles molecular orbital calculations to find the electronic energy levels introduced by different defects in IO [169]. They reported that the energy

level of electrons associated with O vacancies is too deep for them to participate significantly in conduction. Based on their results, those interstitial In atoms which are associated with an O vacancy have the shallowest electron energy level, and so are most likely to act as native donors. These results explain the observed sensitivity of charge carrier density to In/O ratio as well as the calculated low doping efficiency of O vacancies [17].

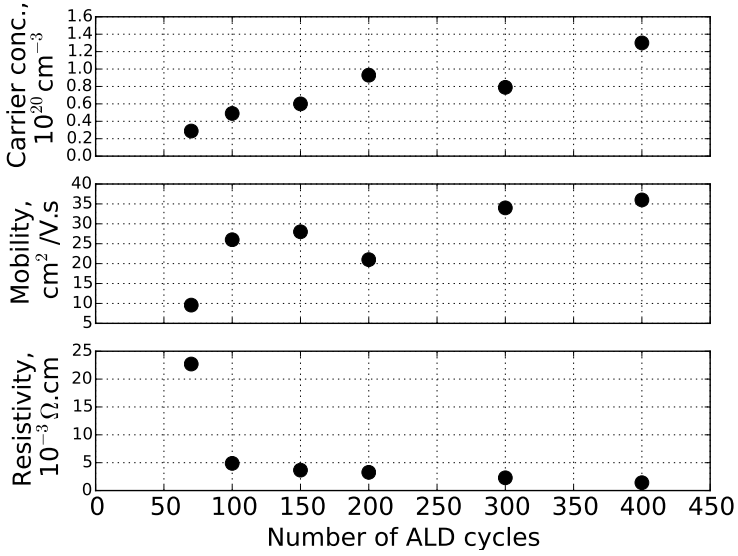

Figure 4.8: Electrical properties of IO films deposited on quartz at 140 °C obtained from Hall effect measurements at room temperature.

As shown in Figure 4.8, measured film resistivity values are very close to those obtained from four-point probe measurements. The small differences might be attributable to errors introduced by the correction factor in the four-point probe calculations, or Hall experiment sample preparation [80,161]. Carrier concentrations for films thicker than 5 nm are in the range of 0.5-1.5×10^{20} cm^{-3} (compare to 1.5×10^{10} cm^{-3} for Si), which is in agreement with previously reported data for IO

films prepared by ALD with the same precursors and by sputtering [17,93,107,167]. Based on our XPS results (presented below), the O/In ratio for these samples is about 1.44. Using this value and the density (ρ) of the ALD prepared IO film of 6.5 g/cm^3, calculated using QCM and spectroscopic ellipsometry data [107], we can approximate the concentration of O vacancies to be $\frac{\rho \cdot N_A}{M_w} \times (3 - 2.88) = 1.7 \times 10^{21}$ cm^{-3}. This is in line with the observation of Bellingham et al. regarding the 10% efficiency of O vacancies with respect to charge carrier generation [17]. Mobility of charge carriers is similar for all samples thicker than 5 nm and ranges from 20 to 35 cm^2/V·s that agrees with literature data [39,107]. The increase in mobility with respect to IO film thickness has been reported before and is mainly due to less surface scattering, and a higher degree of crystallization which results in larger crystal grain size and, therefore, lower boundary scattering in thicker films [27]. Mobility values as high as 72 cm^2/V·s have been reported for 200 nm thick IO films [39]. Also, we would like to point out that the values for film resistivity are somewhat greater when measured immediately after taking the samples out from the reactor chamber. As it will be discussed later, this quasi time-dependent behavior is most likely due to the photoreduction upon exposing samples to the light in the laboratory environment. For all samples the resistivity reaches a fixed value after several hours.

4.3.2. Optical measurements

The optical properties of our IO samples were studied using UV-Vis Spectroscopy. The absorption and transmission spectra for samples deposited by 100, 200 and 400 ALD cycles on quartz are shown in Figure 4.9. All three samples show

some level of absorption for wavelengths less than 500 nm. Samples also showed reflectance values of less than 10% in the infrared region which is of interest for applications related to radiator pigments. The spectra shown in Figure 4.9 are in close agreement with previously reported data [104, 106, 107].

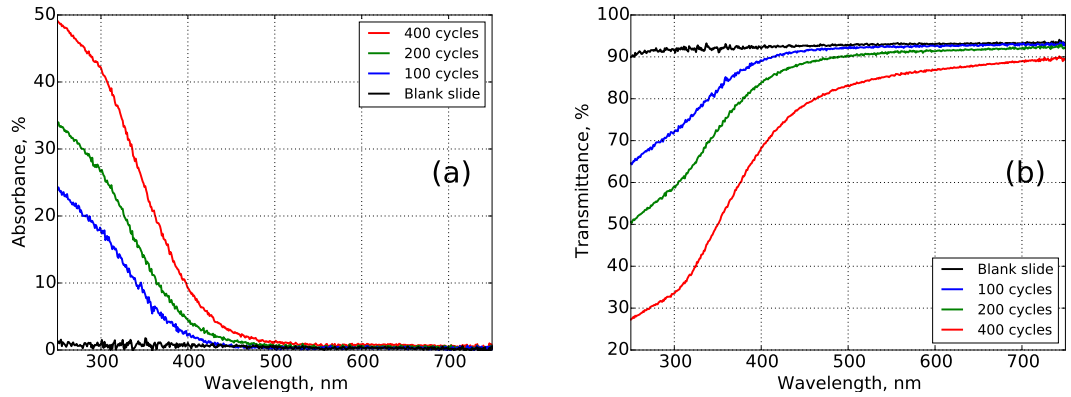

Figure 4.9: Absorbance (a), and transmittance (b) spectra for IO samples deposited by 100, 200 and 400 ALD cycles at 140 °C. The spectrum corresponding to an uncoated (blank) quartz slide is presented for comparison. In all graphs, the top legend corresponds to the top plot and the rest are ordered accordingly.

There appears to be a lack of consensus on the value and nature of the IO band gap reported in the literature. This is mostly due to disagreements in reported band structure and optical absorption data. Indium oxide strongly absorbs light in the ultraviolet (UV) range, and this has been attributed to an IO band gap of 3.5-3.7 eV. However, more recent studies have shown ∼2.7 eV as the minimum band gap for IO [21, 75, 140]. Using UV-Vis data we are able to estimate the optical band gap ($E_{g,opt}$) of our samples. For IO films absorption coefficient α and photon energy $h \cdot \nu$ are related by [168]

$$\alpha h\nu = A(h\nu - E_{g,opt})^n \tag{4.2}$$

where h is Planck's constant, $E_{g,opt}$ optical band gap and A is proportionality con-

stant. The values of $n = 2$ and $n = 1/2$ can be used for indirect and direct allowed transitions and are applicable to IO [107]. According to Tauc's procedure, one can find $E_{g,opt}$ by the line tangent to the linear portion of the $(\alpha h\nu)^{(1/n)}$ versus $h\nu$ plot and its intercept with x-axis [56, 82, 168]. The absorption coefficient α can be approximated using [82]

$$\alpha = \frac{1}{d} \times ln \left[\frac{(1-R)^2}{T} \right] \tag{4.3}$$

with d being the film thickness and R and T, reflectance and transmittance. Figure 4.10 shows the Tauc plot for the same samples as in Figure 4.9.

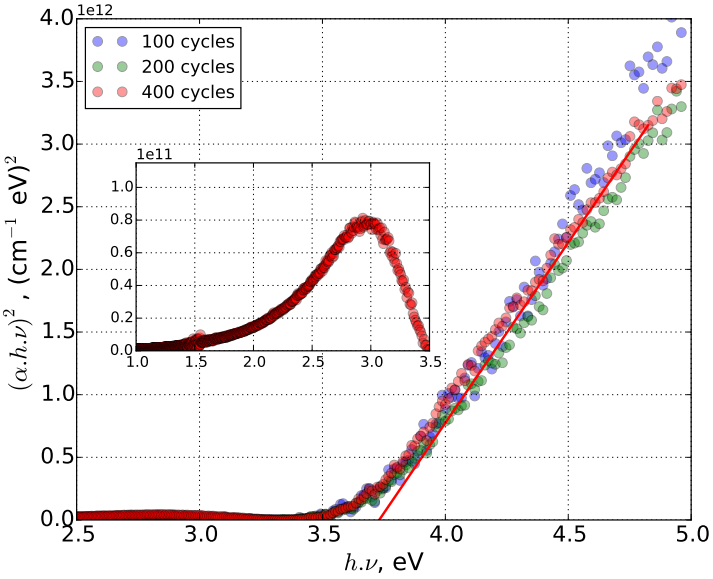

Figure 4.10: Tauc plots for IO samples deposited by 100, 200 and 400 ALD cycles at 140 °C. Optical band gap can be estimated from the x-axis intercept of the linear portion of the curves. Inset shows a zoom of the low energy region.

Tauc plot presented in Figure 4.10 gives an optical band gap value of 3.7 eV for direct transition for the IO sample deposited with 400 cycles which is in close agreement with the value reported in the literature [21]. The $E_{g,opt}$ approximated by

the Tauc's procedure is slightly higher for thinner samples which might be partially due to a 1-D quantum confinement effect [57]. Also note that a small peak can be observed at around 3 eV. Using the value of $n = 2$ in (4.2) and repeating the same procedure for indirect transitions (shown in Figure 4.11) we can estimate the value of 2.7 eV.

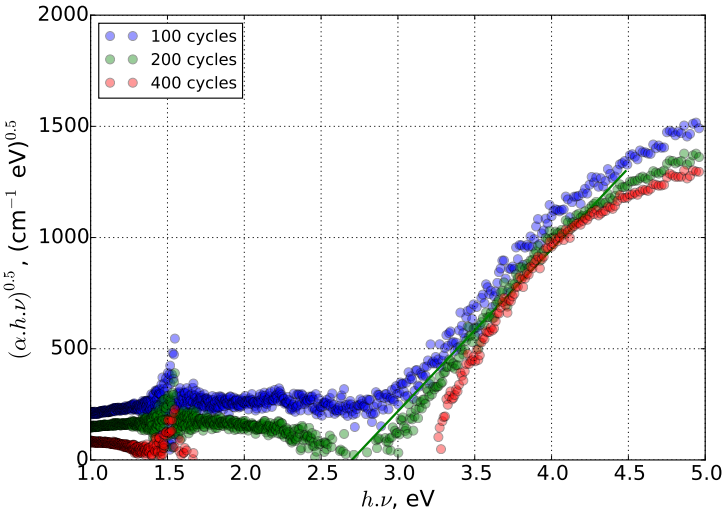

Figure 4.11: Tauc plots for IO samples deposited by 100, 200 and 400 ALD cycles at 140 °C; with the value of $n = 2$ in (4.2) for indirect transitions.

4.3.3. Chemical analysis

XPS measurements were performed to study the chemical composition of IO films. Figure 4.12 shows the XPS spectrum for the IO film deposited by 400 ALD cycles at 140 °C (∼18nm thick). A peak is observed at 529.7 eV which is consistent with O in In-O bond. However, the peak is not symmetric and it can be deconvoluted to two sub-peaks. From the high-resolution scan in O 1s region presented in Figure 4.13, there is a high energy shoulder which can be attributed to the presence of O

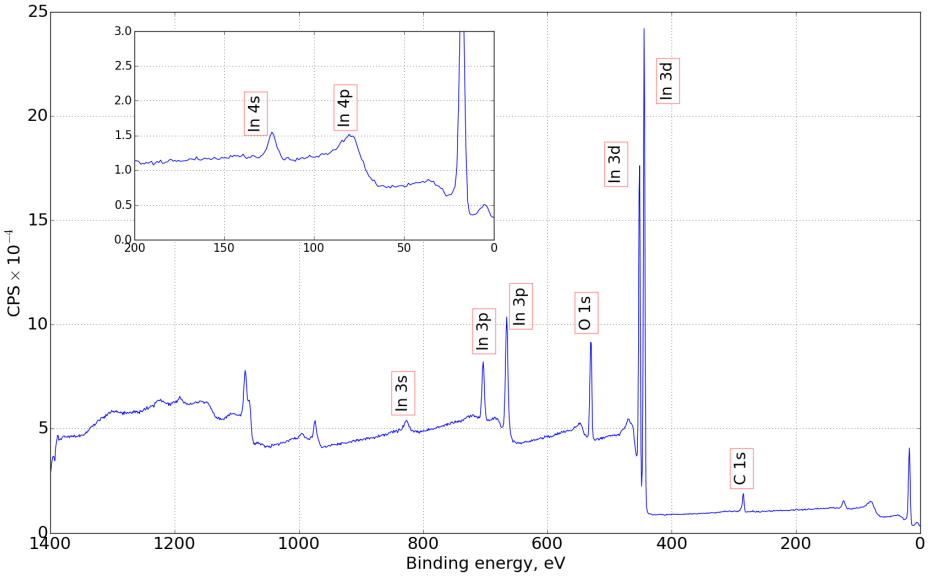

Figure 4.12: XPS spectrum corresponding to a full 0-1400 eV scan for the IO sample deposited by 400 ALD cycles at 140 °C.

vacancies, O-H bond on the surface or in bulk of the film, and also oxidized carbon contamination on the surface. However, the assignment of exact binding energies to these is under debate [6, 16, 70, 107, 157]. If present in the bulk, H atoms can act as donors to IO matrix and generate charge carriers [88]. However, note that the intensities of the two sub-peaks become almost equal when using a 20° take-off angle. Considering that the 20° take-off angle corresponds to higher sampling from regions closer to the film surface, the high energy shoulder can be mainly attributed to O-H bonds due to surface hydroxylation. For this film the O/In ratio was approximately 1.44 which confirms the presence of O vacancies in the film. Two peaks (spin-orbit splitting) are observed at 444.3 and 451.8 eV and correspond to In 3d states, an observation consistent with previously reported results [6, 99, 107, 187]. We also measured the O/In ratio for samples deposited at 190 °C, and obtained

a value of 1.35. This points to potentially higher density of O vacancies in films deposited at higher temperatures, and might be a result of higher saturation for In precursor half-reactions (higher degree of ligand exchange, x>1.5) which leaves a lower number of ligands to be removed in the second half-reaction [143]. Comparing

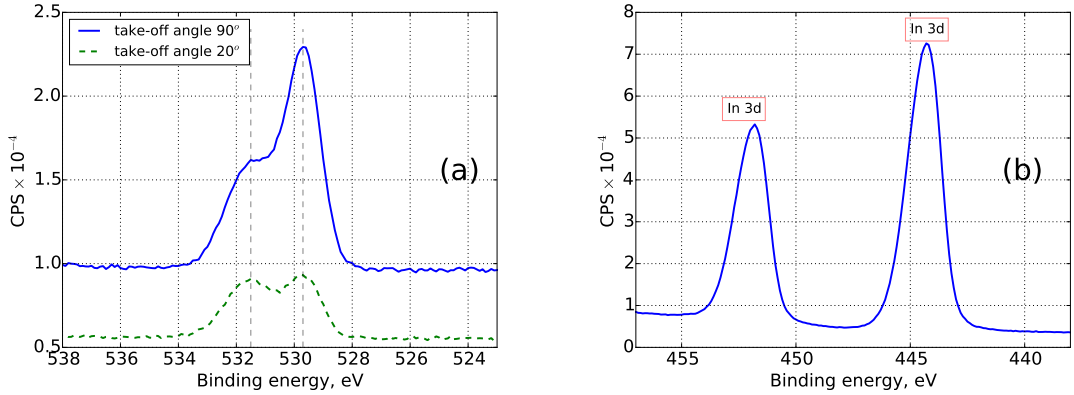

Figure 4.13: High-resolution scans for O 1s (a) and In 3d (b) regions.

the high-resolution scans from the O 1s and In 3d regions for samples deposited at different temperatures shown in Figure 4.14, suggests that the In atoms are oxidized to a slightly higher level in the sample deposited at lower temperature (resulting in a small peak shift to higher binding energies). This observation is consistent with higher O/In ratio calculated for these samples. Note that that surface layer can highly affect this ratio. In any case, when interpreting the XPS results, note that the errors due to the accuracy of the Scofield cross-sections calculated by Hartree−Fock methods and possible imperfect background removals may have affected the accuracy of the calculated O/In ratio. Also, as mentioned above, the uncertainty in assigning the high energy shoulder in the O 1s peak to O-H bond, O vacancy, or oxidized carbon can introduce additional errors to O/In ratio. Samples deposited at 190 °C

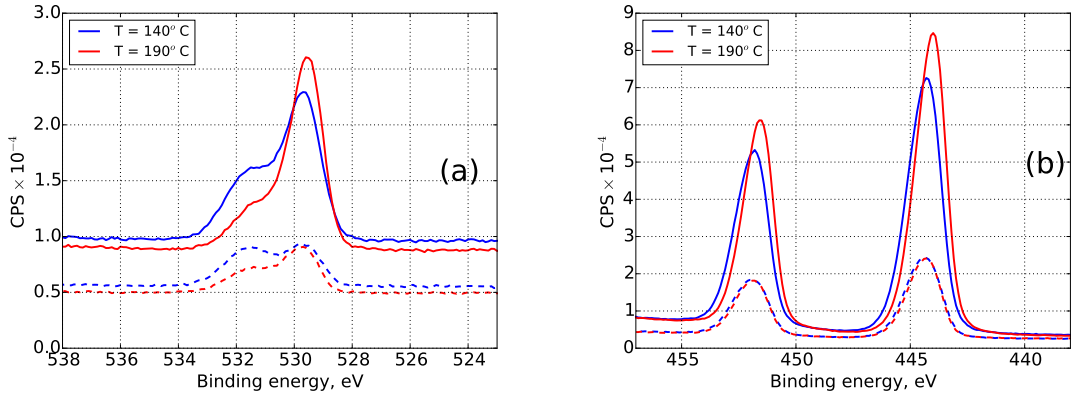

Figure 4.14: High-resolution scans for O 1s (a) and In 3d (b) regions for samples deposited at 140 °C (blue) and 190 °C (red). Dotted lines correspond to 20° take-off angle.

showed about 15% carbon content which by comparing the high and low take-off angles, and considering the fact that experiments were not performed in a cleanroom environment, is believed to mostly be due to surface contamination. Those deposited at 140 °C showed slightly but consistently larger carbon incorporation in the film (about 20-25%) which can be attributed to the incomplete removal of TMI precursor ligands. This might be contributing to relatively weaker shoulder of O 1s peak for high temperature sample in Figure 4.14.

4.3.4. Variability in film resistivity

As discussed above, the conductivity of IO films results from interstitial In sites and O vacancy defects; the concentration of each may depend on the manufacturing process conditions or the gas composition in contact with the IO film. These factors may explain the significant variability found in reported resistivity data [17, 130]. It has been reported that IO film resistivity may increase by four orders of magnitude in the presence of O_3 as an oxidizing agent [18, 87, 130, 178, 185]. This change in

resistivity is, however, reversible if the film is exposed to light with photon energy greater than 2.8 eV [179]. The sensitivity of IO films to environmental factors has made them interesting candidates for gas sensing applications [85, 97, 146, 179]. Note that a reducing agent such as ethanol can also act instead of a light source to decrease film resistivity which enables the potential application of IO thin-films as a sensor for both oxidizing and reducing gases.

To assess IO film sensitivity to its environment, we performed a set of experiments to investigate the potential application of ALD-prepared IO films for gas sensing. These experiments consisted of exposing the samples to different sets of O_3 pulses using our ALD reactor at room temperature, and then transferring them to an ambient environment and exposing the films to a UV-containing light source to measure the changes in their resistivity. The ozone pulses consisted of the same O_3/O_2 ratio as that of the ALD runs and generated a peak partial pressure of $\sim$1 Torr inside the reactor chamber. Among the samples, the thinner ones showed higher sensitivity to ozone exposure as might be expected [18]. Figure 4.15 shows the results for samples deposited with 100 and 150 ALD cycles. In both cases, the resistivity significantly increases in the presence of ozone at a low partial pressure. In turn, exposing the samples to a light source rapidly causes a decrease in their resistivity.

It has been suggested that during ozone exposure, adsorption of O atoms on the surface produces a depletion layer by consuming free electrons resulting in increased resistivity. However, layers below the surface still can act as parallel elements with greater conductivity. This is one of the reasons behind differing dynamics of

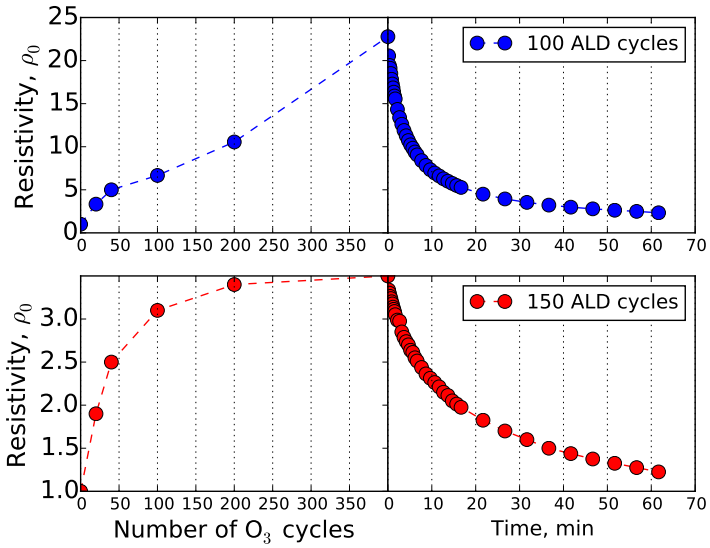

Figure 4.15: Sensitivity of ALD-prepared IO films' resistivity to exposure to ozone and a light source. y-axis is normalized with respect to the reference resistivity before starting the test. Ozone pulses generated a ∼1 Torr partial pressure peak inside the reactor chamber at room temperature; resistivity measurements were performed immediately after removal from the reactor. The light source used was a 45 W 3000 K tungsten bulb.

resistivity changes for films of different thicknesses [18, 178]. The resistivity value reaches its maximum if sufficient time is given for O to diffuse through the entire film. This mechanism is in agreement with the data shown in Figure 4.15, and that thinner samples show higher sensitivity to ozone exposure. Upon radiation, light-generated electron and hole pairs are produced; electrons can contribute to conduction, and holes can react with surface O^- ions to produce O atoms which combine to form oxygen gas [178]. We conclude that the sample deposited by 100 ALD cycles can provide the best response for ozone sensing; thinner films are likely to be discontinuous. Furthermore, the fact that the film resistivity significantly increases upon exposure to ozone, in addition to the measured charge carrier mobility

(much less than ~100 $cm^2/V{\cdot}s$ observed for H doped IO [88]) confirms that the high energy shoulder in XPS spectrum is mostly due to O vacancies, surface O-H bonds or oxidized carbon and that our samples are not significantly doped with hydrogen.

4.3.5. Indium tin oxide

High sensitivity of IO film conductivity to environmental factors hinders its direct use in many applications where a consistent level of conductivity is required. For these applications IO is typically doped with less than 10 wt.% Sn to make ITO. Sn has an additional valence electron relative to In and so Sn may act as an electron donor if ionized. Sn can be easily introduced into the IO matrix by defining a supercycle in the ALD recipe which consists of pulses of TDMASn + O_3 between a set of normal IO pulses. The relative ratio of the two determines the final doping level. Following this procedure, a set of ITO samples with 0, 3.3, 5, 6.6, 12.5 % SnO_2 pulses (supercycle recipe of 0, 10, 15, 20, 37 SnO_2 pulses in total of 300 ALD cycles, respectively) were prepared. For all samples the total number of ALD cycles was fixed at 300. Furthermore, to provide a uniform doping throughout the film, each SnO_2 cycle was introduced separately from others, meaning each individual SnO_2 cycle was proceeded and followed by a sequence of IO cycles. These samples were deposited at 100 °C. This deposition temperature enables us to study the ITO samples in both amorphous (as-deposited) and crystalline states (upon annealing); however, it potentially leads to slightly higher carbon impurity in the film. Figure 4.16 shows the resistivity of ITO samples measured by four-point probe in as-deposited form and after annealing in air (at 220°C for 4 hours and then at

450 °C for 4 hours).

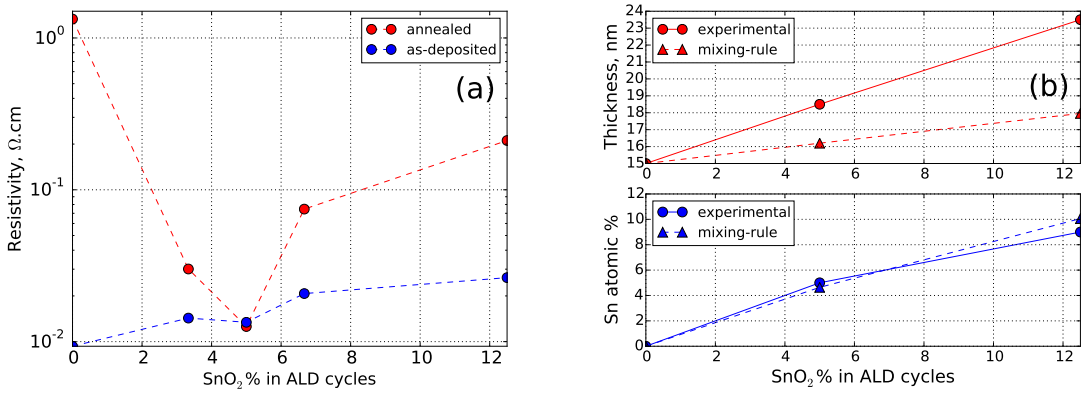

Figure 4.16: Resistivity of deposited ITO thin-films as a function of SnO_2 cycle percentage for a total of 300 ALD cycles (a). Experimentally determined and mixing-rule predicted thicknesses and Sn atomic percentages for ITO films deposited with 0, 5 and 12.5% SnO_2 for a total of 300 ALD cycles (b).

As can be seen in Figure 4.16, for as-deposited ITO films, there is no improvement in film conductivity with increasing Sn fraction. In fact, samples doped with Sn show a slight increase in resistivity. This can be explained by the structure of the deposited films at low temperatures: IO reportedly starts to crystallize at 135-140 °C [41, 107] and Sn is known to remain neutral and inactive in amorphous ITO [119, 159]. Sn atoms also can act as neutral scattering centers resulting in higher resistivity. Furthermore, films with higher Sn content had slightly higher thicknesses (gpc ∼0.75 Å/cycle for highest doped sample) which results in higher resistivity according to equation 4.1.

Upon annealing in air, the resistivity curve confirms the presence of a clear global minimum corresponding to the sample doped with 5% SnO_2 cycles. Annealed in air at high temperature for extended time, the pure IO sample has become much more resistive as a result of high O diffusion and annihilation of O vacancies [167].

It also is suggested that doping IO samples with high amounts of Sn results in formation of neutral Sn_2O_4 clusters which can act as scattering centers [39]. For the undoped and highest doped samples the mobility of charge carriers appear to significantly decrease upon annealing in air, reaching values as low as 6 $cm^2/V{\cdot}s$. As a final note, while the value of film resistivity for the 5% SnO_2 cycle sample is almost the same before and after annealing, the origin of charge carriers (O vacancies versus ionized Sn) and their stability against oxidizing gases such as ozone is different. A comparison of stability against ozone for an IO and an optimally-doped ITO sample with the similar thickness is shown in Figure 4.17. These samples were prepared at 140 °C with a total of 400 ALD cycles. For a clear comparison, unlike the results of Figure 4.15, this test was performed at a higher temperature (140 °C) to enhance the O diffusion into the film.

XPS analysis was performed on two of the ITO samples to confirm the presence of the Sn dopant, and to establish the relationship between the percentage of SnO_2 cycles in the process recipe and the level of Sn doping in the film. Figure 4.18 highlights the new peaks associated with Sn atom in the XPS spectra. Table 4.2 summarizes the results for Sn content obtained by studying Sn 3d peaks in the XPS spectra. Note that the precision is very high in XPS using relative sensitivity factors meaning changes in Sn content between samples can be detected within a few tenths of a percent in atomic concentration. Calculated Sn wt.% show that the sample prepared by 5% SnO_2 cycles contains 10 wt.% Sn which is the optimum doping level of Sn widely reported in the literature [112, 115, 128]. This is consistent with the minimum point obtained in Figure 4.16. Investigating the potential migration of

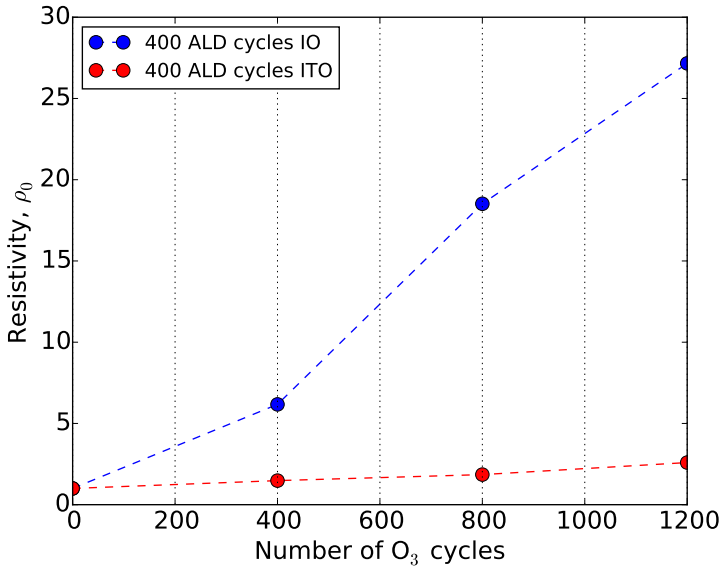

Figure 4.17: Sensitivity of IO (top) and optimally-doped ITO samples resistivity to exposure to ozone; y-axis is normalized with respect to the reference resistivity before starting the test. Ozone pulses corresponded to ∼1 Torr partial pressure peak inside the reactor chamber at 140 °C; resistivity measurements were performed immediately after removal from the reactor.

Sn atoms to the surface, we also analyzed XPS spectrum obtained from a take-off angle of 20^o; this gave a similar Sn content, confirming almost uniform Sn doping throughout the film. Furthermore, data presented in Table 4.2 suggest that the efficiency of doping with our ALD process may decreases with increasing SnO_2 cycles.

Table 4.2: Sn content obtained by XPS analysis for ITO films deposited with 0, 5 and 12.5% SnO_2 cycles in a total of 300 ALD cycles at 100 °C. The values for wt.% are calculated using O, In, and Sn molar masses.

SnO_2 cycle %	Sn atomic%	Sn wt.%
0	0	0
5	5	10
12.5	9	19

As mentioned above, films deposited with higher percentages of SnO_2 cycles

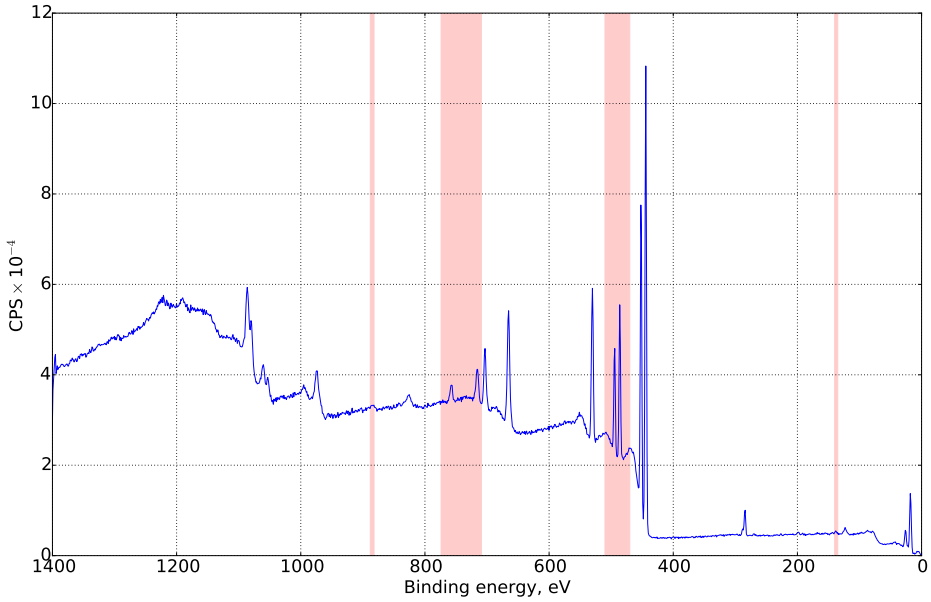

Figure 4.18: XPS spectrum corresponding to a full 0-1400 eV scan for the ITO sample deposited at 100 °C. Highlighted areas show the new peaks associated with Sn atom, and from right to left correspond to 4s, 3d, 3p and 3s states.

showed higher gpc values (shown in Figure 4.16). This can be partially attributed to the intrinsically higher growth rate of ALD-prepared SnO_2; the gpc for SnO_2 ALD using the TDMASn/O_3 precursor system at T=100 °C is ∼1.3 Å/cycle as reported by Choi et al. [32]. However, as it can be seen in Figure 4.16, the experimentally measured thickness is larger than the value predicted by a simple weighted average between thicknesses from individual ALD processes. Furthermore, to predict the correct Sn atomic%, we define a mixing rule that relates the thickness increment of each ALD cycle to the number of atoms deposited on the growing film surface in each cycle by [132]

$$\Delta_{Metal} = \frac{\Delta_h \times \rho \times N_A}{M_w} \tag{4.4}$$

with Δ_{Metal} being number of metal atoms deposited during each cycle, Δ_h thickness increase (gpc), and ρ and M_w density and molar mass of the material. Defining a mixing rule for predicting Sn atomic% we have

$$\text{Sn atomic\%} = 100 \times \frac{N_{Sn} \times \Delta_{Sn}}{(3 \times N_{Sn} \times \Delta_{Sn}) + (2.5 \times N_{IO} \times \Delta_{In})} \tag{4.5}$$

N_i terms refer to the number of ALD cycles associated with In_2O_3 and SnO_2. As it can be seen in Figure 4.16, the predicted values for Sn atomic% in the film are in good agreement with the experimental values measured by XPS. One possible explanation for higher gpc for doped samples is that the SnO_2 pulse sequence may provide a better surface hydroxylation, facilitating the growth in potentially few subsequent In_2O_3 cycles. This hypothesis can be tested by performing QCM studies comparing the difference in mass increase for normal In_2O_3 cycles compared to those which immediately follow a SnO_2 cycle. Slightly lower density of SnO_2 also may have contributed to higher thickness readings for ITO samples.

4.4. Results and discussion: Particles

Figure 4.19 shows the scanning electron microscope images of an Si substrate and Z93 pigments coated in the first set of experiments described with 600 ALD cycles of exposure to TMI and ozone in a regular flow-type ALD process. As it can be seen, IO film is able to nucleate and grow on the surface of Z93 particles confirming the possibility of the encapsulation with a thin-layer of IO. Furthermore, the structure of the IO coating is similar to that of the IO film deposited on a standard silicon substrate during the same experiment resulting in a ~30 nm thick

film. The film appears to be polycrystalline with the grain size of ∼20 nm; this agrees with the crystallization of IO films reported in the literature at 135-140 °C [41].

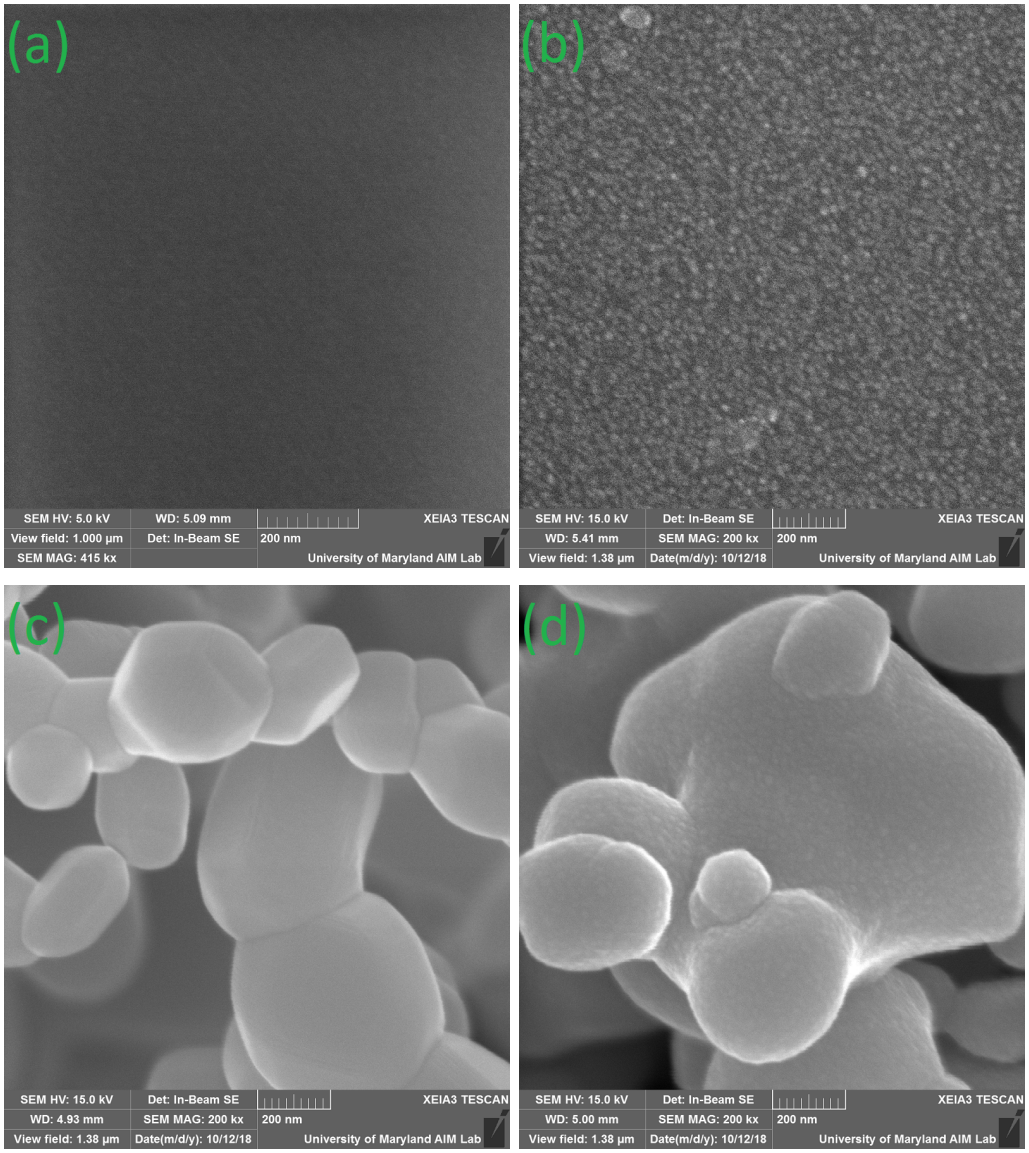

Figure 4.19: SEM images showing the IO thin-films deposited with 600 ALD cycles at 140 °C in a regular flow-type ALD process. Clean uncoated Si wafer (a), IO film deposited on the Si wafer (b), original uncoated Z93 particles (c), coated Z93 particles (d).

Energy Dispersive X-ray Spectroscopy (EDS) analysis also was performed to confirm the presence of indium atoms in the coated sample fixed on the carbon tape.

Figure 4.20 clearly shows the presence of indium. Note that the Zn signal originates from the pigment itself, and O signal results from both the IO coating and the Z93 pigments.

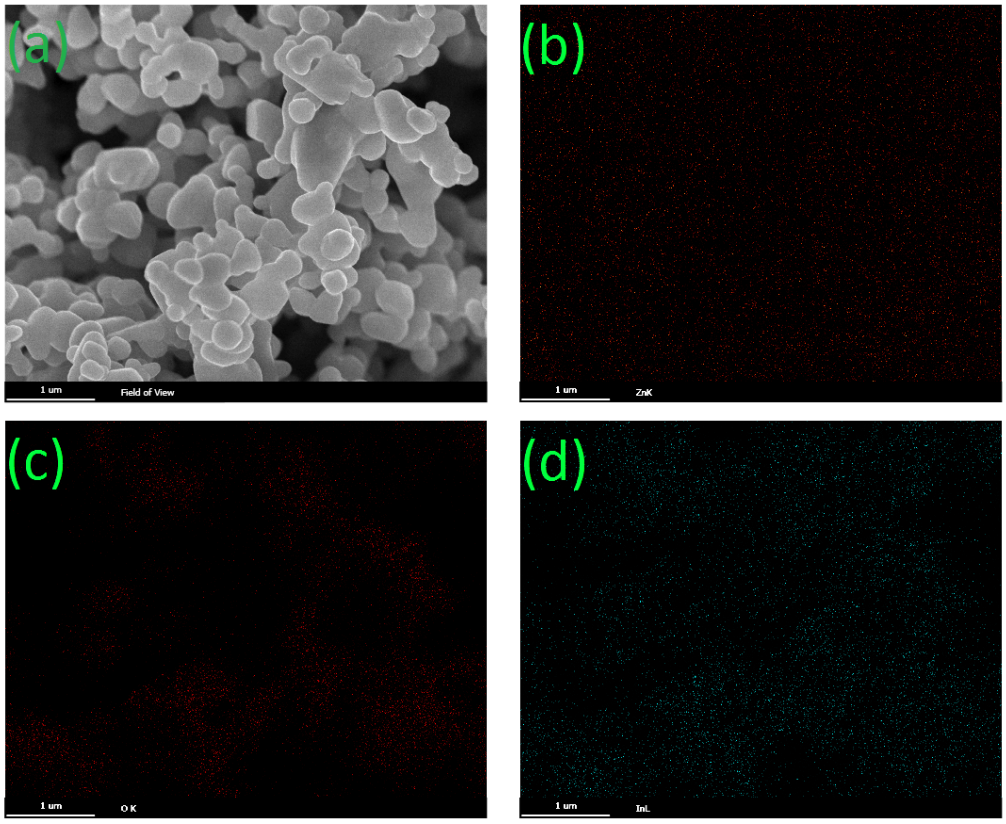

Figure 4.20: EDS scan of coated Z93 particles deposited with 600 ALD cycles at 140 °C in a regular flow-type ALD process. Image of the mapping area (a), Scan for Zn (b), O (c), and In (d). The black background is the carbon tape used for fixing the particles.

As mentioned, the primary function of Z93 or other materials used for thermal control coatings is to efficiently dissipate waste heat. These coatings are required to have high emissivity and low solar absorptivity. Therefore, it is desirable to apply the minimum level of coating on their surface to maintain their original optical properties [78]. In our experiments with flat substrates, we concluded that using our precursor system, 100 ALD cycles is sufficient to produce a continues uniform IO thin-film

with conductivity that satisfies the criteria required to avoid charge buildup and the subsequent ESD [145] while retaining on average ∼90% transparency in visible range. Table 4.3 compares the bulk resistance in ambient pressure of the original uncoated Z93 pigment particles and a sample coated with 100 ALD cycles. Furthermore, to ensure that the observed conductivity is not due to potential adsorption of water molecules in the processed batch, and to check for potential degradation of electrical properties in various environments, the measurements were repeated by keeping the samples under different vacuum levels. The effect of the indium oxide coating can be clearly seen as the resistivity has been decreased almost with a factor of 4. As the vacuum level is increased, the difference between the resistivity of indium oxide coated and original pigments becomes more significant. This can be partially attributed to either the removal of the moisture within the bulk powder or the compression of the powder filling the void space allowing for a clearer conduction path.

Table 4.3: Bulk resistance of uncoated Z93 pigments and the sample coated with 100 ALD cycles under different vacuum levels. Both samples contain the same amount of Z93 pigments.

Pressure (Torr)	Sample	Applied voltage	R(Ohms)
$7.60\times10^{+2}$	coated Z93	40	$1.30\times10^{+8}$
	original Z93	40	$5.10\times10^{+8}$
$7.00\times10^{+1}$	coated Z93	40	$1.60\times10^{+8}$
	original Z93	40	$8.00\times10^{+10}$
7.00×10^{-2}	coated Z93	40	$1.80\times10^{+8}$
	original Z93	40	$1.80\times10^{+11}$
6.00×10^{-2}	coated Z93	100	$7.00\times10^{+7}$
	original Z93	100	$6.00\times10^{+10}$

Figure 4.21 shows the reflectance of the original and processed Z93 sample

coated with 100 ALD cycles of indium oxide. As it can be seen, the processed pigments have retained their original reflectance as well, which is assuring considering the fact that for this application retaining optical properties close to that of the original Z93 particles is highly desired.

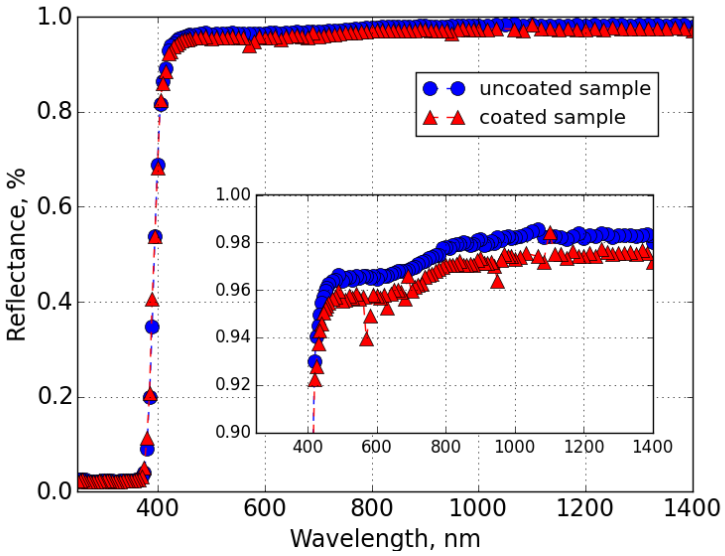

Figure 4.21: The reflectance spectrum of the original and processed Z93 sample coated with 100 ALD cycles of indium oxide.

The emissivity of the Z93 particles were also tested before and after coating experiments. The emissivity of the original Z93 particles is ∼0.92 and the coated samples maintained roughly the same value. Besides the IO coatings itself, the carbon impurities present in the layer might result in a decrease in emissivity and other degradation of optical properties. As mentioned above, comparing samples performed in different temperatures suggests that increasing the deposition temperature leads to lower amount of carbon impurity in the coating which is desirable; however, based on our observations, the Z93 particles tend to agglomerate more at

higher temperatures which might negatively affect the coating uniformity. Nevertheless, the reactor design can be improved to provide better exposure and more uniform coating for the particles.

4.5. Final remarks

In this chapter we have studied the ALD process of indium oxide and indium tin oxide thin films using trimethylindium, tetrakis(dimethylamino)tin(IV), and ozone as precursors. The relationship between the thickness of indium oxide films and their electrical and optical properties has been established with the goal of finding the optimum thickness for coating the Z93 pigment particles used in spacecraft heat radiators to ultimately increase their electrical conductivity without significantly affecting their optical properties mainly emissivity. The process with 100 ALD cycles was shown to provide a uniform film with resistivity as low as $5\times10^{-3}\ \Omega\cdot\text{cm}$ and $\sim$90% transparency in the visible range. X-ray photoelectron spectroscopy was used to investigate the relationship between the ternary In-Sn-O ALD process recipe and the level of doping in the final product. The process containing 5% SnO_2 cycles was shown to provide the optimum level of Sn doping in the ITO film for highest conductivity. Furthermore a custom-built ALD reactor was designed and constructed for processing the Z93 pigment particles and to assess whether the proposed ALD chemistry can be used to coat these particles and the film is able to nucleate and grow on their surface.

Prepared samples coated with indium oxide and indium tin oxide layers were launched to international space station as a part of the Materials International Space

Station Experiment (MISSE) mission to further investigate their performance under low earth orbit condition. Potential factors that might affect the performance of the coatings in orbit might be active atomic oxygen and high exposure to UV light. Based on our experiments, the presence of oxygen might lead to significantly higher resistivity in the coating; however, on the other hand, UV light can contribute to electron-hole pair generation and so better conductivity.

Chapter 5: Conclusions and Future Works

5.1. Conclusion

Chapters 2 and 3 of this dissertation focused on the reaction network analysis for ALD processes with the ultimate goal of defining a step by step procedure for development of representative ALD surface reaction kinetic models. Emerging computational tools such as density functional theory have the ability to provide accurate information on the thermodynamics and kinetics of surface reaction. However, in order to relate such data to macroscopic and experimentally measurable quantities kinetic models based on a well-posed system of equations describing the evolution of different species in the system are required. At the core of this modeling approach lies a reaction network consisting of initial precursor adsorption and subsequent surface reactions which occur during each ALD half-cycle. In the beginning of this dissertation we defined the criteria for a proper ALD RN. A proper ALD RN has the potential to mimic the ALD behavior and can guarantee the self-limiting and surface reproducibility properties inherent to practical ALD processes. Since these two both originate from properties of the growth surface, and considering that in an ALD process the growth surface tracks a cyclic trajectory during each ALD cycle

and returns to its original state, we concluded that there should be surface-related invariant states in the RN that can help to answer whether a proposed RN can satisfy the set criteria. In order to study these surface-originated invariant states we have focused on defining only semi-positive invariant states. We have shown that for a physically valid RN, for any chemical system, the invariant subspace must be describable by such a basis set, otherwise there are stoichiometric inconsistencies in the network. Clearly, formulated using only positive coefficients, these states are the most amenable to physical interpretation and are desired for our ALD RN analysis purpose. Two methods based on the species-reaction graph associated with the RN, and the principles of convex analysis were developed and their applicability for RN analysis was shown in the context of four different chemical processes including ALD. In chapter 3 both of these methods were extended to study not just RN invariant states but also variant states. Therefore, completely defining a mathematical transformation from the original molar quantities to a new state space where the dynamic order of the system is reduced through the identification of RN invariants, and if possible, each of the newly defined variant states are dynamically associated with only one of the reactions in the network. This facilitates the study and ultimately the formulation of different reaction rates in the system.

In chapter 4 an experimental study was conducted for the ALD process of indium oxide and indium tin oxide thin-films. The goal in this work was to develop an ALD process to coat the commercial pigment particles used in manufacturing spacecraft heat radiator panels in order to enhance their electrical properties to avoid electrostatic charge built-up during the spacecraft passage through Van Allen

radiation belts. To find the optimum process, different sets of experiments where conducted on standard flat substrates and commercial Z93 radiator pigments to:

1. Establish the relationship between the thickness of the deposited IO film and its electrical and optical properties.

2. Assess the ability of the proposed ALD chemistry based on trimethylindium, tetrakis(dimethylamino)tin(IV), and ozone precursor system to deposit ITO thin films; and to establish the relationship between the ALD process recipe and the doping level in the final product.

3. Assess the ability of the developed ALD process to coat the surface of the Z93 pigment particles and test whether the IO film is capable to nucleate and grow on their surface.

4. Test whether the proposed process based on ALD of IO and ITO coatings is useful to enhance the properties of the Z93 pigments.

5.2. Future works

5.2.1. Reaction network analysis

The developed approach based on species-reaction graphs and convex analysis in this work provides a framework for formulation of physically-relevant invariant and variant states and using them to analyze ALD reaction networks. However, these can be extended to encompass additional information as well. One obvious addition is to incorporate the available thermodynamic data for different ALD precursors and reaction products in the software package that performs the operation.

This way free energies associated with each reaction can be computed and presented alongside with the graph. This provides additional criteria that can be used to modify a proposed reaction network if some of the suggested reactions are not likely to proceed under a specific condition. Ideally, this package then can be coupled with a complete database of ALD precursors thermophysical properties as an online source available to the research community.

5.2.2. ALD for heat radiator coatings

Performed tests in this study confirmed the possibility of coating the heat radiator particles with IO and ITO thin-films using the proposed ALD process and chemistry. However, modified reactor designs and further characterization of particles such as transmission electron microscopy can be used to achieve and confirm the complete encapsulation of the particles with the thin-film coating. Furthermore, while pre-processing the Z93 heat radiator pigment particles by ALD provides a new solution for charge bleeding and avoiding the ESD on the spacecraft during its mission, processed particles might undergo structural and chemical changes when exposed to harsh condition of space. It is necessary to evaluate different properties of the particles after being exposed to these conditions.

5.2.3. ALD for X-ray optics

Another space application which can greatly benefit from advantages of the ALD process is space optics. In particular X-ray optics used for imaging space weather in the high frequency X-ray wavelengths can be optimized using ALD of specific metallic films. Ni metal is one of the materials that is typically used in

the structure of X-ray optics and X-ray telescopes because of its X-ray reflectivity (XRR) properties [162]. Therefore, investigating different mechanisms for depositing Ni films with ALD is potentially useful for advancements in this area. Furthermore, ALD is capable of providing uniform coating in high-aspect ratio structures which opens up potentials for a new generation of X-ray optics. Other applications of Ni in its metallic or oxide forms that can benefit from ALD are in catalysis, optoelectronics and sensors [28, 61, 124, 147].

In general depositing pure metallic Ni thin-films are more challenging compared to metal-oxide films mainly because:

1. Large differences in surface energies of the metallic film and the substrate compared to, for example, a metal-oxide film that potentially results in longer nucleation period and large grains.

2. Lack of high vapor pressure ALD precursors which complicates the precursor delivery system.

3. Typical Ni precursor unwillingness to reduction to its metallic state that results in requiring high temperatures or activated radical species as the reducer precursor for the reduction reaction to proceed.

There are multiple pathways that can be taken for depositing Ni films. Due to the possibility of reducing NiO to Ni in relatively low temperatures [28, 172], one approach is to produce an oxide layer first and then use an ex-situ reduction step. Major challenges in this approach are requiring high temperatures for reduction

by a noble gas such as argon [14], and formation of pinholes or complete transformation of the film to isolated clusters for reduction using hydrogen [172, 173]. An alternative approach is direct deposition of the metallic film. The main issues associated with this approach are requiring high temperatures or activated species such as hydrogen radicals as the reducer agent [28]. Figure 5.1 shows different pathways available for depositing Ni film and challenges associated with each. As

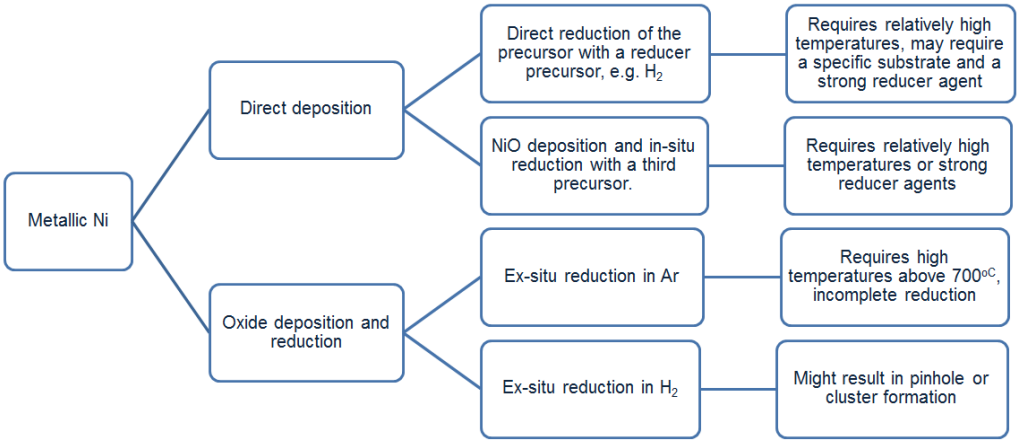

Figure 5.1: Different pathways available for depositing Ni film and challenges associated with each [28, 172].

it can be seen, the simplest method is to deposit a NiO thin-film layer first and subsequently reduce it to Ni. Depositing nickel oxide, a good candidate precursor system is bis(cyclopentadienyl)nickel(II), or nickelocene, $Ni(Cp)_2$ and O_3. Other widely used Ni precursor in ALD and CVD processes is nickel(II)acetylacetonate, $Ni(acac)_2$. While almost 1.5 times more expensive than $Ni(acac)_2$, the main advantage of nickelocene is its much higher vapor pressure which facilitates the direct draw precursor delivery. Furthermore, it is reported that $Ni(acac)_2$ has a high tendency to agglomerate in gas phase to form trimers. This in addition to its low vapor

pressure can significantly complicate the design of the precursor delivery system. Figure 5.2 compares the vapor pressure of the two Ni precursors. As the oxygen source, ozone is previously shown to be able to react with metallocene precursors and remove the cyclopentadienyl group at relatively low temperatures [40]. Initial result for this ALD system for producing high-quality X-ray reflector coatings are provided in appendix E.

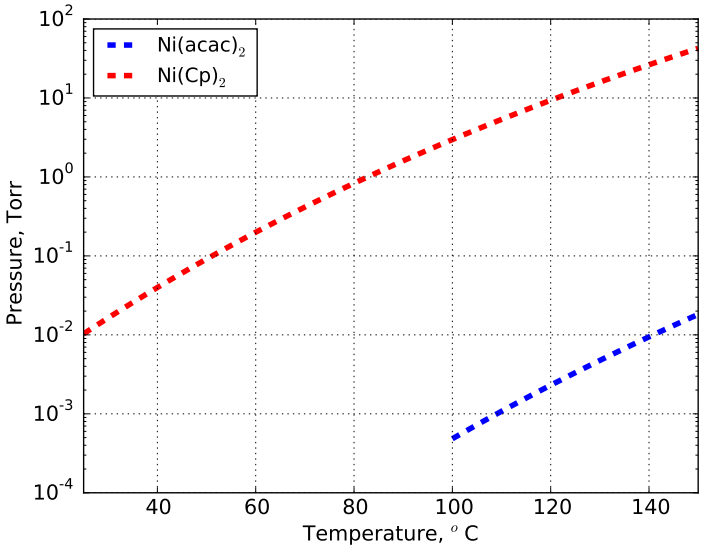

Figure 5.2: Vapor pressure of the two Ni precursors $Ni(acac)_2$ and $Ni(Cp)_2$ reported by [116, 175].

Appendix A: The equivalency of the two criteria for constructing a systematically independent set

To show that both approaches to remove the redundant vectors from the generating set from the result of the convex algorithm presented in chapters 2 and 3 are mathematically equivalent, we start with the first algorithm described in chapter chapter 2. According to the statement in the second step, for a pair of rows (i, k) in the m^{th} tableau that have elements with different signs in the corresponding column a new vector can be constructed only if for every row $l \neq i, k$ in the current tableau $S(i) \cap S(k) \nsubseteq S(l)$ where $S(i) = \{h - n_r : h > n_r \text{ for which } t^j_{i,h} = 0\}$ contains column indices of zero elements of each row in the right-hand side of the current tableau. Let us pick a pair of rows (i, k) such that they have opposite sign elements in the column of interest (meeting the first criterion of the step 2), however, there is a row l that $S(i) \cap S(k) \subseteq S(l)$. Note that the algorithm in chapter 2 votes to not using this pair. Nevertheless, we use this pair and proceed to construct a new vector $\nu_{i,k}$ for the next tableau $m + 1^{th}$. Two cases might occur when constructing the new tableau:

1. Row l in the m^{th} tableau already has a zero element in the $m^{th} + 1$ column so it is readily picked to be used for constructing tableau $m + 1^{th}$. In this case in

the $m+1^{th}$ tableau we will have both $\nu_{i,k}$ and ν_l vectors and so

$$S(i) \cap S(k) \subseteq S(l) \rightarrow S(i,k) \subseteq S(l) \tag{A.1}$$

with $S(i,k)$ corresponding to the constructed vector $\nu_{i,k}$.

2. Row l in the m^{th} tableau does not have a zero element in the $m^{th}+1$ column so it has to be paired with another row to construct an appropriate vector for $m^{th}+1$ tableau. Clearly, row l can be added to i or k since one and only one of them has a nonzero element with a appropriate sign for combination with the row l. Without loss of generality, let us consider that to be row k. In this case the new vector $\nu_{l,k}$ is constructed for the new tableau, and in the $m+1^{th}$ tableau we will have the $\nu_{(i,k)}$ and $\nu_{l,k}$ and so

$$S(i) \cap S(k) \subseteq S(l) \rightarrow S(i,k) \subseteq S(l,k) \tag{A.2}$$

which is represented by the Venn diagram of Figure A.1

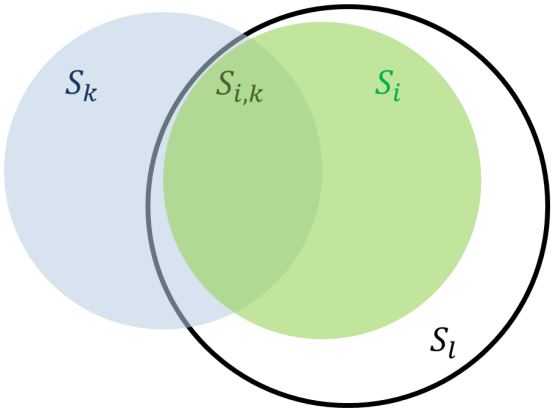

Figure A.1: An example Venn diagram representing $S(i) \cap S(k) \subseteq S(l) \rightarrow S(i,k) \subseteq S(l,k)$.

This completes the proof that both approaches to removing redundant vectors from the generating set are equivalent. Note that we started with a pair of rows (i, k) which the first approach rejects, and showed that proceeding with that pair always results in a new vector $\nu_{(i,k)}$ in the next tableau that second approach rejects as well.

Appendix B: Construction of a systematically independent generating basis set for the invariant subspace

We already have shown that the criteria to build a set of systematically independent generating vectors for the invariant subspace or the invariant cone presented in the convex algorithm of chapters 2 and 3 are mathematically equivalent. Here we show that the condition set on step 3.C of the convex algorithm presented in chapter 3 guarantees that the result of performing the algorithm is a systematically independent basis set.

The mathematical proof provided here closely follows the one presented in [69]. Note that the step 3.C in the convex algorithm implies that for a set of generating vectors $\{p_1, p_2, ..., p_q\}$ defining the invariant cone, if there exist a p_j and $p_{j'}$ pair where $j \neq j'$ and $S(p_j) \subseteq S(p_{j'})$ (where S contains the indices of the elements which are zero as defined in chapter 3), then

$$p_j = \sum_{i \neq j} \lambda_i p_i \quad \lambda_i \geq 0 \tag{B.1}$$

meaning that the set is not systematically independent and vector p_j can be written as s positive combination of others and hence is redundant.

To prove, assume that for two vectors $(p_j, p_{j'})$ we have $S(p_j) \subseteq S(p_{j'})$. Therefore, there exist a $\mu > 0$ that gives $\nu^* = p_j - \mu.p_{j'}$ with non-negative elements and

$S(p_j) \subseteq S(\nu^*)$. Taking the μ

$$\mu = min\{\frac{p_{j,i}}{p_{j',i}} | i = 1, ..., n \quad \text{and} \quad i \notin S(p_{j'})\} \tag{B.2}$$

gives

$$\nu_i^* = p_{j,i} - \mu p_{j',i} \geqslant p_{j,i} - \frac{p_{j,i}}{p_{j',i}} \times p_{j'.i} = 0 \tag{B.3}$$

for $i = 1, ..., n$. Note that this new vector ν is also a part of the invariant cone. Therefore, with $\lambda_i \geqslant 0$

$$\nu^* = \sum_{i=1}^{q} \lambda_i p_i = \lambda_j p_j + \sum_{i \neq j} \lambda_i p_i \tag{B.4}$$

Taking $\lambda_j > 0$ gives

$$S(\nu^*) = S(p_j) \cap S(\sum_{i \neq j} \lambda_i p_i) = S(p_j) \cap (\bigcap_{i \neq j} S(p_i)) \tag{B.5}$$

Note that since all p_i vectors are constructed from nonnegative elements, their nonnegative linear combination has zero element if and only if all p_is have zero in the corresponding element.

Following the same logic, from (B.3) we have

$$S(p_j) = S(\nu^* + \mu.p_{j'}) = S(\nu^*) \cap S(p_{j'}) \tag{B.6}$$

Substituting (B.5) in (B.6) we have

$$S(p_j) = S(p_j) \cap S(p_{j'}) \cap (\bigcap_{i \neq j} S(p_i)) \tag{B.7}$$

Since $S(p_j) \subseteq S(p_{j'})$, and using (B.5) this gives

$$S(p_j) = S(p_j) \cap (\bigcap_{i \neq j} S(p_i)) = S(\nu^*) \tag{B.8}$$

However, $S(p_j) \subseteq S(\nu^*)$ by construction which means (B.8) cannot be valid. This means $\lambda_j = 0$ and therefore,

$$p_j = \nu^* + \mu.p_{j'} = \mu.p_{j'} + \sum_{i \neq j} \lambda_i p_i \tag{B.9}$$

Which means that p_j indeed can be written as a non-negative linear combination of other vectors and so is redundant. This finishes the proof and confirms that the step 3.C in the algorithm is needed to produce a systematically independent set defining the invariant cone. Note that, as done in chapter 3, this can be extended to study of RN variants since, as it was shown, variant states are the invariant states of the reduce RN.

Appendix C: Remained variant states associated with propane oxidation RN

For variants associated with reactions f_1 and f_2 in the RN of Table 3.1 the last tableau upon performing the convex algorithm reads:

For f_1:

$$\mathbf{T}^{j=3} = \left[\begin{array}{ccc|cccccc} 0 & -4 & 0 & 1 & 0 & 1 & 0 & 0 & 1 \\ 0 & 0 & 0 & 1 & 0 & 0 & 1 & 0 & 1 \\ 0 & -10 & 0 & 0 & 2 & 2 & 0 & 0 & 1 \\ 0 & -2 & 0 & 0 & 2 & 0 & 2 & 0 & 1 \\ 0 & 6 & 0 & 0 & 0 & 0 & 0 & 1 & 0 \end{array}\right] \tag{C.1}$$

where the second row re-generates an invariant state.

For f_2:

$$\mathbf{T}^{j=3} = \left[\begin{array}{ccc|cccccc} 0 & 0 & -6 & 3 & 0 & 3 & 0 & 2 & 0 \\ 0 & 0 & -6 & 0 & 6 & 6 & 0 & 5 & 0 \\ 0 & 0 & -6 & 0 & 6 & 0 & 6 & 1 & 0 \\ 0 & 0 & -2 & 1 & 0 & 0 & 1 & 0 & 0 \\ 0 & 0 & 2 & 0 & 0 & 0 & 0 & 0 & 1 \end{array}\right] \tag{C.2}$$

Appendix D: Arbitary rate equations and rate parameters used to simulate the RN of Table 3.1

The following arbitrary rate equations are used to simulate the dynamics of example RN of Table 3.1.

$$f_0 = k_0 * n_{C_3H_8} * n_{O_2}$$

$$f_1 = k_1 * n_{C_3H_8} * n_{O_2}$$

$$f_2 = k_2 * n_{C_3H_8} * n_{O_2}$$

where $k_i = 1 \times 10^{10} \times exp(-E_i/RT)$ has the consistent unit; and $E_0 = 60$ kJ, $E_1 = 63$ kJ , $E_2 = 66$ kJ. This gives the following system of ODEs for the corresponding system.

$$\frac{dn_{\text{Prop}}}{dt} = -(1 \times f_0) - (4 \times f_1) - (2 \times f_2)$$
$$\frac{dn_{O_2}}{dt} = -(1 \times f_0) - (5 \times f_1) - (1 \times f_2)$$
$$\frac{dn_{\text{Acetone}}}{dt} = (1 \times f_0)$$
$$\frac{dn_{H_2O}}{dt} = (1 \times f_0) + (4 \times f_1)$$
$$\frac{dn_{\text{Acet}}}{dt} = (6 \times f_1)$$
$$\frac{dn_{\text{iPrOH}}}{dt} = (2 \times f_2)$$

Appendix E: Initial results for ALD of Ni and NiO thin-films for X-ray optics

As mentioned before in chapter 5, the simplest method to deposit a Ni thin-film with ALD is to deposit a NiO film and then reduce it to Ni using ex-situ reduction. Initial ALD experiments were preformed in the same reactor described in chapter 4 using the precursor system of $Ni(Cp)_2/O_3$ at 140 °C and on standard Si substrates; and the product was characterized using XPS and EDS. While both tests confirmed the deposition of Ni, significant amount of carbon was detected in the samples which signals the incomplete removal of the cyclopentadienyl group at this temperature. Furthermore, both methods confirm the ratio of O/Ni to be larger than one. The presence of Ni in higher oxidation states has been reported before for ALD processes that use ozone as the oxidizing agent [14]. The surface of the films deposited at this temperature was featureless when imaged by SEM. These films were also characterized by profilometry and XRR to investigate their potential for coating X-ray optics which proved them to be too rough for this specific application.

To completely remove the cyclopentadienyl groups, and potentially improve the roughness of the deposited film [102], the heating jacket on the reactor was replaced with a new heating wire capable of providing internal temperatures as high as 260 °C. Initial results confirm the presence of a self-limiting and complementary

ALD growth. Figure E.1(left) shows the gpc of NiO film on the standard Si substrate deposited at 245 °C as a function of $Ni(Cp)_2$ pulse time. Saturated gpc at 1 Å/cycle is consistent with the value reported by Lu et al. at the same temperature [102]. No variation was observed with respect to increasing O_3 pulses. Figure E.1(right) shows the thickness of the deposited film under the same condition with varying number of ALD cycles. A consistent growth corresponding to gpc of 0.7 Å/cycle is observed when using 0.6 s $Ni(Cp)_2$ pulse time. Furthermore, initial measurement results confirm improvements in surface roughness and film composition for the samples deposited at higher temperature.

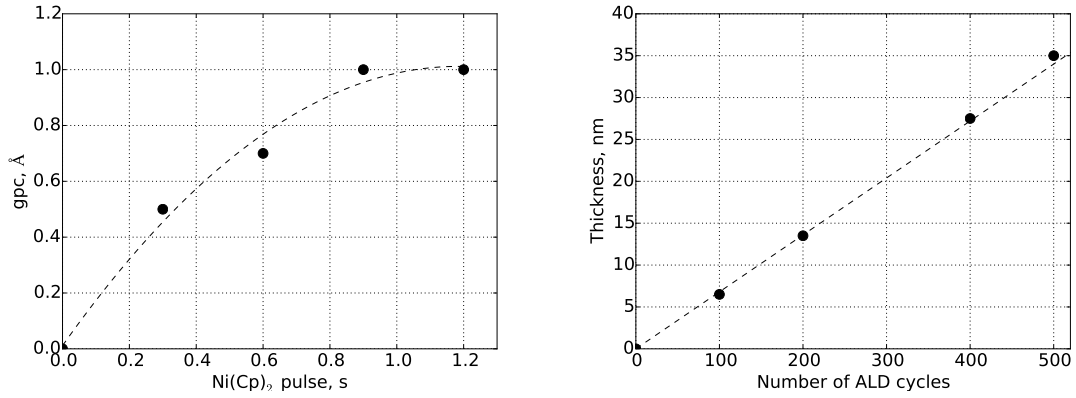

Figure E.1: gpc of NiO film deposited on Si substrate at 240°C as a function of $Ni(Cp)_2$ pulse time (left). The pulse time for the pneumatic valve was set to 0.3 s and longer pulses were achieved by performing multiple pulses. For all experiments the ozone pulse is fixed at 0.2 s with the same O_3/O_2 ratio as that of chapter 4. Thickness of the NiO film deposited on Si substrate as a function of ALD cycles with $Ni(Cp)_2$ pulse time fixed at 0.6 s (right).

Bibliography

[1] R. A. Adomaitis, Development of a multiscale model for an atomic layer deposition process. J. Cryst. Growth **312(8)**, 1449-1452 (2010).

[2] R. A. Adomaitis, Time-scale analysis of atomic layer deposition processes: Predicting the transition from mass-transfer to kinetically limited regimes. Phys. Status Solidi (c) **12(7)**, 934-943 (2015).

[3] R. A. Adomaitis, Dynamic order reduction of thin-film deposition kinetics models: A reaction factorization approach. J. Vac. Sci. Technol. A **34(1)**, 01A104 (2016).

[4] F. O. Adurodija, H. Izumi, T. Ishihara, H. Yoshioka, M. Motoyama, K. Murai, Influence of substrate temperature on the properties of indium oxide thin films. J. Vac. Sci. Technol. A **18**, 814-818 (2000).

[5] A. Afshar and K. Cadien, Growth mechanism of atomic layer deposition of zinc oxide: A density functional theory approach. App. Phys. Lett. **103**, 251906 (2013).

[6] R. E. Agbenyeke, E. A. Jung, B. K. Park, T. M. Chung, C. G. Kim, J. H. Han, Thermal atomic layer deposition of In2O3 thin films using dimethyl(N-ethoxy-2,2-dimethylcarboxylicpropanamide)indium and H2O. Appl. Surf. Sci. **419**, 758-63 (2017).

[7] E. Ahvenniemi et al., Review Article: Recommended reading list of early publications on atomic layer deposition- outcome of the virtual project on the history of ALD. J. Vac. Sci. Technol. A **35**, 010801 (2017).

[8] A. Alobaid, H. Salami, R. A. Adomaitis, On the computation and physical interpretation of semi-positive reaction network invariants. Comp. and Chem. Eng. **117**, 236-246 (2018).

[9] M. Amrhein, N. Bhatt, B. Srinivasan, D. Bonvin, Extents of reaction and flow for homogeneous reaction systems with inlet and outlet streams. AIChE J. **56(11)**, 2873-2886 (2010).

[10] O. A. Asbjørnsen and M. Fjeld, Response modes of continuous stirred tank reactors. Chem. Eng. Sci. **25**, 1627-36 (1970).

[11] O. A. Asbjørnsen, Reaction invariants in the control of continuous chemical reactors. Chem. Eng. Sci. **27**, 709-717 (1972).

[12] T. Asikainen, M. Ritala, M. Leskela, Growth of indium-tin-oxide thin films by atomic layer epitaxy. J. Electrochem. Soc. **142**, 3538-41 (1995).

[13] T. Asikainen, M. Ritala, M. Leskela, Growth of In2O3 thin films by atomic layer epitaxy. J. Electrochem. Soc. **141**, 3210-3 (1994).

[14] J. Bachmann, A. Zolotaryov, O. Albrecht, S. Goetze, A. Berger, D. Hesse, D. Novikov, K. Nielsch, Stoichiometry of nickel oxide films prepared by ALD. Chem. Vap. Depos. **17**, 177-180 (2011).

[15] M. Baldea, P. Daoutidis, A. Kumar, Dynamics and control of integrated networks with purge streams. AIChE J. **52**, 1460-1472 (2006).

[16] R. Bayon, C. Maffiotte, J. Herrero, Chemical bath deposition of indium hydroxy sulphide thin films: Process and XPS characterization. Thin Solid Films **353**, 100-107 (1999).

[17] J. R. Bellingham, A. P. Mackenzie, W. A. Phillips, Precise measurements of oxygen content: Oxygen vacancies in transparent conducting indium oxide films. Appl. Phys. Lett. **58**, 2506-8 (1991).

[18] M. Bender, N. Katsarakis, E. Gagaoudakis, E. Hourdakis, E. Douloufakis, V. Cimalla, G. Kiriakidis, Dependence of the photoreduction and oxidation behavior of indium oxide films on substrate temperature and film thickness. J. Appl. Phys. **90**, 5382-7 (2001).

[19] O. M. Berengue, C. A. Amorim, H. Kamimura, A. J. Chiquito, E. R. Leite, Oxygen-induced metal-insulator-transition on single crystalline metal oxide wires. J. Appl. Phys. **111**, 013713 (2012).

[20] N. Bhatt, N. Kerimoglu, M. Amrhein, W. Marquardt, D. Bonvin, Incremental identification of reaction systems- A comparison between rate-based and extent-based approaches. Chem. Eng. Sci. **83**, 24-38 (2012).

[21] O. Bierwagen, Indium oxide - a transparent, wide-band gap semiconductor for (opto)electronic applications. Semicond. Sci. Technol. **30**, 024001 (2015).

[22] J. Billeter, D. Rodrigues, S. Srinivasan, M. Amrhein, D. Bonvin, On decoupling rate processes in chemical reaction systems- Methods and applications. Comput. Chem. Eng. **114**, 296-305 (2018).

[23] N. Biyikli, A. Haider, Atomic layer deposition: An enabling technology for the growth of functional nanoscale semiconductors. Sem. Sci. and Technol. **32**, 093002 (2017).

[24] P. H. Bjornbom, The independent reactions in calculations of complex chemical equilibria. Ind. Eng. Chem. Fundam. **14(2)**, 102-106 (1975).

[25] D. Bonvin and D. W. T. Rippin, Target factor analysis for the identification of stoichiometric models. Chem. Eng. Sci. **45(12)**, 3417-3426 (1990).

[26] S. Boyd, L. Vandenberghe, Convex optimization. 12th printing, Cambridge University Press, New York (2013).

[27] D. B. Buchholz, Q. Ma, D. Alducin, A. Ponce, M. Jose-Yacaman, R. Khanal, J. E. Medvedeva, R. P. Chang, The structure and properties of amorphous indium oxide. Chem. Mater. **26**, 5401-5411 (2014).

[28] J. Chae, H. S. Park, S. W. Kang, Atomic layer deposition of nickel by the reduction of preformed nickel oxide. Electrochem. solid-state lett. **5(6)**, C64-C66 (2002).

[29] S. H. Chan, M. C. Li, H. S. Wei, S. H. Chen, C. C. Kuo, The effect of annealing on nanothick indium tin oxide transparent conductive films for touch sensors. Journal of Nanomaterials **1**, (2015).

[30] M. W. Chase, NIST-JANAF Themochemical Tables 4th Eds., J. Phys. Chem. Ref. Data **9**, (1998). NIST Chemistry WebBook, National Institute of Standards and Technology, Gaithersburg MD, USA, www.webbook.nist.gov, retrieved January 25 (2019).

[31] S. Chen, M. G. Mason, H. J. Gysling, G. R. Paz-Pujalt, T. N. Blanton, T. Castro, K. M. Chen, C. P. Fictorie, W. L. Gladfelter, A. Franciosi, P. I. Cohen, J. F. Evans, Ultrahigh vacuum metalorganic chemical vapor deposition growth and in situ characterization of epitaxial TiO2 films. J. Vac. Sci. Technol. A **11**, 2419 (1993).

[32] D. W. Choi and J. S. Park, Highly conductive SnO2 thin films deposited by atomic layer deposition using tetrakis-dimethyl-amine-tin precursor and ozone reactant. Surface and Coatings Technology **259**, 238-243 (2014).

[33] D. J. Comstock and J. W. Elam, Atomic layer deposition of Ga2O3 films using trimethylgallium and ozone. Chem. Mater. **24**, 4011-8 (2012).

[34] G. Craciun and M. Feinberg, Multiple equilibria in complex chemical reaction networks: II. The species-reaction graph. SIAM J. Appl. Math. **66**, 1321-1338 (2006).

[35] P. Daoutidis, DAEs in model reduction of chemical processes: An overview, in A. Ilchmann and T. Reis, (Eds.), Surveys in Differential-Algebraic Equations II. Springer International Publishing, New York (2015).

[36] J. H. De Wit, Electrical properties of In2O3. J. Solid State Chem. **8**, 142-9 (1973).

[37] A. Delabie, S. Sioncke, J. Rip, S. Van Elshocht, G. Pourtois, M. Mueller, B. Beckhoff, K. Pierloot, Reaction mechanisms for atomic layer deposition of aluminum oxide on semiconductor substrates. J. Vac. Sci. Technol. A **30(1)**, 01A127 (2012).

[38] Y. Dong, P. Zhang, Y. Kou, Z. Yang, Y. Li, X. Sun, A first-principles study of oxygen formation over NiFe-layered double hydroxides surface. Catalysis Letters. **145(8)**, 1541-1548 (2015).

[39] J. W. Elam, D. A. Baker, A. B. Martinson, M. J. Pellin, J. T. Hupp, Atomic layer deposition of indium tin oxide thin films using non-halogenated precursors. J. Phys. Chem. A **112**, 1938-45 (2008).

[40] J. W. Elam, A. B. Martinson, M. J. Pellin, J. T. Hupp, Atomic layer deposition of In2O3 using cyclopentadienyl indium: A new synthetic route to transparent conducting oxide films. Chem. Mater. **18**, 3571-8 (2006).

[41] J. W. Elam, J. A. Libera, J. N. Hryn, Indium oxide ALD using cyclopentadienyl indium and mixtures of H2O and O2. ECS Transactions **41**, 147-155 (2011).

[42] S. D. Elliott, G. Scarel, C. Wiemer, M. Fanciulli, G. Pavia, Ozone-based atomic layer deposition of alumina from TMA: Growth, morphology, and reaction mechanism. Chem. Mater. **18**, 3764-73 (2006).

[43] S. D. Elliott and J. C. Greer, Simulating the atomic layer deposition of alumina from first principles. J. Mater. Chem. **14**, 3246-50 (2004).

[44] I. Famili and B. O. Palsson, The convex basis of the left null space of the stoichiometric matrix leads to the definition of metabolically meaningful pools. Biophys. J. **85(1)**, 16-26 (2003).

[45] Y. Fang, G. Yeh, W. D. Burgos, A general paradigm to model reaction-based biogeochemical processes in batch systems. Water Resources Research **39(4)**, 1083 (2003).

[46] E. Feliu and C. Wiuf, Simplifying biochemical models with intermediate species. J. R. Soc. Interface. **10(87)**, 20130484 (2013).

[47] G. Frank and H. Kostlin, Electrical properties and defect model of tin-doped indium oxide layers. Appl. Phys. A **27**, 197-206 (1982).

[48] D. M. Fryauf, A. C. Phillips, M. J. Bolte, A. Feldman, G. S. Tompa, N. P. Kobayashi, Scaling atomic layer deposition to astronomical optic sizes: Low-temperature aluminum oxide in a meter-sized chamber. ACS Appl. Mater. Interfaces **10(48)**, 41678-41689 (2018).

[49] H. Fritzsche, B. Pashmakov, B. Claflin, Reversible changes of the optical and electrical properties of amorphous InOx by photoreduction and oxidation. Sol. Energy Mater. Sol. Cells **32**, 383-93 (1994).

[50] S. B. Gadewar, M. F. Doherty, M. F. Malone, A systematic method for reaction invariants and mole balances for complex chemistries. Comput. Chem. Eng. **25(9)**, 11991217 (2001).

[51] S. B. Gadewar, M. F. Doherty, M. F. Malone, Reaction invariants and mole balances for plant complexes. Ind. Eng. Chem. Res. **41(16)**, 3771-3783 (2002).

[52] G. P. Gakis, H. Vergnes, E. Scheid, C. Vahlas, B. Caussat, A. G. Boudouvis, Computational fluid dynamics simulation of the ALD of alumina from TMA and H2O in a commercial reactor. Chem. Eng. Res. Des. **132**, 795-811 (2018).

[53] Z. Gao, F. Wu, Y. Myung, R. Fei, R. Kanjolia, L. Yang, P. Banerjee, Standing and sitting adlayers in atomic layer deposition of ZnO. J. Vac. Sci. Technol. A **34(1)**, 01A143 (2016).

[54] S. M. George, Atomic layer deposition: An overview. Chem. Rev. **110**, 111-131 (2009).

[55] D. Gilmore, Spacecraft thermal control handbook, volume I: Fundamental technologies. The Aerospace Press, El Segundo (2002)

[56] M. Girtan, Investigations on the optical constants of indium oxide thin films prepared by ultrasonic spray pyrolysis. Materials Science and Engineering: B **118**, 175-178 (2005).

[57] E. S. Goh, T. P. Chen, C. Q. Sun, Y. C. Liu, Thickness effect on the band gap and optical properties of germanium thin films. J. Appl. Phys. **107**, 024305 (2010).

[58] D. N. Goldstein, J. A. McCormick, S. M. George, Al2O3 atomic layer deposition with trimethylaluminum and ozone studied by in situ transmission FTIR spectroscopy and quadrupole mass spectrometry. J. Phys. Chem. C **112**, 19530-9 (2008).

[59] G. B. Gonzlez, J. S. Okasinski, D. B. Buchholz, J. Boesso, J. D. Almer, L. Zeng, M. J. Bedzyk, R. P. H. Chang, Relationship between electrical properties and crystallization of indium oxide thin films using ex-situ grazing-incidence wide-angle x-ray scattering. J. Appl. Phys. **121**, 205306 (2017).

[60] Google Scholar search. Key words used:"atomic layer deposition" and "thin film", retrieved April 22 (2019).

[61] T. D. Gould, A. M. Lubers, B. T. Neltner, J. V. Carrier, A. W. Weimer, J. L. Falconer, J. W. Medlin, Synthesis of supported Ni catalysts by atomic layer deposition. J. of Catalysis **303**, 9-15 (2013).

[62] P. Gray, S. K. Scott, J. H. Merkin, The Brusselator model of oscillatory reactions relationships. J. Chem. Soc. Faraday Trans. I **84(4)**, 993-1011 (1988).

[63] C. W. Groetsch and J. T. King, Matrix Methods and Applications. Prentice Hall, Englewood Cliffs (1998).

[64] J. Guo, H. van Bui, D. Valdesueiro, S. Yuan, B. Liang, J. R. van Ommen, Suppressing the photocatalytic activity of TiO2 nanoparticles by extremely thin Al2O3 films grown by gas-phase deposition at ambient conditions. Nanomaterials **8(2)**, 61 (2018).

[65] U. Gupta, S. Heo, A. Bhan, P. Daoutidis, Time scale decomposition in complex reaction systems: A graph theoretic analysis. Comput. Chem. Eng. **95**, 170-181 (2016).

[66] T. Gustafsson and K. Waller, Dynamic modeling and reaction invariant control of pH. Chem. Eng. Sci. **38(3)**, 389-398 (1983).

[67] L. F. Hakim, J. Blackson, S. M. George, A. W. Weimer, Nanocoating individual silica nanoparticles by atomic layer deposition in a fluidized bed reactor. Chem. Vap. Depos. **11(10)**, 420-425 (2005).

[68] Y. Han, D. Kim, J. S. Cho, Y. W. Beag, S. K. Koh, V. S. Chernysh, Effects of substrate treatment on the initial growth mode of indium-tin-oxide films. J. Appl. Phys. **97**, 024910 (2005).

[69] S. Hille, Lecture notes, Leiden University (2017).

[70] L. B. Hoch, L. He, Q. Qiao, K. Liao, L. M. Reyes, Y. Zhu, G. A. Ozin, Effect of precursor selection on the photocatalytic performance of indium oxide nanomaterials for gas-phase CO2 reduction. Chem. Mater. **28**, 4160-4168 (2016).

[71] S. Honda, M. Watamori, K. Oura, The effects of oxygen content on electrical and optical properties of indium tin oxide films fabricated by reactive sputtering. Thin Solid Films **281**, 206-8 (1996).

[72] J. H. Hwang, D. D. Edwards, D. R. Kammler, T. O. Mason, Point defects and electrical properties of Sn-doped In-based transparent conducting oxides. Solid State Ionics **129**, 135-44 (1996).

[73] C. S. Hwang, Atomic Layer Deposition for Semiconductors. Springer, New York (2014).

[74] V. Dwivedi, M. Hasegawa, R. A. Adomaitis, H. Salami, A. Uy, Modification of radiator pigments by atomic layer deposition. 48th International Conference on Environmental Systems, (2013).

[75] K. Irmscher, M. Naumann, M. Pietsch, Z. Galazka, R. Uecker, T. Schulz, R. Schewski, M. Albrecht, R. Fornari, On the nature and temperature dependence of the fundamental band gap of In2O3. Phys. Status Solid (a) **211**, 54-8 (2013).

[76] T. O. Kaariainen, M. Kemell, M. Vehkamaki, M. Kaariainen, A. Correia, H. A. Santos, L. M. Bimbo, J. Hirvonen, P. Hoppu, S. M. George, D. C. Cameron, M. Ritala, M. Leskela, Surface modification of acetaminophen particles by atomic layer deposition. Int. J. Pharm. **52(1)**, 160-174 (2017).

[77] R. L. Karp, M. P. Milln, T. Dasgupta, A. Dickenstein, J. Gunawardena, Complex-linear invariants of biochemical networks. J. Theor. Biol. **311**, 130-138 (2012).

[78] L. Kauder, Spacecraft thermal control coatings references. Technical report No. TP-2005-212792, NASA Goddard Space Flight Center, Greenbelt, MD, United States (2005).

[79] D. K. Kaushik, K. U. Kumar, A. Subrahmanyam, Metal-insulator transition in tin doped indium oxide (ITO) thin films: Quantum correction to the electrical conductivity. AIP Advances **7**, 015109 (2017).

[80] F. Keywell and G. Dorosheski, Measurement of the sheet resistivity of a square wafer with a square fourpoint probe. Rev. Sci. Instrum. **31**, 833-7 (1960).

[81] R. Khanal, Properties of amorphous transparent conducting and semiconducting oxides from first principles. Doctoral dissertation, Missouri University of Science and Technology (2016).

[82] N. M. Khusayfan, M. M. El-Nahass, Study of structure and electro-optical characteristics of indium tin oxide thin films. Advances in Condensed Matter Physics, (2013).

[83] K. Kikuchi, M. Miura, K. Kanomata, B. Ahmmad, S. Kubota, F. Hirose, Room temperature atomic layer deposition of TiO2 on gold nanoparticles. J. Vac. Sci. Technol. A **35(1)**, 01B121 (2017).

[84] S. B. Kim, A. Jayaraman, D. Chua, L. M. Davis, S. L. Zheng, X. Zhao, S. Lee, R. G. Gordon, Obtaining a low and wide atomic layer deposition window (150-275C) for In2O3 films using an In(III) amidinate and H2O. Chemistry- A European Journal, (2018).

[85] H. Kind, H. Yan, B. Messer, M. Law, P. Yang, Nanowire ultraviolet photodetectors and optical switches. Adv. Mater. **14**, 158-60 (2002).

[86] D. M. King, X. Liang, C. S. Carney, L. F. Hakim, P. Li, A. W. Weimer, Atomic layer deposition of UV-absorbing ZnO films on SiO2 and TiO2 nanoparticles using a fluidized bed reactor. Adv. Funct. Mater. **18(4)**, 607-615 (2008).

[87] G. Kiriakidis, M. Bender, N. Katsarakis, E. Gagaoudakis, E. Hourdakis, E. Douloufakis, V. Cimalla, Ozone sensing properties of polycrystalline indium oxide films at room temperature. Phys. Status Solidi A **185**, 27-32 (2001).

[88] T. Koida, H. Fujiwara, M. Kondo, Hydrogen-doped In2O3 as high-mobility transparent conductive oxide. Jpn. J. Appl. Phys. **46**, L685 (2007).

[89] V. Korobov, M. Leibovitch, Y. Shapira, Structure and conductance evolution of very thin indium oxide films. Appl. Phys. Lett. **65**, 2290-2 (1994).

[90] G. Korotcenkov, V. Brinzari, A. Cerneavschi, M. Ivanov, V. Golovanov, A. Cornet, J. Morante, A. Cabot, J. Arbiol, The influence of film structure on In2O3 gas response. Thin Solid Films **460**, 315-23 (2004).

[91] N. Krstaji, M. Popovi, B. Grgur, M. Vojnovi, D. Sepa, On the kinetics of the hydrogen evolution reaction on nickel in alkaline solution Part I. The mechanism. J. of Electroanalytical Chemistry **512(1)**, 16-26 (2001).

[92] K. J. Laidler, Chemical Kinetics, 3rd ed. Harper and Row, New York (1987).

[93] D. J. Lee, J. Y. Kwon, J. I. Lee, K. B. Kim, Self-limiting film growth of transparent conducting In2O3 by atomic layer deposition using trimethylindium and water vapor. J. Phys. Chem. C **115**, 15384-9 (2011).

[94] M. Leskela and M. Ritala, Atomic layer deposition (ALD): From precursors to thin film structures. Thin Solid Films **409**, 138-146 (2002).

[95] D. H. Levy and S. F. Nelson, Thin-film electronics by atomic layer deposition. J. Vac. Sci. Technol. A **30**, 018501 (2012).

[96] E. G. Lewars, Computational chemistry, introduction to the theory and applications of molecular and quantum mechanics. 2nd ed., Springer, New York (2011)

[97] C. Li, D. Zhang, X. Liu, S. Han, T. Tang, J. Han, C. Zhou, In2O3 nanowires as chemical sensors. Appl. Phys. Lett. **82**, 1613-5 (2003).

[98] J. A. Libera, J. N. Hryn, J. W. Elam, Indium oxide atomic layer deposition facilitated by the synergy between oxygen and water. Chem. Mater. **23**, 2150-8 (2011).

[99] J. Liu, G. Chen, Y. Yu, Y. Wu, M. Zhou, H. Zhang, C. Lv, Y. Zheng, F. He, Controllable synthesis of In2O3 octodecahedra exposing 110 facets with enhanced gas sensing performance. RSC. Advances **5**, 44306-12 (2015).

[100] A. Locy and B. S. Ault, Matrix isolation study of the thermal and photochemical reaction of ozone with Trimethylindium. Chem. Phys. **392**, 192-7 (2012).

[101] A. Lu, J. Paulson, R. Braatz, PH and conductivity control in an integrated biomanufacturing plant. Proceedings of the American Control Conference (ACC), 1741-1746 (2016).

[102] H. L. Lu, G. Scarel, C. Wiemer, M. Perego, S. Spiga, M. Fanciulli, G. Pavia, Atomic layer deposition of NiO films on Si(100) using cyclopentadienyl-type compounds and ozone as precursors. J. Electrochem. Soc. **155**, H807-H811 (2008).

[103] A. J. Mackus, C. MacIsaac, W. H. Kim, S. F. Bent, Incomplete elimination of precursor ligands during atomic layer deposition of zinc-oxide, tin-oxide, and zinc-tin-oxide. J. Chem. Phys. **146**, 052802 (2017).

[104] W. J. Maeng, D. W. Choi, J. Park, J. S. Park, Atomic layer deposition of highly conductive indium oxide using a liquid precursor and water oxidant. Ceram. Int. **41**, 10782-7 (2015).

[105] W. J. Maeng, D. W. Choi, K. B. Chung, W. Koh, G. Y. Kim, S. Y. Choi, J. S. Park, Highly conducting, transparent, and flexible indium oxide thin film prepared by atomic layer deposition using a new liquid precursor Et2InN(SiMe3)2. ACS Appl. Mater. Interfaces **6**, 17481-8 (2014).

[106] W. J. Maeng, D. W. Choi, J. Park, J. S. Park, Indium oxide thin film prepared by low temperature atomic layer deposition using liquid precursors and ozone oxidant. J. Alloys Compd. **649**, 216-21 (2015).

[107] A. U. Mane, A. J. Allen, R. K. Kanjolia, J. W. Elam, Indium oxide thin films by atomic layer deposition using trimethylindium and ozone. J. Phys. Chem. C **120**, 9874-83 (2016).

[108] R. Matero, A. Rahtu, M. Ritala, M. Leskela, T. Sajavaara, Effect of water dose on the atomic layer deposition rate of oxide thin films. Thin Solid Films **368**, 1-7 (2000).

[109] T. McAvoy, E. Hsu, S. Lowenthal, Dynamics of pH in controlled stirred tank reactor. Industrial Engineering Chemistry Process Design and Development **11(1)**, 68-70 (1972).

[110] J. A. McCormick, B. L. Cloutier, A. W. Weimer, S. M. George, Rotary reactor for atomic layer deposition on large quantities of nanoparticles. J. Vac. Sci. Technol. A **25(1)**, 67-74 (2007).

[111] W. W. McNeary, A. E. Linico, C. Ngo, S. van Rooij, S. Haussener, M. E. Maguire, S. Pylypenko, A. W. Weimer, Atomic layer deposition of TiO2 for stabilization of Pt nanoparticle oxygen reduction reaction catalysts. J. Appl. Electrochem. **48(9)**, 973-984 (2018).

[112] G. A. Mei-Zhen, R. Job, X. De-Sheng, W. R. Fahrner, Thickness dependence of resistivity and optical reflectance of ITO films. Chinese Phy. Lett. **25**, 1380 (2008).

[113] V. Miikkulainen, M. Leskelä, M. Ritala, R. L. Puurunen, Crystallinity of inorganic films grown by atomic layer deposition: Overview and general trends. J. Appl. Phys. **113(2)**, 021301 (2013).

[114] D. Ming, D. Glasser, D. Hildebrandt, B. Glasser, M. Metzger, Attainable Region Theory; An Introduction to Choosing an Optimal Reactor. J. Wiley and Sons, New Jersey (2016).

[115] A. Mohammadi, F. Behafarid, G. Kavei, M. Kazemzad, Effect of sputtering pressure and annealing temperature on the properties of indium tin oxide thin films. Materials Science and Engineering: B **136**, 37-40 (2007).

[116] P. Moravec, J. Smolik, H. Keskinen, J. M. Mkel, S. Bakardjieva, V. V. Levdansky, NiOx nanoparticle synthesis by chemical vapor deposition from nickel acetylacetonate. Mater. Sci. Appl. **2**, 258 (2011).

[117] H. Morikawa, H. Sumi, M. Kohyama, Crystal growth of ITO films prepared by DC magnetron sputtering on C film. Thin Solid Films **281**, 202-5 (1996).

[118] H. Morikawa and M. Fujita, Crystallization and decrease in resistivity on heat treatment of amorphous indium tin oxide thin films prepared by d.c. magnetron sputtering. Thin Solid Films **339**, 309-13 (1999).

[119] H. Morikawa and M. Fujita, Crystallization and electrical property change on the annealing of amorphous indium-oxide and indium-tin-oxide thin films. Thin Solid Films **359**, 61-7 (2000).

[120] B. A. Morrow and R. A. McFarlane, Trimethylgallium adsorbed on silica and its reaction with phosphine, arsine, and hydrogen chloride: an infrared and Raman study. J. Phys. Chem. **90**, 3192-7 (1986).

[121] T. Muneshwar and K. Cadien, Surface reaction kinetics in atomic layer deposition: An analytical model and experiments. J. App. Phys. **124(9)**, 095302 (2018).

[122] S. Muranaka, Crystallization of amorphous In2O3 films during film growth. Jpn. J. Appl. Phys. **30**, L2062 (1991).

[123] S. Muranaka and N. Hayashi, Thickness-induced crystallization of amorphous In2O3 films: Influence of the film deposition rate. J. Mater. Sci. **44**, 3315-8 (2009).

[124] K. L. Nardi, N. Yang, C. F. Dickens, A. L. Strickler, S. F. Bent, Creating highly active atomic layer deposited NiO electrocatalysts for the oxygen evolution reaction. Adv. Energy Mat. **5(17)**, 1500412 (2015).

[125] H. G. Othmer, Lecture notes, Rutgers University (1981).

[126] A. W. Ott, J. M. Johnson, J. W. Klaus, S. M. George, Surface chemistry of In2O3 deposition using In(CH3)3 and H2O in a binary reaction sequence. Appl. Surf. Sci. **112**, 205-215 (1997).

[127] D. C. Paine, T. Whitson, D. Janiac, R. Beresford, C. O. Yang, B. Lewis, A study of low temperature crystallization of amorphous thin film indiumtinoxide. J. Appl. Phys. **85**, 8445-50 (1999).

[128] J. H. Park, C. Buurma, S. Sivananthan, R. Kodama, W. Gao, T. A. Gessert, The effect of post-annealing on Indium Tin Oxide thin films by magnetron sputtering method. Appl. Surf. Sci. **307**, 388-93 (2014).

[129] G. Parsons, Functional model for analysis of ALD nucleation and quantification of area-selective deposition. J. Vac. Sci. Technol. A **37(2)**, 020911 (2019).

[130] B. Pashmakov, B. Claflin, H. Fritzsche, Photoreduction and oxidation of amorphous indium oxide. Solid State Commun. **86**, 619-22 (1993).

[131] R. L. Puurunen, A short history of atomic layer deposition: Tuomo Suntola's atomic layer epitaxy. Chem. Vap. Depos. **20(10)**, 332-344 (2014).

[132] R. L. Puurunen, Growth per cycle in atomic layer deposition a theoretical model. Chem. Vap. Depos. **9**, 249-257 (2003).

[133] A. Rautiainen, M. Lindblad, L. B. Backmanb, R. L. Puurunen, Preparation of silica-supported cobalt catalysts through chemisorption of cobalt(II) and cobalt(III) acetylacetonate. Phys. Chem. Chem. Phys. **4**, 2466-2472 (2002).

[134] M. Reinke, Y. Kuzminykh, P. Hoffmann, Surface kinetics of titanium isopropoxide in high vacuum chemical vapor deposition. J. Phys. Chem. C **119**, 2796527971 (2015).

[135] M. Reinke, Y. Kuzminykh, P. Hoffmann, Low temperature chemical vapor deposition using atomic layer deposition chemistry. Chem. Mater. **27(5)**, 1604-1611 (2015).

[136] E. M. Remmers, C. D. Travis, R. A. Adomaitis, Reaction factorization for the dynamic analysis of atomic layer deposition kinetics. Chem. Eng. Sci. **127**, 374-391 (2015).

[137] S. K. Rhee, Surface energies of silicate glasses calculated from their wettability data. J. Mater. Sci. **12**, 823-824 (1977).

[138] M. Ritala, T. Asikainen, M. Leskela, Enhanced growth rate in atomic layer epitaxy of indium oxide and indiumtin oxide thin films. Electrochem. Solid-State Lett. **1**, 156-7 (1998).

[139] M. Ritala, J. Niinisto, Atomic layer deposition, in A. C. Jones and M. L. Hitchman Chemical Vapor Deposition: Precursors, Processes and Applications. Royal Society of Chemistry (2009).

[140] J. Robertson and B. Falabretti, Electronic structure of transparent conducting oxides, in Handbook of Transparent Conductors. Springer, Boston, 27-50 (2011).

[141] D. Rodrigues, S. Srinivasan, J. Billeter, D. Bonvin, Variant and invariant states for chemical reaction systems. Comput. Chem. Eng. **73**, 23-33 (2015).

[142] M. R. Roussel and S. J. Fraser, Invariant manifold methods for metabolic model reduction. Chaos **11**, 196 (2001).

[143] H. Salami, K. Ramakrishnasubramanian, R. A. Adomaitis, Reaction path analysis for chemical vapor deposition and atomic layer deposition processes: A study of titania thin-film deposition. Phys. Status Solidi (b) **254(10)**, 1700091 (2017).

[144] H. Salami, A. Poissant, R. A. Adomaitis, Anomalously high alumina atomic layer deposition growth per cycle during trimethylaluminum under-dosing conditions. J. Vac. Sci. Technol. A **35(1)**, 01B101 (2017).

[145] H. Salami, A. Uy, A. Vadapalli, C. Grob, V. Dwivedi, R. A. Adomaitis, Atomic layer deposition of ultrathin indium oxide and indium tin oxide films using a trimethylindium, tetrakis (dimethylamino) tin, and ozone precursor system. J. Vac. Sci. Technol. A **37(1)**, 010905 (2019).

[146] S. Sanze and C. Hess, Ethanol gas sensing by indium oxide: An operando spectroscopic raman-FTIR study. J. Phys. Chem. C **118**, 25603-13 (2014).

[147] M. Sarr, N. Bahlawane, D. Arl, M. Dossot, E. McRae, D. Lenoble, Tailoring the properties of atomic layer deposited nickel and nickel carbide thin films via chain-length control of the alcohol reducing agents. J. Phys. Chem. C **118**, 23385-23392 (2014).

[148] Y. Sato, M. Taketomo, N. Ito, Y. Shigesato, Study on early stages of film growth for Sn doped In2O3 films deposited at various substrate temperatures. Thin Solid Films **516**, 5868-71 (2008).

[149] Y. Sato, M. Taketomo, N. Ito, A. Miyamura, Y. Shigesato, Comparative study on early stages of film growth for transparent conductive oxide films deposited by dc magnetron sputtering. Thin Solid Films **516**, 4598-4602 (2008).

[150] C. H. Schilling, S. Schuster, B. O. Palsson, R. Heinrich, Metabolic pathway analysis: Basic concepts and scientific applications in the post-genomic era. Biotechnology progress **15(3)**, 296-303 (1999).

[151] C. H. Schilling, D. Letscher, B. O. Palsson, Theory for the systemic definition of metabolic pathways and their use in interpreting metabolic function from a pathway-oriented perspective. J. Theor. Biol. **203(3)**, 229-248 (2000).

[152] S. Schuster and T. Hofer, Determining all extreme semi-positive conservation relations in chemical reaction systems: A test criterion for conservativity. J. Chem. Soc. Faraday Trans. **87(16)**, 2561-2566 (1991).

[153] R. Schuster and S. Schuster, Refined algorithm and computer program for calculating all non-negative fluxes admissible in steady states of biochemical reaction systems with or without some flux rates fixed. Bioinformatics **9(1)**, 79-85 (1993).

[154] S. Schuster and C. Hilgetag, What information about the conserved-moiety structure of chemical reaction systems can be derived from their stoichiometry? J. Phys. Chem. **99**, 8017-8023 (1995).

[155] W. D. Seider, D. R. lewin, J. D. Seader, S. Widagdo, R. Gani, K. M. Ng, Product and Process Design Principles: Synthesis, Analysis, and Evaluation, 4th ed. J. Wiley and Sons, New Jersey (2017).

[156] V. Senthilkumar, P. Vickraman, M. Jayachandran and C. Sanjeeviraja, Structural and optical properties of indium tin oxide (ITO) thin films with different compositions prepared by electron beam evaporation. Vacuum **84**, 864-9 (2010).

[157] D. Shah, D. I. Patel, T. Roychowdhury, G. B. Rayner, N. O'Toole, D. R. baer, M. R. Linford, Tutorial on interpreting x-ray photoelectron spectroscopy survey spectra: Questions and answers on spectra from the atomic layer deposition of Al2O3 on silicon. J. Vac. Sci. Technol. B **36**, 062902 (2018).

[158] D. V. Shenai-Khatkhate, R. L. DiCarlo, R. A. Ware, Accurate vapor pressure equation for trimethylindium in OMVPE. J. Cryst. Growth **310**, 2395-2398 (2008).

[159] Y. Shigesato and D. C. Paine, Study of the effect of Sn doping on the electronic transport properties of thin film indium oxide. Appl. Phys. Lett. **62**, 1268-70 (1993).

[160] V. Singh and P. K. Dhar, Systems and Synthetic Biology. Springer, Netherlands (2015).

[161] F. M. Smits, Measurement of the sheet resistivity with the four-point probe. Bell System Technical Journal **37**, 711-8 (1958).

[162] D. Spiga, A. Mirone, G. Pareschi, R. Canestrari, V. Cotroneo, C. Ferrari, C. Ferrero, L. Lazzarini, D. Vernani, Characterization of multilayer stack parameters from x-ray reflectivity data using the PPM program: measurements and comparison with TEM results. Proceeding of International Society for Optics and Photonics **6266**, 626616 (2006).

[163] J. K. Sprenger, H. Sun, A. S. Cavanagh, S. M. George, Electron-enhanced atomic layer deposition of silicon thin films at room temperature. J. Vac. Sci. Technol. A **36**, 01A118 (2018).

[164] B. Srinivasan, M. Amrhein, D. Bonvin, Reaction and flow variants/invariants in chemical reaction systems with inlet and outlet streams. AIChE J. **44(8)**, 1858-1867 (1998).

[165] J. Su, Z. Li, Y. Yu, X. Wang, Atomic layer deposition for advanced electrode design in photoelectrochemical and triboelectric systems. Advanced Materials Interfaces **4(4)**, 1600835 (2017).

[166] X. W. Sun, H. C. Huang, H. S. Kwok, On the initial growth of indium tin oxide on glass. Appl. Phys. Lett. **68**, 2663-5 (1996).

[167] T. Suzuki, T. Yamazaki, M. Takizawa, O. Kawasaki, Thickness dependence of electrical properties in thin films of undoped indium oxide prepared by ion-beam sputtering. J. Mater. Sci. **24**, 187-91 (1989).

[168] M. Thirumoorthi and J. Thomas Joseph Prakash, Structure, optical and electrical properties of indium tin oxide ultra thin films prepared by jet nebulizer spray pyrolysis technique. Journal of Asian Ceramic Societies **4**, 124-32 (2016).

[169] T. Tomita, K. Yamashita, Y. Hayafuji, H. Adachi, The origin of n-type conductivity in undoped In2O3. Appl. Phys. Lett. **87**, 051911 (1995).

[170] C. D. Travis and R. A. Adomaitis, Modeling alumina atomic layer deposition reaction kinetics during the trimethylaluminum exposure. Theor. Chem. Acc. **133(1)**, 1-11 (2013).

[171] C. D. Travis and R. A. Adomaitis, Dynamic modeling for the design and cyclic operation of an atomic layer deposition (ALD) reactor. Processes **1**, 128-52 (2013).

[172] M. Utriainen, M. Krger-Laukkanen, L. S. Johansson, L. Niinisto, Studies of metallic thin film growth in an atomic layer epitaxy reactor using M (acac)2 (M= Ni, Cu, Pt) precursors. Appl. Surf. Sci. **157(3)**, 151-158 (2000).

[173] M. Utriainen, M. Krger-Laukkanen, L. Niinisto, Studies of NiO thin film formation by atomic layer epitaxy. Mat. Sci. Eng. **54**, 98-103 (1998).

[174] J. R. van Ommen, U.S. Patent No. 15/813840 (15 March 2018).

[175] M. T. Vieyra-Eusebio, A. Rojas Vapor pressures and sublimation enthalpies of nickelocene and cobaltocene measured by thermogravimetry. J. Chem. Eng. Data **56(12)**, 5008-5018 (2011).

[176] N. Vora and P. Daoutidis, Nonlinear model reduction of chemical reaction systems. AIChE J. **47**, 2320-2332 (2001).

[177] A. Walsh and C. R. A. Catlow, Structure, stability and work functions of the low index surfaces of pure indium oxide and Sn-doped indium oxide (ITO) from density functional theory. J. Mater. Chem. **20**, 10438-10444 (2010).

[178] C. Y. Wang, V. Cimalla, T. Kups, C. C. Rhlig, H. Romanus, V. Lebedev, J. Pezoldt, T. Stauden, O. Ambacher, Photoreduction and oxidation behavior of In2O3 nanoparticles by metal organic chemical vapor deposition. J. Appl. Phys. **102**, 044310 (2007).

[179] C. Y. Wang, V. Cimalla, T. Kups, C. C. Rhlig, T. Stauden, O. Ambacher, M. Kunzer, T. Passow, W. Schirmacher, W. Pletschen, K. Khler, Integration of In2O3 nanoparticle based ozone sensors with GaInN/GaN light emitting diodes. Appl. Phys. Lett. **91**, 103509 (2007).

[180] C. Y. Wang, V. Cimalla, H. Romanus, T. Kups, M. Niebelschutz, O. Ambacher, Tuning of electrical and structural properties of indium oxide films grown by metal organic chemical vapor deposition. Thin Solid Films **515**, 6611-14 (2007).

[181] J. R. Wank, S. M. George, A. W. Weimer, Nanocoating individual cohesive boron nitride particles in a fluidized bed by ALD. Powder Technology **142(1)**, 59-69 (2004)

[182] T. Weckman and K. Laasonen, Atomic layer deposition of zinc oxide: Study on the water pulse reactions from first-principles. J. Phys. Chem. C. **122(14)**, 7685-7694 (2018).

[183] T. Weckman and K. Laasonen, Atomic layer deposition of zinc oxide: diethyl zinc reactions and surface saturation from first-principles. J. Phys. Chem. C **120(38)**, 21460-21471 (2016).

[184] C. Xirouchaki, K. Moschovis, E. Chatzitheodoridis, G. Kiriakidis, P. Morgen, Chemical characterization of as-deposited microcrystalline indium oxide films prepared by reactive dc magnetron sputtering. Appl. Phys. A **67**, 295-301 (1998).

[185] C. Xirouchaki, G. Kiriakidis, T. F. Pedersen, H. Fritzsche, Photoreduction and oxidation of asdeposited microcrystalline indium oxide. J. Appl. Phys. **79**, 9349-52 (1996).

[186] G. Yeh, W. D. Burgos, J. M. Zachara, Modeling and measuring biogeochemical reactions: System consistency, data needs, and rate formulations. Adv. Environ. Res. **5**, 219-237 (2001).

[187] H. I. Yeom, J. B. Ko, G. Mun, S. H. Park, High mobility polycrystalline indium oxide thin-film transistors by means of plasma-enhanced atomic layer deposition. J. Mater. Chem. C **4**, 6873-80 (2016).

[188] X. Zhou, J. Xu, L. Yang, G. Zhu and Z. Yu, Effects of tin content on structure, properties, electrical repeatability, uniformity and stability of high sheet resistance ITO thin films for touch panels. J. Mater. Sci: Mater. Electron **26**, 6954-60 (2015).

[189] www.lanl.gov, credit: NASA, retrieved April 15 (2019).

Publications and presentations

Peer-reviewed publications

1 H. Salami, A. Uy, A. Vadapalli, C. Grob, V. Dwivedi, R. A. Adomaitis, Atomic layer deposition of ultrathin indium oxide and indium tin oxide films using a trimethylindium, tetrakis (dimethylamino) tin, and ozone precursor system. *J. Vac. Sci. and Technol. A* **37(1)**, 010905 (2019).
https://doi.org/10.1116/1.5058171

2 A. Alobaid, H. Salami, R. A. Adomaitis, On the computation and physical interpretation of semi-positive reaction network invariants. *Comp. and Chem. Eng.* **117**, 236-246 (2018).
https://doi.org/10.1016/j.compchemeng.2018.06.009

3 H. Salami, K. Ramakrishnasubramanian, R. A. Adomaitis, Reaction path analysis for chemical vapor deposition and atomic layer deposition processes: A study of titania thin-film deposition. *physica status solidi (b)* **254(10)**, 1700091 (2017).
https://doi.org/10.1002/pssb.201700091

4 E. Ahvenniemi, A. R. Akbashev, S. Ali, M. Bechelany, M. Berdova, S. Boyadjiev, ... and A. Devi, Recommended reading list of early publications on atomic layer deposition - Outcome of the virtual project on the history of ALD. *J. Vac. Sci. and Technol. A* **35(1)**, 010801 (2017).
https://doi.org/10.1116/1.4971389

5 H. Salami, A. Poissant, R. A. Adomaitis, Anomalously high alumina atomic layer deposition growth per cycle during trimethylaluminum under-dosing conditions. *J. Vac. Sci. and Technol. A* **35(1)**, 01B101 (2017).
https://doi.org/10.1116/1.4963368

Delivered conference presentations

1 H. Salami[‡], A. Uy, V. Dwivedi, R. A. Adomaitis, Investigation of electrical and optical properties of indium oxide thin-films prepared by atomic layer deposition using trimethylindium and ozone precursors. *AIChE annual meeting*, Pittsburgh (2018).

2 H. Salami[‡], A. Alobaid, R. A. Adomaitis, A Combined graphical / algebraic method for model reduction and analysis of chemical reaction networks: application to atomic layer deposition process. *AIChE annual meeting*, Pittsburgh (2018).

3 V. Dwivedi‡, M. Hasegawa, R. A. Adomaitis, H. Salami, A. Uy, Modification of radiator pigments by atomic layer deposition (ALD). *48th International Conference on Environmental Systems (ICES)*, Albuquerque (2018).

4 H. Salami‡, R. A. Adomaitis, Reaction network structure and flux analysis for thin-film deposition processes. *AIChE annual meeting*, Minneapolis (2017).

5 H. Salami‡, R. A. Adomaitis, Species-reaction graphs for reaction network analysis in thin-film deposition processes. *UMD ResearchFest*, College Park (2017).

6 H. Salami‡, A. Poissant, R. A. Adomaitis, Aluminum oxide thin film growth using atomic layer deposition at precursor underdosed conditions. *UMD ResearchFest*, College Park (2016).

Scheduled conference presentations

1 H. Salami‡, A. Uy, A. Vadapalli, V. Dwivedi, R. A. Adomaitis, Atomic layer deposition of nickel and nickel oxide thin-films for astronomical X-ray optics applications. *AVS 19th International Conference on Atomic Layer Deposition*, Bellevue (July 23, 2019).

2 A. Uy‡, H. Salami, A. Vadapalli, C. Grob, V. Dwivedi, R. A. Adomaitis, Atomic layer deposition of aluminum fluoride for use in optical devices. *AVS 19th International Conference on Atomic Layer Deposition*, Bellevue (July 22, 2019).

3 H. Salami, A. Uy, R. A. Adomaitis, V. Dwivedi‡, M. Hasegawa, Modification of spaceflight radiator coatings by atomic layer deposition for thermal applications. *AVS 19th International Conference on Atomic Layer Deposition*, Bellevue (July 22, 2019).

‡ presenter